



**HAL**  
open science

## Cavitation erosion modelling using SPH

Shrey Joshi

► **To cite this version:**

Shrey Joshi. Cavitation erosion modelling using SPH. Materials Science [cond-mat.mtrl-sci]. Université Grenoble Alpes, 2018. English. NNT : 2018GREAI080 . tel-02014179

**HAL Id: tel-02014179**

**<https://theses.hal.science/tel-02014179>**

Submitted on 11 Feb 2019

**HAL** is a multi-disciplinary open access archive for the deposit and dissemination of scientific research documents, whether they are published or not. The documents may come from teaching and research institutions in France or abroad, or from public or private research centers.

L'archive ouverte pluridisciplinaire **HAL**, est destinée au dépôt et à la diffusion de documents scientifiques de niveau recherche, publiés ou non, émanant des établissements d'enseignement et de recherche français ou étrangers, des laboratoires publics ou privés.

## THÈSE

Pour obtenir le grade de

### **DOCTEUR DE LA COMMUNAUTE UNIVERSITE GRENOBLE ALPES**

Spécialité : **Mécanique des Fluides, Procédés**

Arrêté ministériel : 25 mai 2016

Présentée par

**Shrey JOSHI**

Thèse dirigée par **Marc FIVEL**, Directeur de recherche CNRS,  
et  
codirigée par **Jean-Pierre FRANC**, Directeur de recherche CNRS,  
et par **Giovanni GHIGLIOTTI**, Maître de Conférences UGA.

préparée au sein du **Laboratoire SIMaP**  
dans **l'École Doctorale I-MEP2**

## **Modélisation de l'érosion de cavitation par SPH**

Thèse soutenue publiquement le **9 Novembre 2018**,  
devant le jury composé de :

**Monsieur Arjen ROOS**

Ingénieur de Recherche HDR, Safran Tec, Rapporteur

**Monsieur Stéphane AUBERT**

Professeur des Universités, École Centrale de Lyon, Rapporteur

**Monsieur Rickard BENSOW**

Professeur des Universités, Chalmers University, examinateur

**Madame Magdalena NEUHAUSER**

Ingénieure, Andritz Hydro AG, Examinateur

**Monsieur Marc FIVEL**

Directeur de Recherche CNRS, Directeur de thèse

**Monsieur Jean-Pierre FRANC**

Directeur de Recherche CNRS, Co-directeur de thèse

**Monsieur Giovanni GHIGLIOTTI**

Maître de Conférences, UGA, Co-directeur de thèse





*To Mom, Dad & Anubha*



## Acknowledgement

Firstly, I would like to express my special appreciation and thanks to my supervisors Prof. Marc FIVEL, Prof. Jean-Pierre FRANC and Dr. Giovanni Ghigliotti for their constant support and encouragement throughout the thesis. The innumerable discussions that I have had with Marc during the course of 3 years has helped me more than what I could express in words. The frequent meetings and email exchanges with Jean-Pierre helped me a lot in shaping the thesis in the right direction. The frequent support and encouragement I received from my supervisors has been the core reason I could finish the project in time.

I would also express my gratitude to the CaFE project and the European commission for providing me the opportunity to work in a large project with constant meetings and support from the project members. Special thanks to Prof. Manolis Gavaises (CITY) for his support during the 2 month visit to CITY University London and to Dr. Steffen Schmidt for his support during the 2 months in Technische Universität München. I appreciate the fruitful discussions I had with project members from various Universities and Industries that were a part of the CaFE project and the wonderful times we shared together twice every year.

I express my thanks to Dr Domingo Garcia-Senz from UPC Barcelona for his support in developing the axisymmetric fluid solver used in the thesis, the 1 week visit to his laboratory helped a lot in developing the solver on time. I would also like to thank Dr Anxin Ma from Ruhr-University Bochum for giving his precious time for a week visit to Grenoble and helping me with developing a solid SPH solver. Without any prior knowledge of SPH before the thesis, it couldn't have been possible without their support and the support of various participants I met during SPHERIC conferences who helped me with the mysteries of SPH.

I would like to extend my greatest respect and gratitude to the Jury members for accepting the invitation to be present during the defense and evaluate the work. I am grateful to the referees: Prof. Stéphane Aubert (École Centrale de Lyon) and Dr. Arjen Roos (Safran Tec) for their careful reading, valuable comments and evaluation of the thesis. I have the honor to have Prof. Rickard Bensow (Chalmers University of Technology) and Dr Magdalena Neuhauser (Andritz Hydro AG) as the examiners of the thesis. I also acknowledge the presence of Prof. Marc FIVEL (SIMaP), Prof. Jean-Pierre FRANC (LEGI) and Dr. Giovanni GHIGLIOTTI (LEGI) as a part of the jury members.

I would like to express a special thanks to Mme. Elisabeth LUSSI (SIMaP) for all the administrative support and the times she had to bear with my poor French. I also express my gratitude to Mme. Claire THOMASSON (SIMaP) & Sylvie CHAMPAVIER (SIMaP) for their numerous supports regarding all kinds of administrative works during these years.

But of course life is not all work and moving to a new country is difficult, I would like to thank Mme. Monique FAVREAU-ZUBER and M. Eric ZUBER for their help and support during the initial 9 months of my stay in France. Thanks to all my friends who made my stay in Grenoble memorable, thanks to Prasanta, Richi, Chakri, Kaoutar, Markku, Jenni, Jade, Charlotte & Lucie for the moments we shared together in Grenoble. Last but not the least, I would like to thank my wife Anubha for her constant support and for bearing with me and my parents for their love and support that helped me climb every stepping stone in life.

Shrey Joshi



# CONTENT

<b>1 INTRODUCTION</b>	<b>15</b>
1.1 Motivation	15
1.2 CaFE project	16
1.3 Thesis Objectives	17
1.4 Thesis outline	19
<b>2 INTRODUCTION TO SMOOTHED PARTICLE HYDRODYNAMICS</b>	<b>21</b>
2.1 Introduction	21
2.2 Fundamentals	21
2.3 SPH method	24
2.3.1. Equation of state	25
2.3.2. Momentum equation for fluid	25
2.3.3. Momentum equation for solid	27
2.3.4. Constitutive law for the elasto-visco-plastic solid material	27
2.3.5. Artificial viscosity	28
2.3.6. Time integration	29
2.3.7. Moving the particle	30
2.3.8. Kernel	30
2.3.9. Computational linked list method	30
2.3.10. Boundary condition in SPH	32
2.3.10.1. Dynamic Boundary Conditions	32
2.3.10.2. Repulsive Boundary Conditions	33
<b>3 CAVITATION AND CAVITATION EROSION</b>	<b>35</b>
3.1. Cavitation	35
3.2. Scales of cavitation studies	36
3.3. Rayleigh-Plesset collapse	38
3.4. Cavitation erosion	38

3.5.	Experimental Measurement of Cavitation Erosion	40
3.6.	Empirical models	43
3.7.	Phenomenological models	45
3.8.	Numerical simulations	46
<b>4</b>	<b>CAVITATION EROSION FLUID STRUCTURE INTERACTION SOLVER IN 2D</b>	<b>51</b>
4.1	Introduction	51
4.2	2D solver development	51
4.2.1.	Fluid Solver	51
4.2.2.	Solid Solver	52
4.2.3.	Fluid structure interaction	53
4.3	Results and validation	55
4.3.1.	Bubble collapse	55
4.3.2.	Solid solver	58
<b>5</b>	<b>CAVITATION SOLID SOLVER IN 2D AXISYMMETRIC</b>	<b>63</b>
5.1	Introduction	64
5.2	SPH method	67
5.2.1.	SPH fundamentals	67
5.2.2.	2D SPH formulation for Solid mechanics	68
5.2.3.	Moving the particles	69
5.2.4.	Time integration	70
5.2.5.	Artificial viscosity	71
5.3	Axisymmetric SPH for Solid Mechanics	71
5.3.1.	Methodology	71
5.3.2.	Correction close to symmetry axis	73
5.3.3.	Validation test case for the axisymmetric SPH solid solver	77
5.4	SPH simulations for solid response	81
5.4.1.	Mass loss simulation	81

5.4.2.	Parametric study for different extend of indent profile	82
5.4.3.	Strain rate effects	85
5.5	Conclusion and future work	86
<b>6</b>	<b>FLUID STRUCTURE INTERACTION SOLVER</b>	<b>89</b>
6.1.	Introduction	90
6.2.	Methodology	93
6.2.1.	Fluid solver	93
6.2.2.	Solid solver	95
6.2.3.	Fluid structure interaction in SPH	96
6.3.	Validations	97
6.3.1.	Fluid solver validation	97
6.3.2.	Solid solver validation	98
6.4.	Results and discussion	100
6.4.1.	Single bubble collapse: Detached cavity vs Attached cavity	101
6.4.2.	Detached cavity material response	103
6.4.3.	Detached cavity: Strain rate effect	104
6.4.4.	Dynamic loading in cavitation	105
6.4.4.1.	Static vs dynamic loading in cavitation	105
6.4.4.2.	Inertial effects on material response	106
6.4.5.	Effective Pressure	110
6.4.6.	Characteristic response time	112
6.5.	Conclusions and future work	115
<b>7</b>	<b>FLUID STRUCTURE INTERACTION PARAMETRIC STUDY</b>	<b>119</b>
7.1.	Introduction	120
7.2.	Simulation cases and description	121
7.2.1.	Simulation domain and cases	121
7.2.2.	Fluid and material parameters	123

7.3. Results and discussion	123
7.3.1. Effect of stand-off ratio	125
7.3.2. Effect of driving pressure	128
7.3.3. Effect of bubble size	130
7.3.4. Effect of strain rate	132
7.3.5. Plastic deformation potential	133
7.4. Conclusions and future work	135
<b>8 CONCLUSIONS AND PERSPECTIVES</b>	<b>137</b>
8.1 Conclusions	137
8.2 Perspectives	140
<b>Nomenclature</b>	<b>149</b>

## Abstract

The thesis is focused on development of a Smoothed Particle Hydrodynamics (SPH) Fluid-Structure Interaction (FSI) cavitation solver to investigate the phenomenon of material deformation under cavitation load. The fluid solver and the solid solver are validated against Rayleigh-Plesset spherical bubble collapse case and FEM solver respectively. The fluid solver is developed using an open source SPH code SPHYSICS\_2D and the code is changed from 2D to 2D axisymmetric. The solid SPH solver is developed in-house in 2D axisymmetric with a novel scheme to solve typical issues near symmetry axis. The solid solver has the capability to solve for non-linear isotropic hardening with strain rate effects (commonly known as Johnson-Cook plasticity model).

Various cases for detached and attached cavities are simulated using the FSI solver. The results show that, for the same magnitude of pressure wave initiating the collapse and the same size of the bubble, the micro jet can produce twice the maximum plastic deformation compared to the shock wave. Hence a micro jet dominated impact would exhibit a smaller incubation time compared to the detached cavity in the case of repeated cavitation impacts. It is also observed that the volume of material that is plastically deformed in case of a micro jet is miniscule compared to a shock wave impact (almost 800 times smaller). This would imply that even though the incubation time for material erosion might be lower for a micro jet collapse, the shock wave can plastify a much larger volume of material and so the erosion rate should be higher for a shock wave impact. Hence it could be inferred that the material erosion ability of a shock wave is much higher than that of a micro jet.

An important and novel finding in the present study is the response of the material for a detached cavity where plastic deformation does not occur at the center of collapse but at an offset from the center. The results show that even though the pressure experienced by the material is the highest at the center, it does not produce the maximum plastic deformation. This is for the first time that such a phenomenon is reported in cavitation studies. We find that the phenomenon is linked to inertial effects where the material does not respond to the load as the rate of loading and unloading is extremely high. The effect is linked to the high loading and unloading rate near the center of the collapse due to the flat geometry of the solid medium. The study clearly demonstrates that maximum pressure does not always correspond to the location of maximum plastic deformation or material erosion.

Fluid structure interaction simulations for different stand-off ratios, driving pressure and bubble radius have been computed. Results show that for varying stand-off ratio while keeping the bubble radius and driving pressure constant, the attached cavities ( $SR \leq 1$ ) show a higher plastic strain magnitude and a higher absorbed energy density which would suggest a quicker incubation time. However, the volume of plastic deformation zone is much lower in attached cavities thus the total absorbed energy and the erosion rate would be higher for a detached cavity compared to an attached one.

The change in driving pressure shows, as expected, that both the absorbed energy density (hence incubation time) and the total absorbed energy (hence erosion rate) increase with increasing driving pressure. The change in bubble radius while keeping other parameters constant do not affect the magnitude of plastic strain and absorbed energy density much, which would suggest that irrespective of the size of the cavitation bubble, the incubation time should remain similar. However, since the volume of plastically deformed zone goes almost linearly with the bubble size, the total absorbed energy or the erosion rate increases significantly with increasing bubble size.

Fluid structure interaction studies in the past have not considered strain rate sensitivity while defining the plasticity model. The strain rate effects suggest that the magnitude of plastic strain is over predicted while using plasticity models that do not use strain rate sensitivity. The over prediction of the magnitude of plastic strain of around 60% for detached cavities presented in the paper and around 200% for attached cavities presented in the paper is observed. This would lead to an under prediction of incubation time and over prediction of erosion rate while using strain rate insensitive plasticity models.



## Résumé

La thèse est organisée autour du développement d'un modèle d'interaction fluide - structure (FSI) simulant le phénomène de cavitation pour étudier la déformation induite dans le matériau solide. Le solveur fluide est validé par comparaison avec le calcul analytique d'effondrement de bulles sphériques de Rayleigh-Plesset. Le solveur solide est comparé à des calculs menés par la méthode des éléments finis. Le solveur fluide est développé à partir du code open source SPHYSICS\_2D utilisant la méthode des Smoothed Particles Hydrodynamics (SPH). Dans cette thèse, le code 2D a été modifié pour traiter le cas axisymétrique. Le solveur solide SPH a été complètement développé en interne en 2D axisymétrique avec un nouveau schéma pour résoudre les problèmes apparaissant à proximité de l'axe de symétrie. Une loi de comportement élasto-visco-plastique de type Johnson Cook est implémentée dans le solveur solide, ce qui permet de prendre en compte l'effet de la vitesse de déformation sur l'écroutissage du matériau.

Les applications du solveur FSI traitent le cas d'une bulle unique implosant au voisinage d'une surface solide. Deux cas sont envisagés : celui d'une bulle détachée de la surface solide pour laquelle l'effondrement induit une onde de choc dans le liquide ; et celui d'une bulle au contact de la surface pour lequel un micro-jet de liquide vient impacter la surface solide. Pour une taille de bulle donnée, les résultats montrent que, pour une même amplitude de l'onde de pression déclenchant l'effondrement de la bulle, le micro-jet peut produire deux fois plus de déformation plastique que l'onde de choc. Par conséquent, un impact dominé par un micro-jet (cavité attachée) présenterait un temps d'incubation plus court que la cavité détachée dans le cas d'impacts répétés par cavitation. On observe également que le volume de matière déformée plastiquement dans le cas du micro-jet (cavité attachée) est 800 fois plus petit que celui déformé par l'impact d'une onde de choc (cavité détachée). Nous en déduisons que si le temps d'incubation pour l'érosion du matériau peut être plus court dans le cas d'un effondrement par micro-jets, l'onde de choc peut plastifier un volume beaucoup plus important de matériau et donc le taux d'érosion devrait être plus élevé dans le cas d'un impact par onde de choc. Par conséquent, la capacité d'érosion d'une cavité détachée est beaucoup plus élevée que celle d'un micro-jet.

Un important résultat de cette étude concerne les cavités détachées où il est montré que la déformation plastique ne se produit pas au centre de l'effondrement mais à un décalage par rapport à l'axe de symétrie. Les résultats montrent également que même si la pression subie par le matériau est la plus élevée au niveau de l'axe de symétrie, la déformation plastique ne sera pas maximale à cet endroit mais dans une zone éloignée du centre. C'est la première fois qu'un tel phénomène est reporté dans les études menées sur la cavitation. Nous montrons que ce phénomène est lié à des effets inertiels qui empêchent la déformation du matériau lorsque la vitesse du chargement est extrêmement élevée, ce qui est le cas au centre de l'impact en raison de la géométrie d'interaction entre l'onde de choc sphérique et la surface plane du solide. L'étude démontre ainsi clairement que le lieu de pression maximale en paroi ne coïncide pas toujours avec l'emplacement de la déformation plastique maximale.

Une étude paramétrique est menée pour quantifier les effets de la distance bulle/paroi, de la pression d'effondrement et du rayon de la bulle. Les résultats montrent que les cavités attachées engendrent une plus grande amplitude de déformation plastique cumulée et une densité d'énergie absorbée plus élevée, ce qui suggère un temps d'incubation plus rapide. Cependant, le volume de la zone de déformation plastique est beaucoup plus faible pour les cavités attachées si bien que l'énergie totale absorbée et le taux d'érosion devraient être plus élevés pour une cavité détachée que pour une cavité attachée.

La variation de la pression d'effondrement montre, comme prévu, que la densité d'énergie absorbée (d'où le temps d'incubation) et l'énergie totale absorbée (d'où le taux d'érosion) augmentent avec une pression croissante. Le changement du rayon de la bulle tout en gardant les autres paramètres constants n'affecte pas beaucoup l'amplitude de la déformation plastique ni la densité d'énergie absorbée, ce qui suggère que quelle que soit la taille de la bulle de cavitation, le temps d'incubation devrait rester similaire. Cependant, comme le volume de la zone déformée plastiquement varie presque linéairement avec la taille de la bulle, l'énergie totale absorbée ou le taux d'érosion augmente significativement avec la taille de la bulle.

Dans le passé, les études sur l'interaction des structures fluides n'ont jamais pris en compte la sensibilité à la vitesse de déformation dans le modèle de plasticité. Nos simulations montrent que l'ampleur de la déformation plastique est surestimée en utilisant des modèles de plasticité qui ne considèrent pas la sensibilité à la vitesse de déformation. Cette surestimation de l'ampleur de la déformation plastique est

d'environ 60 % pour les cavités détachées présentées dans le document et d'environ 200 % pour les cavités attachées. Nous montrons ainsi que de telles études réductrices fondées sur des modèles de plasticité insensibles à la vitesse de déformation conduisent à une sous-estimation du temps d'incubation et à une surestimation du taux d'érosion.

# 1 INTRODUCTION

## 1.1 Motivation

This thesis is focussed on the fundamental aspect of cavitation erosion and the underlying phenomenon. Specifically, it focusses on studying cavitation erosion at a micro scale to see how bubble collapses lead to material damage using numerical methods.

Cavitation erosion is a major issue amongst a wide range of equipment such as hydraulic devices, diesel injectors, artificial heart valves etc. Cavitation is defined as the appearance of vapour cavities inside a continuous and homogeneous liquid medium. The generation of vapour cavities could happen due to various reasons, but the cause is mostly associated to the drop of local pressure below the vapour pressure. A drop of pressure below the vapour pressure leads to vaporization of liquid commonly known as cavitation. During cavitation the continuum liquid medium breaks down to form vapour cavities. These vapour bubbles can collapse when the ambient pressure increases above the vapour pressure. The collapse of these bubbles can be very different depending on the position of the bubbles with respect to a solid surface. A collapse of a bubble near a solid surface can lead to the formation of a high velocity micro jet and subsequent shock waves. The asymmetric collapse in presence of the wall near the bubble is due to the lack of fluid flow from the side of the wall. The solid surface experiences a high pressure due to the shock wave that is produced due to the micro jet hitting the bubble surface and the high velocity micro jet hitting the surface. The magnitude of the pressure acting on the surface could be high enough to cause plasticity and eventually damage in the material. Although the experimental measurement of these pressures acting on the surface still remains a challenge, various studies have estimated it to be around a few GPa [1-5]. Moreover, experimental investigation offers only limited information about bubble collapse and the subsequent formation of micro jet and pressure wave since any intrusive measurement can cause deviations. Such difficulties in experimental investigation has led to the use of numerical studies to understand and analyse cavitation.

However, most studies in the past have focused on understanding the fluid aspect of cavitation in detail, a thorough study that can lead to better understanding would include material damage along with the bubble dynamics which would in a numerical study mean use of a fluid structure interaction cavitation solver. This could potentially lead to better understanding of material damage due to cavitation, leading to better design and effective protection of the material

surface under cavitation loads. This serves as the motivation for this thesis, to develop a Fluid structure interaction solver for cavitation erosion.

## **1.2 CaFE project**

This thesis is a part of the European Project CaFE “Development and experimental validation of computational models for cavitating flows, surface erosion damage and material loss” [6] funded within the Horizon 2020 program [7]. This Marie Skłodowska-Curie International Training Network project focusses on various aspects of cavitation from both numerical and experimental point of view.

The project is segmented into three basic packages, the first focuses on the fundamental aspect of cavitation such as, developing interface tracking model suitable for direct numerical simulations of bubble cluster dynamics near wall surfaces, simulating single bubble collapse and bubble cloud collapse, developing coupled fluid structure interaction solvers. The above stated techniques are then used to simulate material loss as function of time for different materials and different stages including the incubation period, the acceleration period and the quasi-steady state period

The second package of the project focusses on experimental techniques for quantitative measurement in cavitating flows. Some key experimental development includes, flow measurements using SPIV (Stereo Particle Image Velocimetry), high speed imaging for cavitating vortex in existing test rig configuration, manufacturing of portable refractive index matching rig for pulsatile flow resembling the cardiac pulse and able to accommodate mechanical heart valve measurements of wall pressure and material loss for different fluids and target materials.

Finally, the third part of the project focusses on macro simulation of cavitation with industrial applications. It includes development of numerical models using LES and RANS techniques to simulate cavitation in applications like fuel injectors, marine propellers, gear pumps and heart valves.

Within the CaFE program, 15 Ph.D. students were hired in 8 organizations spread over UK, Sweden, Netherlands, Germany, Austria, and France. The work was conducted in a collective manner based on frequent review meetings, series of seminars and two commitments of two months spent in partners’ place. As far as I was concerned, I spent two months in City, London

in the group of Prof. Manolis Gavaises and two months in Technische Universität Munich working with Dr. Steffen Schmidt.

### **1.3 Thesis Objectives**

Most numerical studies presented in the past decades have focused on solving cavitation bubble collapse dynamics which has led to significant understandings from the fluid aspect of cavitation. However, a thorough understanding of material damage induced by collapsing bubbles still needs some work. For instance, most numerical CFD studies estimate cavitation erosion prone areas using either peak pressures or Cavitation Aggressiveness Index (CAI) [8-10]. However, it is still debatable as to whether peak pressure or CAI can accurately identify the cavitation erosion prone areas. Moreover, these methods can only try to predict cavitation prone areas and cannot predict the pit sizes and the magnitude of material erosion accurately enough. Change in material topology due to cavitation can change the way cavitation loads act on the deformed surface. Hence to address the above issues better, recently there has been a thrust towards modelling cavitation erosion using Fluid structure interaction solvers to understand the phenomenon of cavitation erosion in entirety [11-13]. A thorough numerical study of cavitation that can provide a holistic understanding ideally requires a two-way fluid structure interaction coupling to get realistic results for cavitation erosion. A comprehensive cavitation numerical model should ideally include the following elements in the solver:

- A fluid model capable of capturing the dynamics of a collapsing bubble including the details about the micro jet and the shock waves.
- A solid solver model to solve for the material response due to the pressure acting on the material surface as a result of the micro jet and the shock waves. The solver must be capable of solving an elasto-visco plastic behaviour of the material as well as the development of damage in the material. Since cavitation is a relatively fast process, strain rate dependent behaviour must also be included in the model.
- A fluid structure interaction scheme: During a cavitation bubble collapse, high intensity shock waves are produced along with micro jet. As a shock wave travels through the fluid to the solid, a part of the wave is reflected back into the liquid and the rest gets transmitted to the solid [14]. In the case of two elastic media, transfer of the energy and the solid-liquid interface velocity depend on the ratio of acoustic impedances of the liquid and solid. A two-way coupling is required to model this behaviour properly.

Conventionally, ALE (Arbitrary Lagrangian Eulerian) methods have been used so far to simulate such a problem [15]. The problem is quite complex since the fluid solver (generally a Finite Volume Method (FVM) code) and the solid solver (generally a Finite Element Method (FEM) code) are two different codes which then need to be coupled in order to communicate data across the two solvers. Moreover, the elasto-plastic deformation of the solid mesh medium due to cavitation loads implies the fluid mesh has to be re-constructed to match the solid mesh and maintain the continuity at the interface. To overcome the above complexity, in the present study a first attempt has been made to solve cavitation erosion using a meshless particle method, namely the Smoothed Particle Hydrodynamics (SPH), to model both the fluid and the solid behaviour in a unique Lagrangian framework. The method offers the following advantages:

- Both fluid and solid response can be captured using the same solver and the same numerical method i.e. SPH, hence eliminates the use of two different solvers while numerically solving for cavitation. Both the solid and the fluid can be coded and solved within a single code making it much easier from the development perspective.
- Coupling an FVM solver to an FEM solver can be quite complicated and requires a dedicated procedure for data transfer across the two codes. The problem is eliminated here since the solver uses SPH for both solid and fluid in a common code. No such coupling is required; the data being easily exchanged within the shared RAM memory. For each particle, one only needs to specify if it is a fluid or a solid particle.
- The material will exhibit deformation during cavitation loading, while using mesh methods would require a mesh re-construction algorithm or a moving mesh to account for the deformed material. The reconstruction of mesh for fluid is required which is complex and can slow the code significantly. The tricky mesh reconstruction for the fluid domain is eliminated when using meshless methods like SPH where both the fluid and the solid are solved using a Lagrangian formulation and hence such deformations are already taken care via particle movement.

The objective of the thesis is to develop the Smoothed Particle Hydrodynamics (SPH) fluid structure interaction cavitation solver. To start, an existing 2D open source fluid SPH code SPHYSICS is used as a basis to develop the solver further [16]. The aim is to modify the fluid code to solve for bubble collapse and to develop a solid solver with an aim to be coupled to the fluid solver for simulating a collapsing bubble over a solid medium in 2D. The same solver is then extended to 2D axisymmetric to obtain realistic results of material damage due to a

collapsing spherical bubble. Finally, the solver will be used to simulate FSI cavitation bubble collapse which potentially could lead to better understanding of the cavitation erosion phenomenon.

#### **1.4 Thesis outline**

The thesis has been divided into the following chapters:

**Chapter 2:** Introduces the reader to the numerical method Smoothed Particles Hydrodynamics (SPH), it gives an overview of the basics of the method and how a fluid or a solid system is solved using SPH.

**Chapter 3:** Introduces the reader to the phenomenon of cavitation erosion and the underlying physics. Also provides an overview of the state of the art in the area of cavitation erosion studies with a focus on numerical methods used to study cavitation.

**Chapter 4:** This chapter provides details on the development of a SPH 2D fluid structure interaction solver and validations. The fluid solver is validated against Rayleigh-Plesset solution of a collapsing spherical cavity, whereas the solid solver is validated against FEM results.

**Chapter 5:** New developments are presented in this chapter with regards to development of a solid solver capable of solving elastic-plastic response and damage in 2D axisymmetric, which better represents the actual phenomenon of cavitation. New equations are derived for SPH solid in 2D axisymmetric which can treat particles close to the symmetry axis in a mathematically consistent way. The solver is validated against FEM results. Moreover, strain rate hardening effects are also taken into account in the solver. A simple case of Gaussian displacement is carried out using the solver to demonstrate the importance of strain rate sensitivity.

**Chapter 6:** The fluid structure interaction solver and validation in 2D axisymmetric is provided in this chapter. Interesting observations are made for a detached cavity collapse where plastic strain in the material shows a counter-intuitive behaviour. The behaviour is dealt with in details to understand the plastic strain accumulation in the material due to a cavity collapse.

**Chapter 7:** A parametric analysis of single bubble collapse simulation is carried out. Pressure, bubble radius and stand-off parameter are varied to study the effect of each of these parameters on the material response. Focus on plastic strain energy absorbed by the material.

**Chapter 8:** This chapter provides conclusions to the thesis and the possible future perspectives.

**Nomenclature:** A nomenclature list has been provided at the end of the thesis.

# 2 INTRODUCTION TO SMOOTHED PARTICLE HYDRODYNAMICS

This chapter introduces the reader to the SPH method, since a large number of equations and variables are introduced in this chapter, a nomenclature (pg. 149) can be found at the end of the manuscript. Also a standard notation has been used throughout the thesis to denote vectors (an arrow on top) and tensors (bold letters).

## 2.1 Introduction

Smoothed Particle Hydrodynamics (SPH) is a numerical method to solve partial differential equations by discretizing the computational domain using set of particles. It was first introduced by Lucy [17] in 1977 for astrophysics calculations and later by Monaghan [18] for fluid flows. The method is based around interpolation to express a function at any point in space using its values at a set of disordered neighbouring points called the particles by using a kernel function. The advantage is that the method does not require any grid or mesh as the material is represented by particles and the derivatives are calculated based on derivatives of the interpolation function called the kernel function. Moreover, the method being Lagrangian in nature offers certain advantages over the Eulerian method like FVM in certain cases.

## 2.2 Fundamentals

The following identity is the starting point of the fundamentals which SPH is based on integral interpolant,

$$A(\vec{r}) = \int A(\vec{r}') \delta(\vec{r} - \vec{r}') d\vec{r}' \quad (2.1)$$

Where  $\delta(\vec{r})$  is the Dirac delta function and  $d\vec{r}'$  is an infinitesimal volume element in the integration space. The integration of the Dirac delta function wrt  $d\vec{r}'$  is unity. We can replace the Dirac delta function in equation 2.1 by a kernel function. The kernel function ( $W$ ) is used for interpolation and must satisfy the following properties: firstly, the integration of the kernel function over the whole domain should lead to unity as given by equation 2.2 and secondly, as the limit of  $h$  (commonly known as smoothing length) tends to zero the kernel function becomes a Dirac-Delta function as given by equation 2.3.

$$\int W(\vec{r} - \vec{r}', h) d\vec{r}' = 1 \quad (2.2)$$

and

$$\lim_{h \rightarrow 0} W(\vec{r} - \vec{r}', h) = \delta(\vec{r} - \vec{r}') \quad (2.3)$$

where  $W$  is the kernel function and  $h$  is the smoothing length of the kernel function. The above equation simply means that the value of function  $A$  at point  $\vec{r}$  can be calculated by using an interpolation function ( $W$ ) over the neighbouring points ( $\vec{r}'$ ).

As mentioned earlier the basis of SPH is an interpolation method that allows any function/quantity to be expressed in terms of the neighbouring points. The integral interpolant of any function  $A$  at a position  $\vec{r}$  is defined by the integration over the entire domain ( $\Omega$ ):

$$A(\vec{r}) = \int_{\Omega} A(\vec{r}') W(\vec{r} - \vec{r}', h) d\vec{r}' \quad (2.4)$$

In order to use equation 2.4 for numerical purpose, the equation is transformed into a discretized form where it takes a form of a summation interpolant given by

$$A(\vec{r}) \approx \sum_{j=1}^N A(\vec{r}_j) W(\vec{r} - \vec{r}_j, h) \frac{m_j}{\rho_j} \quad (2.5)$$

where the summation index  $j$  denotes a particle label, and the summation is over all the particles. Particle  $j$  has mass  $m_j$ , position  $\vec{r}_j$  and density  $\rho_j$ . The value of any quantity  $A$  at  $\vec{r}_j$  is denoted by  $A(\vec{r}_j)$ .

The summation is over all the particles in the domain but in practice that would increase computational cost considerably and hence the summation must be only over near neighbors as the kernel function decreases rapidly with distance. Typically,  $h$  is close to the particle spacing, and the kernel  $W$  is effectively zero beyond a distance  $2h$ . In practice kernels which have compact support i.e. they tend to zero at a finite distance close to the particle spacing are a perfect fit for such calculations. As an example of the use of kernel estimation, suppose function  $A$  in equation 2.4 is the density  $\rho$ . The interpolation formula then gives the following estimate for the density at a point  $\vec{r}$

$$\rho(\vec{r}) = \sum_{j=1}^N m_j W(\vec{r} - \vec{r}_j, h) \quad (2.6)$$

This demonstrates how the mass of particle around point  $\vec{r}$  is smoothed to give an estimate of the density. Considering that  $h$  is a constant value, the equation 2.6 could be integrated wrt  $d\vec{r}$  to give,

$$\int \rho(\vec{r}) d\vec{r} = \sum_j m_j \int \nabla W(\vec{r} - \vec{r}_j, h) d\vec{r} = \sum_j m_j = M \quad (2.7)$$

where  $\nabla W$  is the gradient of the kernel function.

Which demonstrates that the mass is conserved exactly unless  $h$  is a variable. In the latter case, the integral can no longer be  $M$  but the errors are small as the mass of each particle itself is always conserved.

The key element is that we can write a differentiable interpolant of a function from its values at the particles by using a kernel which is differentiable. Derivatives of this kernel can be obtained by ordinary differentiation; there is no need to use finite differences or any another numerical method. For instance, if we want  $\nabla A$ , we can use,

$$\nabla A(\vec{r}) \approx \sum_{j=1}^N A(\vec{r}_j) \nabla W(\vec{r} - \vec{r}_j, h) \frac{m_j}{\rho_j} \quad (2.8)$$

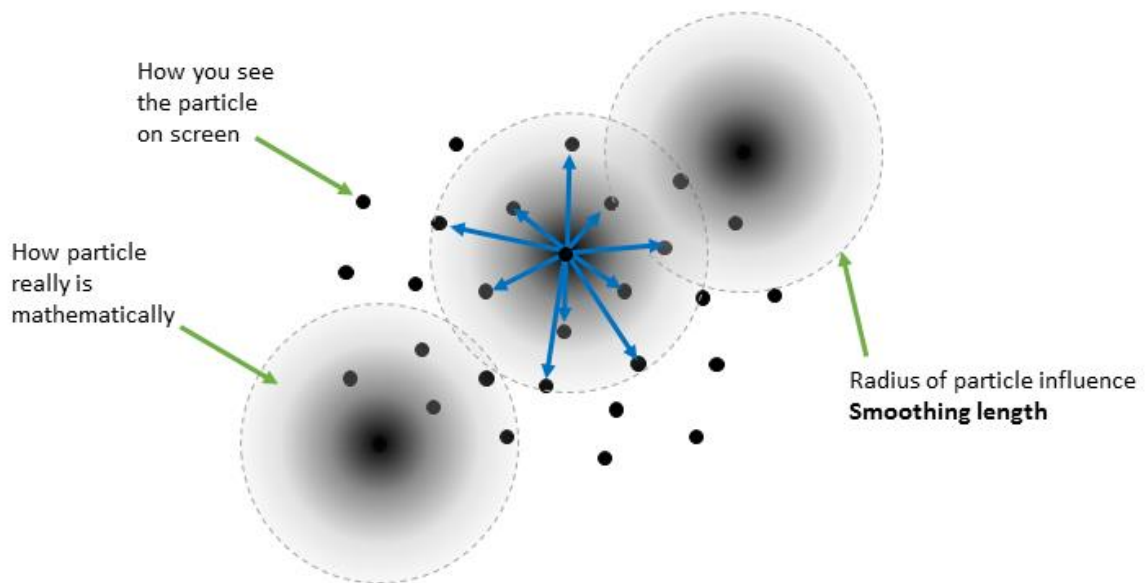


Figure 2.1. Schematic showing how SPH particles interact with neighbours.

Figure 2.1 is a representation of how SPH particles interact with each other. Particles on a computer screen might look like a set of points, however, mathematically every particle has an influence sphere around it defined by the kernel function and the particles interact if the neighboring particle lies within the influence sphere. Figure 2.2 shows the kernel function of the particle in red, the particles inside the radius  $h$  contribute to the interpolation of any function from the neighbouring points to the point under consideration (in red).

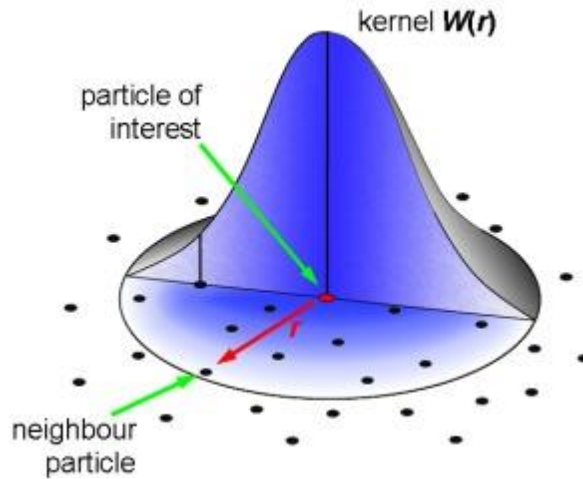


Figure 2.2. A typical SPH kernel in 2D.

### 2.3 SPH method

SPH was first introduced for fluid flows by Monaghan [18]. We hereby present the standard SPH method for fluid simulation. Any SPH simulation starts with estimating density as the first step of the simulation, it could be an interpolation given by,

$$\rho_a = \sum_b m_b W_{ab} \quad (2.9)$$

or

$$\frac{d\rho_a}{dt} = \sum_b m_b \vec{v}_{ab} \cdot \nabla_a W_{ab} \quad (2.10)$$

where  $\vec{v}_{ab} = \vec{v}_a - \vec{v}_b$  is the relative velocity of particle a with respect to particle b. Most SPH calculations use equation 2.9 as this conserves mass exactly. However, equation 2.10 has its own advantages. Consider a fluid domain at its edge, the particles on the edge would see lesser number of particles inside its kernel compared to a particle far from the edge in the interior. Hence equation 2.9 would lead to a lower density estimation near the edges which would lead

to pressure deviations. However, with equation 2.10 the density even at the edge would only change from the initial density if the particle starts to have relative velocities. There is also a computational advantage that while using equation 2.10 all the derivatives can be processed in just one subroutine or one pass.

### 2.3.1. Equation of state

Once the densities are estimated, the next step is to solve for pressure. There are various equations in the literature that can relate pressure to density, however it depends on the physics of the problem. For an incompressible solver, generally the Poisson equation is solved which is given by the following in 2D,

$$\nabla^2 P = 2\rho \left[ \left( \frac{\partial u}{\partial x} \cdot \frac{dv}{dy} \right) - \left( \frac{\partial u}{\partial y} \cdot \frac{\partial v}{\partial x} \right) \right] \quad (2.11)$$

where  $u$  and  $v$  are the velocity components in  $x$  and  $y$  directions. However, solving the above equation could be time-consuming and hence equation such as ideal gas equation is preferred. There are a variety of equations that can overcome the problem of high compressibility but the one widely used in fluid simulations for water is the Tait equation of state as it enforces low density variations and is cost effective to compute. The Tait equation of state gives relative pressure where the background pressure can simply be added as a constant value to the outcome of the equation below,

$$P = B_1 \left( \left( \frac{\rho}{\rho_0} \right)^\gamma - 1 \right) \quad (2.12)$$

where  $\gamma = 7$ ,  $B_1 = c_0^2 \rho_0 / \gamma$ ,  $\rho_0 = 1000 \text{ kg m}^{-3}$  is the reference density and  $c_0$  is the sound speed at the reference density.

### 2.3.2. Momentum equation for fluid

The acceleration equation for an ideal fluid (viscous effects are neglected in the present work since phenomenon like bubble collapse are dominated by inertial effects) neglecting body forces can be written as the following,

$$\frac{d\vec{v}_a}{dt} = -\frac{1}{\rho} \vec{\nabla} P \quad (2.15)$$

where  $P$  is pressure in the fluid. According to equation 2.8 any derivative can be written in the following discrete SPH form,

$$(\vec{\nabla}P)_a = \sum m_b \frac{P_b}{\rho_b} \vec{\nabla}_a W_{ab} \quad (2.16)$$

The approximation for acceleration would then be,

$$\frac{d\vec{v}_a}{dt} = -\frac{1}{\rho_a} \sum m_b \frac{P_b}{\rho_b} \vec{\nabla}_a W_{ab} \quad (2.17)$$

However, this equation does not conserve linear or angular momentum as the force on particle  $a$  due to  $b$  is not equal and opposite to the force on  $b$  due to  $a$ . Consider just two particles in a system  $a$  and  $b$ . The force of  $a$  due to  $b$  is given on the left hand side and force on  $b$  due to  $a$  is given on the right in the following equation (note that the value of kernel derivative remains the same and hence is not included in the equation for simplicity)

$$\frac{m_a m_b P_b}{\rho_a \rho_b} \neq \frac{m_a m_b P_a}{\rho_a \rho_b} \quad (2.18)$$

To ensure linear and angular momentum conservation we re-write the gradient of pressure as the following,

$$\frac{\vec{\nabla}P}{\rho} = \vec{\nabla}\left(\frac{P}{\rho}\right) + \frac{P}{\rho^2} \vec{\nabla}\rho \quad (2.19)$$

Using SPH interpolations we can write the first term on the right hand side as,

$$\vec{\nabla}\left(\frac{P}{\rho}\right)_a = \sum_b \frac{P_b}{\rho_b^2} \vec{\nabla}_a W_{ab} \quad (2.20)$$

and the second term as

$$\frac{P_a}{\rho_a^2} (\vec{\nabla}\rho)_a = \frac{P_a}{\rho_a^2} \sum_b m_b \vec{\nabla}_a W_{ab} \quad (2.21)$$

Hence the acceleration equation becomes

$$\frac{d\vec{v}_a}{dt} = -\sum m_b \left(\frac{P_b}{\rho_b} + \frac{P_a}{\rho_a}\right) \vec{\nabla}_a W_{ab} \quad (2.22)$$

The above equation conserves linear and angular momentum and is widely used in SPH schemes.

### 2.3.3. Momentum equation for solid

The calculation for a solid scheme starts the same way as a fluid scheme by calculating the density using either of the equation 2.9 or 2.10. However, in a fluid scheme we use an equation of state to obtain the pressure, for a solid we use the following equations to obtain the stress tensor which would be used to calculate the acceleration equation for a solid. The following equation gives a relationship between strain rate and velocity of the particles,

$$\rho_a \dot{\varepsilon}_a^{ij} = \frac{1}{2} \sum_{b=1}^n m_b \left[ (v_b^i - v_a^i) \frac{\partial W_{ab}}{\partial x_a^j} + (v_b^j - v_a^j) \frac{\partial W_{ab}}{\partial x_a^i} \right] \quad (2.23)$$

The velocities obtained during the previous time step are used in equation 2.23 to calculate strain rates. The strain rates are then integrated wrt to time to obtain the strain tensor.

### 2.3.4. Constitutive law for the elasto-visco-plastic solid material

The constitutive law is then used to obtain the stress tensor using the following equation for an elastic deformation,

$$\sigma_{ij} = 2\mu \varepsilon^{ij} + \lambda \delta_{ij} \varepsilon^{kk} \quad (2.24)$$

where  $\mu$  and  $\lambda$  are Lamé parameters.

For decomposing the elastic and plastic deformations, we use the Johnson Cook model given by equation 2.27. Details on plastic strain increment calculation are given in Appendix B. Once the stress tensor is obtained by returning to the yield curve, the following acceleration equation is used to obtain velocity derivatives wrt time,

$$\frac{dv_a^i}{dt} = \sum_b m_b \left( \frac{\sigma_a^{ij}}{\rho_a^2} + \frac{\sigma_b^{ij}}{\rho_b^2} - \Pi_{ab} \right) \frac{dW_{ab}}{dx_a^j} \quad (2.25)$$

where  $\Pi$  is the artificial viscosity term and will be explained in section 5.2.5.

For modelling plasticity and strain-rate dependent plasticity, we use the phenomenological Johnson-Cook model [19] relating the yield stress ( $\sigma_y$ ) to the equivalent cumulated plastic deformation ( $\varepsilon_p$ ) and the associated plastic strain rate ( $\dot{\varepsilon}_p$ ):

$$\sigma_y(\varepsilon_p, \dot{\varepsilon}_p, T) = [A_0 + B_0(\varepsilon_p)^n][1 + C_0 \ln(\dot{\varepsilon}_p^*)][1 - (T^*)^m] \quad (2.26)$$

where  $T^* = \frac{(T - T_0)}{(T_m - T_0)}$  is the non-dimensional temperature and  $\dot{\varepsilon}_p^* = \frac{\dot{\varepsilon}_p}{\dot{\varepsilon}_{p0}}$  the non-dimensional plastic strain rate.

In this work the temperature effects are neglected and equation 2.26 reduces to

$$\sigma_y(\varepsilon_p, \dot{\varepsilon}_p, T) = [A_0 + B_0(\varepsilon_p)^n][1 + C_0 \ln(\dot{\varepsilon}_p^*)] \quad (2.27)$$

In the Johnson-Cook model,  $A_0$ ,  $B_0$ ,  $C_0$ ,  $n$  and  $m$  are material constants. Also  $\dot{\varepsilon}_{p0}$  is the effective plastic strain-rate of the quasi static test used to determine the yield and hardening  $A_0$ ,  $B_0$  and  $n$ .  $T_0$  is a reference temperature and  $T_m$  is the reference melting temperature. For conditions where  $T^* < 0$ , we assume that  $m = 1$ .

### 2.3.5. Artificial viscosity

The momentum equations provided in the above section refers to an artificial viscosity term. A momentum conservation equation in a continuum field is given by,

$$\frac{d\vec{v}}{dt} = -\frac{1}{\rho} \vec{\nabla} P + \vec{b} + \vec{\Pi} \quad (2.28)$$

Where  $\vec{b}$  is the body force term and  $\vec{\Pi}$  is the diffusion term. Different approaches, based on various existing formulations of the diffusive terms, can be considered in the SPH method to describe the momentum equation. Three different options for diffusion can be used: (i) artificial viscosity, (ii) laminar viscosity and (iii) full viscosity (laminar viscosity+ Sub-Particle Scale (SPS) Turbulence). These options are available in the present solver and the details can be found in the solver guide [16]. This work uses the artificial viscosity method proposed by Monaghan [20], which is used widely due to its simplicity and is explained in section 5.2.5.

### 2.3.6. Time integration

Consider the momentum equation (equation 2.22) and position equation in the following form

$$\frac{d\vec{v}_a}{dt} = \vec{F}_a \quad (2.29)$$

$$\frac{d\vec{r}_a}{dt} = \vec{V}_a \quad (2.30)$$

where  $\vec{F}_a$  represents force and  $\vec{V}_a$  represents the velocity contribution from particle  $a$  and from neighboring particles (XSPH correction [21]). The XSPH correction avoids penetration of particles as it averages the velocity of the particle according to the flow velocity in the nearby region, thus avoiding sharp gradients of velocity in the flow, more details can be found in section 2.3.7 regarding XSPH.

The predictor step uses the time derivatives from the previous time step to predict velocities and position at half-time step

$$\vec{v}_a^{n+1/2} = \vec{v}_a^n + \frac{\Delta t}{2} \vec{F}_a^n \quad (2.31)$$

$$\vec{r}_a^{n+1/2} = \vec{r}_a^n + \frac{\Delta t}{2} \vec{V}_a^n \quad (2.32)$$

These values are then corrected using derivatives estimated at the half step

$$\vec{v}_a^{n+1/2} = \vec{v}_a^n + \frac{\Delta t}{2} \vec{F}_a^{n+1/2} \quad (2.33)$$

$$\vec{r}_a^{n+1/2} = \vec{r}_a^n + \frac{\Delta t}{2} \vec{V}_a^{n+1/2} \quad (2.34)$$

Finally using the values of velocity and position from the predictor and corrector step, one can obtain the values at the end of the time step by,

$$\vec{v}_a^{n+1} = 2\vec{v}_a^{n+1/2} - \vec{v}_a^n \quad (2.35)$$

$$\vec{r}_a^{n+1} = 2\vec{r}_a^{n+1/2} - \vec{r}_a^n \quad (2.36)$$

### 2.3.7. Moving the particle

The particles are moved using XSPH variant [21] where the particle is not moved with its own velocity but using an average velocity which also takes into account the velocity of the nearby particles and is given by,

$$\frac{d\vec{r}_a}{dt} = \vec{v}_a + \varepsilon_{coef} \sum \frac{m_b}{\bar{\rho}_{ab}} \vec{v}_{ba} W_{ab} \quad (2.37)$$

where  $\varepsilon_{coef}$  is 0.5 (standard value used in various studies) and  $\bar{\rho}_{ab} = (\rho_a + \rho_b) / 2$ . The method moves the particle with a velocity close to the neighbourhood and helps in avoiding inter-penetration of particles.

### 2.3.8. Kernel

The accuracy and stability of an SPH code is highly dependent on the choice of the kernel function. They should satisfy several conditions such as positivity, compact support, and normalization. Also,  $W_{ab}$  of a particle  $a$  should monotonically decrease with increasing distance from the particle and behave like a delta function as the smoothing length  $h$ , tends to zero [22-24]. The value of the Kernel function depends on the smoothing length  $h$ , and the non-dimensional distance between particles given by  $q = r/h$ ,  $r$  being the distance between particles  $a$  and  $b$ . The parameter  $h$ , often called smoothing length, controls the size of the volume around particle  $a$  where contribution from the rest of the particles is considered, outside the radius  $h$  the contribution of the particles is either zero or negligible.

A cubic spline kernel has been used in the present work,

$$W(r, h) = \alpha_D \begin{cases} 1 - \frac{3}{2}q^2 + \frac{3}{4}q^3 & 0 \leq q \leq 1 \\ \frac{1}{4}(2-q)^3 & 1 \leq q \leq 2 \\ 0 & q > 2 \end{cases} \quad (2.38)$$

where  $\alpha_D = 2/(\pi h^2)$  in 2D and  $\alpha_D = 5/(4\pi h^3)$  in 3D.

### 2.3.9. Computational linked list method

SPH codes are based on interactions with closed neighbours. These interactions are based on the distances between the interaction points called particles. Such interactions require a loop through particles to check whether or not they lie within the kernel so as to consider the weightage of the interpolation contributions. An overly simple solution would be to loop through all the particles to have such an interaction possible, however that would lead to an extremely inefficient code with extremely high computational times. Hence to make the system much more efficient we use a link list method for particle search and interactions (Monaghan and Latanzio 1985 [25]). In the present work the computational domain is divided in square cells of side  $2h$  (see Figure 2.3). Thus, for a particle located inside a cell, only the interactions with the particles of neighbouring cells need to be considered. In this way the number of calculations per time step and, therefore, the computational time diminish considerably, from  $N^2$  operations to  $N \log N$ ,  $N$  being the number of particles.

Around each cell, the E, N, NW & NE neighbouring cells are checked to minimise repeating the particle interactions. Thus, for example, when the centre cell is  $i=5$  and  $k=3$  (see scheme in Figure 2.4 where leftmost column refers to  $i = 1$  and lowest row refers to  $k = 1$ ), the target cells are  $(5,4)$ ,  $(4,4)$ ,  $(6,4)$  and  $(6,3)$ . The rest of the cells were previously considered through the sweeping (e.g. the interaction between cell  $(5,3)$  and  $(5,2)$  was previously accounted when  $(5,2)$  was considered to be the centre cell).

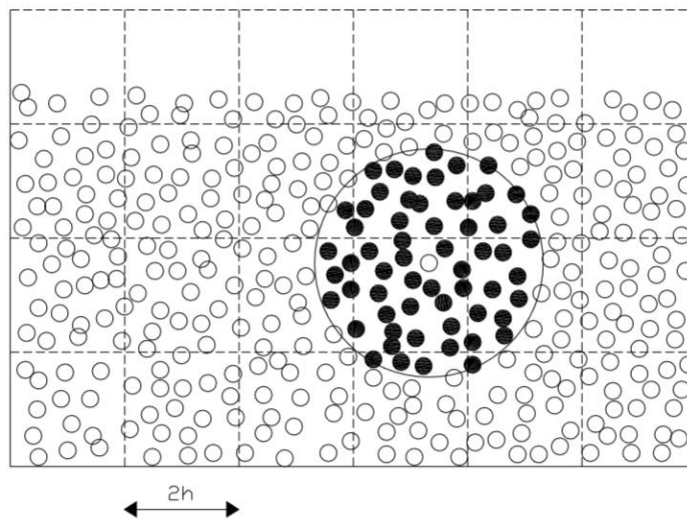


Figure 2.3. Set of neighbouring particles in 2D. The possible neighbours of a fluid particle are in the adjacent cells but this only interacts with particles marked by black dots.

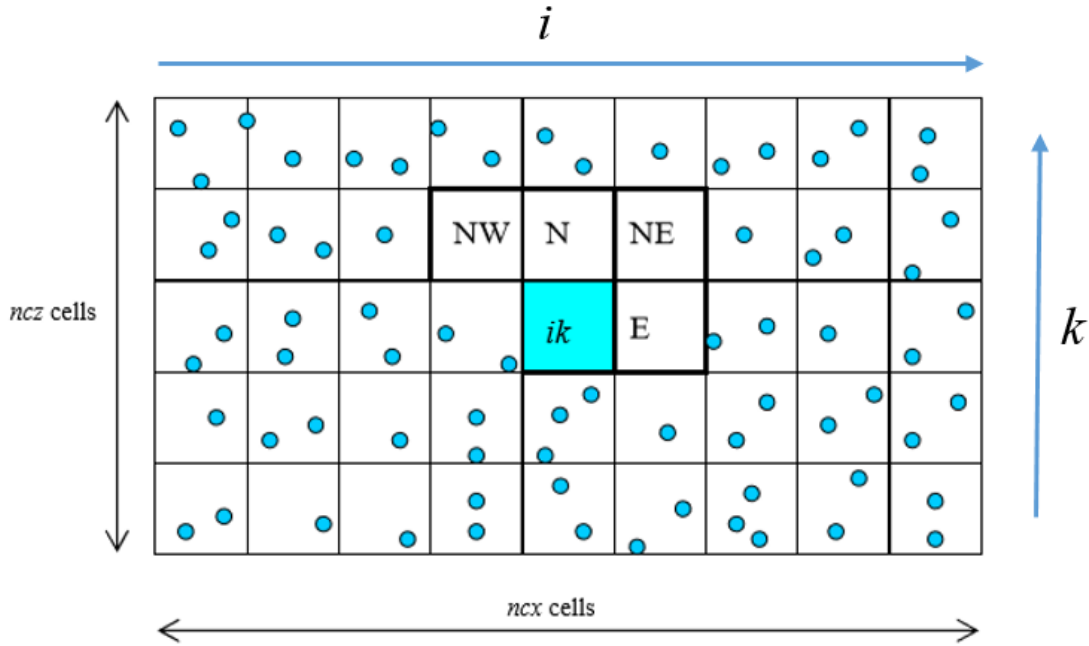


Figure 2.4. Sweeping through grid cells in 2D. Starting from the lower left corner, particles inside the centre cell  $ik$  interact with adjacent cells only in E, N, NW and NE directions. The interactions with the rest of the cells W, S, SW & SE directions were previously computed using reverse interactions.

### 2.3.10. Boundary condition in SPH

Two kinds of boundary conditions have been used in the present study: (i) Dynamic Boundary conditions (Crespo *et al.*, 2007 [26], Dalrymple and Knio, 2000 [27]); (ii) Repulsive boundary conditions (Monaghan & Kos, 1999 [28], Rogers & Dalrymple 2008 [29]).

#### 2.3.10.1. Dynamic Boundary Conditions

In this method, boundary particles satisfy the same equations as fluid particles. Thus, they follow the momentum equation, the continuity equation and the equation of state. However, they do not move according to Eq. 2.37. They remain fixed in position (fixed boundaries) or move according to some externally imposed function (moving objects like gates, wavemaker etc.). When a particle approaches the boundary, the density of the boundary particle increases according to the continuity equation that results in an increase in pressure. This boundary particle then exerts a higher force on the inner particles due to its higher pressure, this in a way acts as a repulsive force on the inner particle. For example, a wall in SPH can be made up of such particles and could keep the inner particles from leaving the domain or entering an obstacle. However, the need to solve the fluid or solid equation for each of the boundary particles could increase the computational time.

### 2.3.10.2. Repulsive Boundary Conditions

This type of boundary condition was developed by Monaghan 1994 [86] to ensure that the particles never cross the boundary. Similar to inter-molecular forces, the boundary particles exert a central force on the inner particles. No equation is solved for the boundary particles and hence the only interaction the boundary particles have with the inner particles is the repulsive force on the inner particle. Thus, for a boundary particle and an inner particle separated by a distance  $r$ , the force for unit of mass has the form given by the Lennard-Jones potential. In a similar way, other authors (Peskin, 1977 [87]) express this force assuming the existence of forces in the boundaries, which can be described by a delta function. This method was refined in Monaghan and Kos (1999) by means of an interpolation process, minimizing the interspacing effect of the boundary particles on the repulsion force of the wall.

The force experienced by an inner particle normal to the wall is given by the following,

$$\vec{f} = \vec{n}R(\psi)M(\xi)\varepsilon(u_{\perp}) \quad (2.39)$$

where  $\vec{n}$  is the normal to the wall. The distance  $\psi$  is the shortest distance of the particle from the wall,  $u$  is the velocity of the inner particle projected onto the normal. The repulsive function,  $R(\psi)$ , is calculated using the normalized distance from the wall ( $q=\psi/2h$ ) and is given by,

$$R(\psi) = A \frac{1}{\sqrt{q}}(1-q) \quad (2.40)$$

where the coefficient  $A$  is given by,

$$A = \frac{1}{h} 0.01c_i^2$$

$c_i$  being the speed of sound corresponding to particle  $i$ .

The function  $M(\xi)$  is chosen such that the inner particle would experience a constant repulsive force as it travels parallel to the wall

$$M(\xi) = \frac{1}{2} \left( 1 + \cos \left( \frac{2\pi\xi}{\Delta b} \right) \right) \quad (2.41)$$

where  $\Delta b$  is the distance between any two adjacent boundary particles. The function  $\varepsilon(u_{\perp})$  is a modification to Monaghan and Kos's scheme and it takes into account the velocity of the particle normal to the boundary.

$$\varepsilon(u_{\perp}) = \alpha_D \begin{cases} 0 & u_{\perp} > 0 \\ |20u_{\perp}|/c_0 & |20u_{\perp}| < c_0 \\ 1 & |20u_{\perp}| > c_0 \end{cases} \quad (2.42)$$

### Chapter Highlights

- This chapter provides an overview of the SPH method
- The SPH method for both fluid and solid has been discussed, details on the solution algorithm have been provided.

# 3 CAVITATION AND CAVITATION EROSION

This chapter introduces cavitation and cavitation erosion to the readers. The chapter covers various aspects of cavitation that are relevant to the thesis, including the cavitation phenomenon, different kinds of cavitation, numerical studies in cavitation and cavitation erosion and eventually a brief description on fluid structure interaction in cavitation.

## 3.1. Cavitation

Cavitation erosion is a major issue amongst a wide range of equipment such as hydraulic devices, diesel injectors, artificial heart valves etc. Cavitation is defined as the appearance of vapour cavities inside a continuous and homogeneous liquid medium. The generation of vapour cavities could happen due to various reasons, but the cause is mostly associated to the drop of local pressure below the vapour pressure. Figure 3.1 shows a pressure-temperature phase diagram of water and a drop of pressure below the vapour pressure leads to vaporization of liquid commonly known as cavitation. During cavitation the continuum liquid medium breaks down to form vapour cavities.

However, the general view is that the formation of these cavities is not just due to the drop in pressure but also because of the presence of cavitation nuclei in the liquid. These nuclei are typically gas microbubbles present in the liquid as dissolved gas. Cavitation can hence generate at these favourable locations such as the gas microbubbles or even discontinuities for example near a solid liquid interface. Studies have shown that a degassed liquid can sustain tens of MPa in dropped pressure without breaking into such vapour cavities [30-33]. When present, these gas nuclei can grow rapidly as the pressure in the liquid reduces forming microscopic bubbles. These bubbles will keep growing until the ambient pressure in the liquid rises above the pressure inside the vapour cavity. Once the pressure in the ambient liquid is higher, the vapour cavity starts to collapse and can eventually lead to the formation of high velocity micro jets and high intensity shock waves. Rayleigh [34] has explained the generation and explosion of such spherical cavities from a theoretical standpoint leading to shock wave generation. Harrison [35] in 1952 experimentally showed the evidence of shock wave emission during a cavitation bubble collapse. The formation of micro jet for a bubble close to a solid surface has been shown in various studies [1-2, 36-39], Figure 3.2 shows a schematic description of a collapsing bubble and the resulting micro jet.

It is the difference in the pressure inside and outside the vapour cavity that drives the bubble collapse. However, the pressure acting on the bubble might not be the same on all sides specially under the presence of a solid surface near the bubble. For example, a bubble near a wall does not have enough liquid inflow from the surface close to the wall as compared to the surface away from the wall. Such a difference in the liquid flow can lead to an asymmetric collapse of the bubble, first numerically solved by Plesset and Chapman [40]. Thereafter there have been various studies conducted to understand the mechanism of an asymmetric bubble collapse near a solid surface [11, 41-42]. Philipp and Lauterborn [1] have presented in detail the experimental investigation of the influence of a solid boundary on bubble collapses. They observed that the pressure gradient along the boundary leads to different accelerations of the bubble surface closest and farthest to the wall which ultimately moves the bubble towards the boundary. So not only does the solid boundary lead to a micro jet formation directed towards the wall but also a translation of the bubble itself towards the solid boundary. Such a translational movement of bubbles during collapse was first introduced by Shutler & Mesler [43] and is considered to be able to enhance the damaging effect of bubbles collapsing relatively away from the solid boundary.

During such a collapse, the solid surface experiences a high pressure due to the shock wave or the high velocity micro jet hitting the surface. The magnitude of the pressure acting on the surface could be high enough to cause plasticity and eventually damage to the solid material. Although the experimental measurement of these pressures acting on the surface still remains a challenge, various studies have estimated it to be around a few GPa [1-5].

### **3.2.Scales of cavitation studies**

Cavitation is a phenomenon that can occur at various scales simultaneously ranging from a micro scale of a single cavity to a large cavitation sheet ranging tens of centimetres in length on turbines blade or a hydrofoil. Hence cavitation studies can focus on various scales of cavitation, ranging from a study of a cavitating flow over a hydrofoil to a single cavity collapse. For example, various types of cavity structures can be observed over a hydrofoil [44]. Depending upon the operating conditions (angle of attack, flow speed, nuclei content, etc.), either isolated cavitation bubbles as shown in Figure 3.3 or attached sheet cavitation can be observed. If the number of bubbles is large, they eventually merge together to form a sheet cavity. Depending on the length of the attached cavity, this cavitation pattern is classified in partial cavity or super cavity. It is known as a partial cavity if the cavity length finishes on the cavitator wall (see Fig. 3.4). On the contrary if the cavity closes inside the liquid, downstream

of the cavitator, it is known as super cavity (see Fig. 3.5). In this thesis we will focus on a single bubble collapsing over a solid surface and we will numerically estimate the plastic deformation and damages caused by such a collapsing bubble.

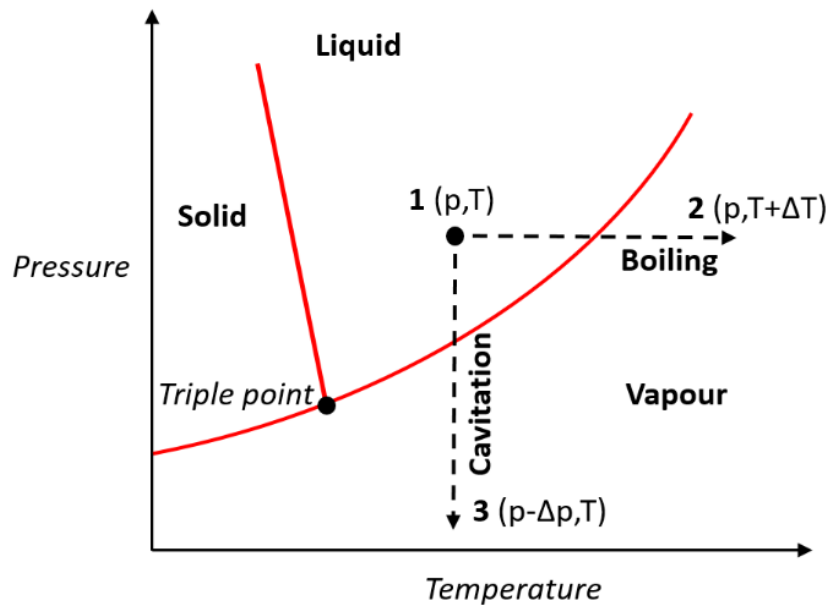


Figure 3.1. Pressure-temperature phase diagram for water showing the two forms of vaporization in water, namely, boiling (state 1 to state 2) and cavitation (state 1 to state 3).

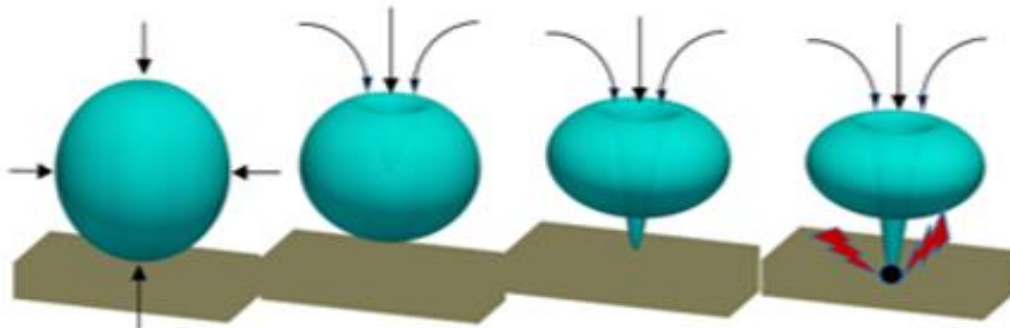


Figure 3.2. Collapse of a single cavitation bubble near a surface.

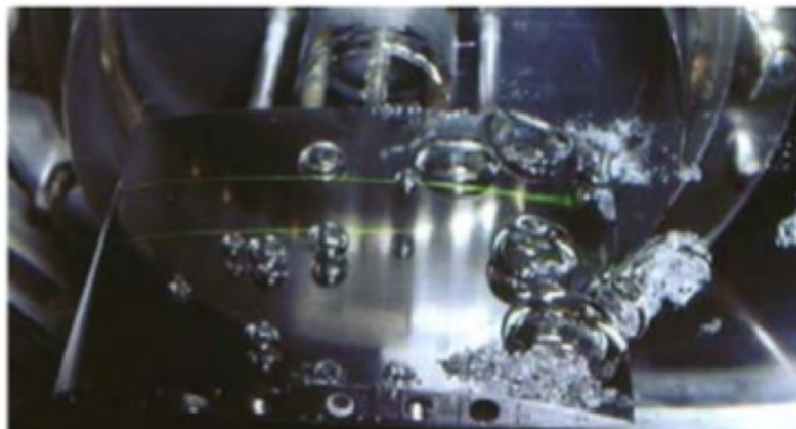
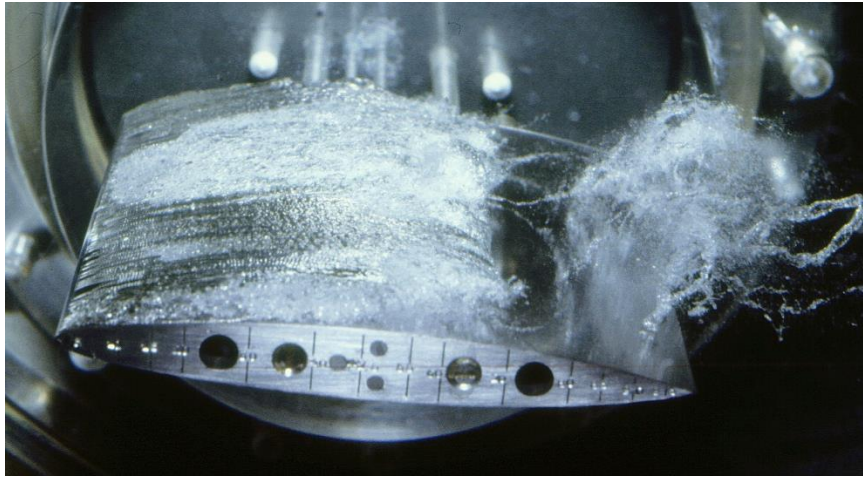
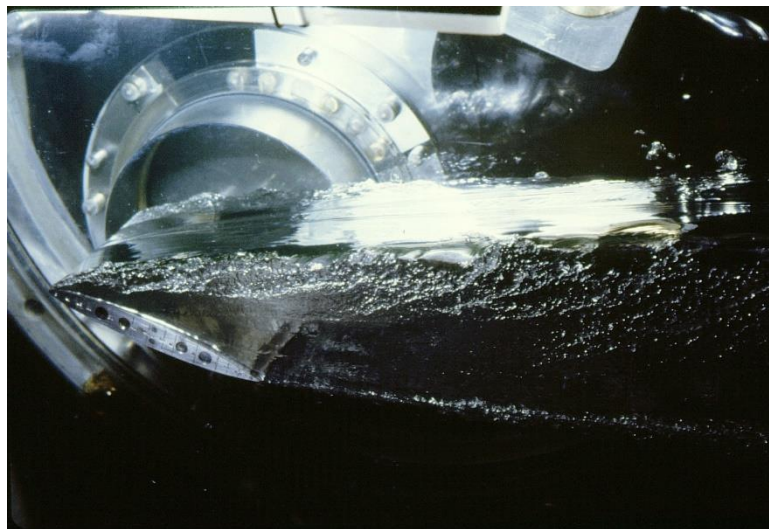


Figure 3.3. Isolated cavitation bubbles over a hydrofoil [44].



*Figure 3.4. Partial cavity sheet over a hydrofoil [44].*



*Figure 3.5. Supercavity sheet over a hydrofoil [44].*

### **3.3. Rayleigh-Plesset collapse**

Cavitation bubble dynamics can be analysed analytically while making a few assumptions. Rayleigh [34] developed the theory of the dynamics of an empty spherical bubble in an incompressible and inviscid liquid medium. He derived analytical equations to interpret the phenomenon of the bubble collapse. Later Plesset [45] derived new equations for bubble dynamics by modifying the Rayleigh equation and including surface tension, later also adding viscous effects [40].

### **3.4. Cavitation erosion**

Understanding cavitation erosion and damage in the material is extremely important to develop techniques to inhibit cavitation erosion. As mentioned earlier, formation of micro jets and shock waves due to the presence of a solid wall near the bubble surface can result in high

intensity loads on the solid wall. The intensity or the magnitude of the load depends on various parameters such as bubble size, distance of the bubble surface from the wall and the pressure gradient driving the collapse. The magnitude of the loads could be a few GPa and hence could lead to significant plastic strain in the material leading to formation of cavitation pits at the surface. However, impact loads due to one single collapse is rarely significant enough to produce damage or cavitation erosion. It is more likely to be the consequent loading cycles due to multiple collapses that leads to plastic strain accumulation and eventually damage propagates through the material leading to complete failure called cavitation erosion. To demonstrate the magnitude of the problem and the extent of damage it can cause, some examples of cavitation erosion are shown in Figures 3.6 & 3.7.



Figure 3.6. Images provided by Delphi Diesel Systems UK and showing cavitation erosion at the exit of an injection hole together with an impression made of the inside of the damage hole in a Diesel fuel injector (taken from Grant agreement of CaFE project grant no. 642536).

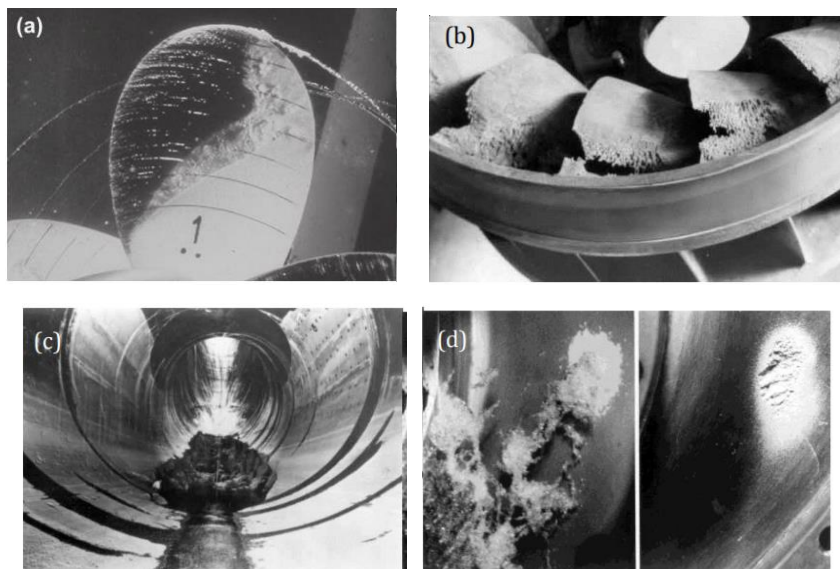


Figure 3.7 (a) Sheet and cloud cavitation damage together with a tip vortex on a propeller blade [46]; (b) Cavitation damage on the blades at the discharge from a Francis turbine; (c) Cavitation damage to the concrete wall of the 15.2m diameter Arizona spillway at the Hoover Dam; (d) Axial

views from the inlet of the cavitation and cavitation damage on the hub or base plate of a centrifugal pump impeller [47].

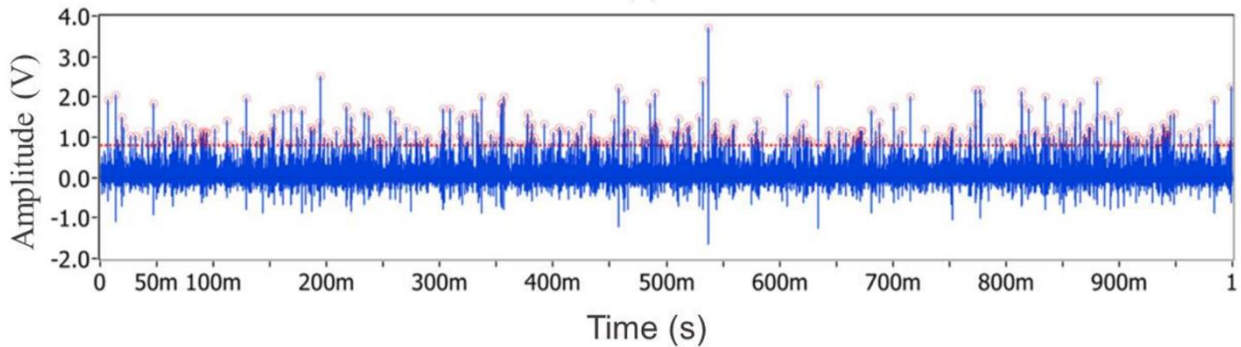


Figure 3.8. Impact load signals recorded by a piezoelectric pressure sensor in a cavitation tunnel operating at flow pressure of 40 bar. The circles show the signals above a threshold of 0.8 V [48].

A random cycle fatigue is an appropriate analogy to the kind of loading the material is subjected under cavitation conditions. The impact loads are observed to be between zero and a compressive load surface pressure with random magnitude and time intervals between two loads corresponding to different bubble collapses. Figure 3.8 below shows a typical signal recorded by a piezoelectric pressure sensor (PCB 108A02) subjected to cavitation erosion [48]. Each peak with a positive amplitude in Volts represents an impact due to a cavitation bubble collapse and the negative peaks are due to ringing of the transducer. The red horizontal line at 0.8 V is a threshold value obtained by the piezoelectric sensor marked to avoid background noise and weak pulses which might not result in cavitation pits. The only difference with the completely reversed cycle fatigue is that there is no tension loading or in other words no reversing of the applied loading cycle, the loads vary between zero and a positive value instead of a negative and a positive value. [49, 50]. Although there are no tension loads during the cavitation load cycle, the surface geometry changes with each impact and the random location of impacts may result in reverse straining of the material close to the surface or at least to stress triaxiality fluctuations. Under such a scenario, the plastic strain accumulation may not occur evenly with successive impacts.

### 3.5. Experimental Measurement of Cavitation Erosion

There are various kinds of cavitation erosion tests that can be performed to evaluate the vulnerability of a certain material under cavitation loads in general. However, to understand the erosion patterns in a particular flow specific to a given machinery, tests can be conducted on the field as well. These field methods need elaborate planning and hence are expensive to

design and conduct. This has led to various laboratory test techniques for cavitation erosion. Some of the standard test procedures include: ultrasonic vibratory devices, rotating discs and cavitation liquid jets [5, 51-55]. The following section provides a brief introduction to the vibratory test method and cavitating liquid jet method.

The vibratory test method works on the principle that vibrating an object at a high frequency while inside a liquid can lead to cavitation. In this method, a horn is used to stimulate cavitation which is connected to an ultrasonic transducer which vibrates at a high frequency. Figure 3.9 shows a schematic of a vibratory erosion test. The methods being relatively cheap, portable, simple and rapid makes it popular. It can be used to test cavitation erosion resistance of different materials. However, the cavitation generation is very different from that in actual cases of hydraulic machineries and hence the test does not give a complete picture of the cavitation erosion phenomenon.

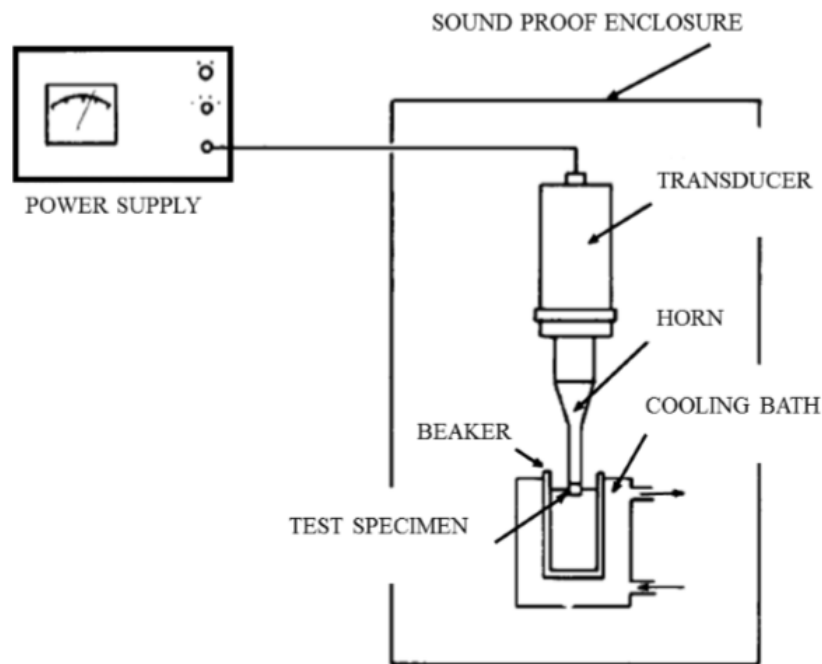


*Fig. 3.9 Schematic of vibratory cavitation erosion apparatus [56].*

Another standard test method that can provide some more information on the cavitation erosion and leads to similar cavitation clouds as in hydraulic equipment is a cavitating liquid jet system [58]. The cavitation is produced by a submerged cavitation jet that impinges on a test specimen which will be eroded due to numerous cavitation bubble collapses. A suitably designed cylindrical bore nozzle is used to generate a high velocity liquid jet. Cavitation is observed in the vena contracta region of the jet which eventually collapses on the test specimen. Vena contracta is referred to as the region where the diameter of the nozzle is the minimum, leading

to the highest velocity and the lowest pressure occurring along the length of the nozzle. The lowering of pressure at the vena contracta can escalate the generation of the cavities and these cavities can then collapse on the test specimen leading to material erosion. The formation of cavities can be attributed to the shear layer between the high velocity jet and the (almost) immobile surrounding water. Shear leads to the formation of vortices, whose core is a region of low pressure, where cavitation bubbles will grow preferably.

As apparent from the design, this method provides flexibility in controlling and changing a few parameters like the jet velocity, angle of impingement, standoff distance and downstream pressure [58]. Figure 3.10 shows the schematic of the test chamber of a typical cavitating liquid jet apparatus [58]

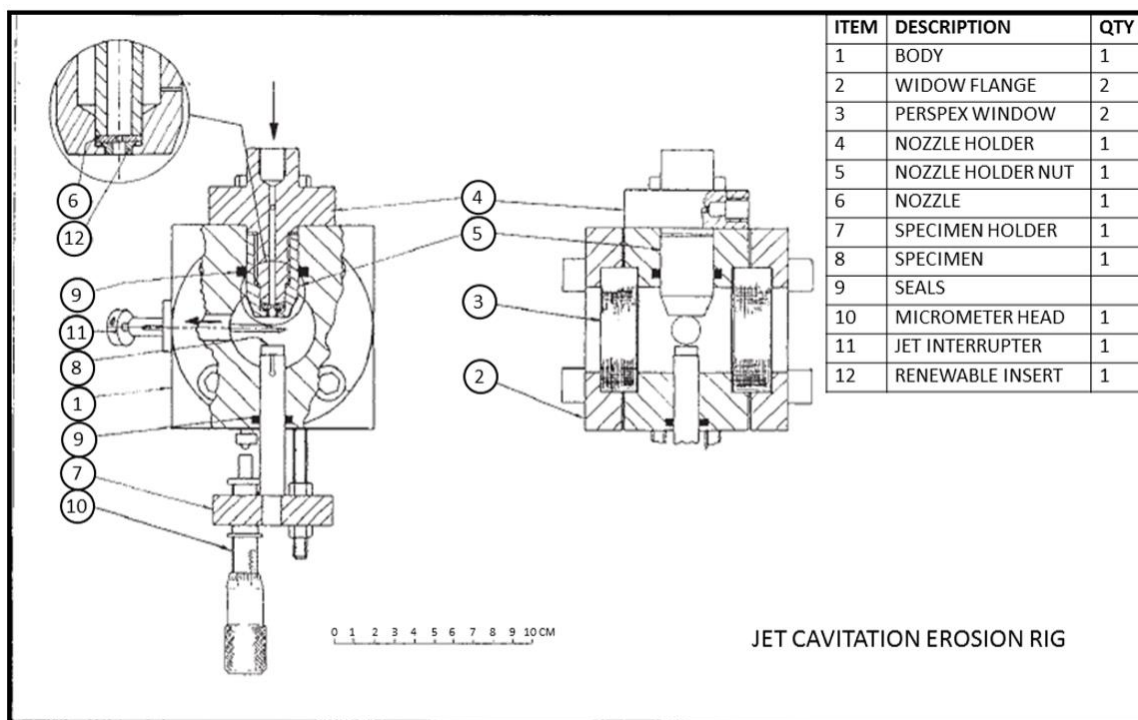


Fig. 3.10 Test chamber assembly of cavitating liquid jet apparatus [58].

These devices can produce standard conditions to test materials. However, in reality the cavitation pattern can vary from equipment to equipment and even for the same equipment could vary under different testing conditions. Even though these tests can be used to assess materials resistance to cavitation erosion, a thorough understanding of cavitation erosion for a specific equipment would require information like type and size of cavities formed under different conditions, the resulting pressure on the solid surface due to these cavity collapses and eventually linking how cavitation loading leads to cavitation erosion. Amongst the three pieces of the puzzle, the type and size of cavities can be estimated with visualization

techniques, cavitation erosion can also be measured using surface visualization/detection techniques. However, the experimental load measurement on the solid surface still remains a challenge.

One of the measurement techniques uses a pressure sensor directly at the wall of the test specimen, some studies have used pressure transducers made up of piezoelectric material with a rise time of the order of 1 micro second and a natural frequency of around 400 kHz [38,48]. The studies however pointed out various difficulties with such pressure transducers. The primary problem is that the sensitive tip of these transducers which measures the pressure is of the order of mm in radius. However the collapsing bubbles and therefore the loading radius is significantly smaller than the transducer tip. Hence the pressure sensor response cannot be related to one single collapse as the reading could be a result of multiple collapses located inside the sensor area. Secondly, the pressure sensor has to be flush mounted on the surface in order to not produce any geometrical inconsistencies, however this is a challenging task as any deviation from flushing at the surface might result in deviations in the output. Moreover, the output of the transducer is at a certain point on the surface hence only the temporal evolution and not the radial spread of pressure can be studied. Finally, the output of these transducers is given in terms of force which is then converted to stress by dividing the force by the tip area of the transducer and also accounting for any other calibration the manufacturer specifies. This assumes that the load over the transducer is uniformly distributed, but in reality the applied stress can have a complex distribution and hence the resulting stress might not be very accurate. Since most experimental methods have difficulties in producing the pressure signal, numerical methods can also be used to do the same. Modelling cavitation using CFD is a common technique to estimate pressure at the wall, these data can then be used to estimate the material response by using different methods and models for cavitation erosion prediction. These models could include empirical models, phenomenological models and numerical methods and will be discussed in the following section.

### **3.6. Empirical models**

These are simplistic models that try to relate the results from a standard cavitation test to the mechanical properties of the material such as yield stress, Young's Modulus, hardness, toughness etc. Other kinds of model empirically relate the erosion resistance (ability of the material to resist erosion under cavitation loading) to the pitting rate or flow aggressiveness without considering material properties [59-61]. Some of these methods will be discussed in this thesis in order to give a general overview.

One such study provided a review of erosion tests on various materials using standard test methods [62]. They plotted erosion resistance of metallic alloys against the Vickers Hardness ( $HV$ ) on a log-log scale and found the relationship to be linear in terms of log of erosion resistance and log of  $HV$ . The maximum mean depth of erosion rate ( $MDER_{\max}$ ) refers to the inverse of the erosion resistance, the coefficients in the equation below could be different for different classes of material and should be determined experimentally.

$$MDER_{\max}^{-1} = 2.6 \times 10^{-7} \times HV^{2.4} \quad (3.1)$$

Okada *et al.* [63] have developed a pressure transducer mounted with a test specimen that can record impact forces and erosion damage due to cavitation bubble collapses. By correlating the impact loads with indent sizes in decreasing order of magnitudes, they have shown that an empirical relationship between cumulative volume loss and cumulative impact energy can be established, which is linear in nature and independent of test apparatus and test condition. Although the arbitrariness in correlating impact loads with indent size could be argued, the method provides a simple way to predict cavitation erosion based on the measurement of cavitation impact loads.

As said previously, cavitation erosion is a fatigue like phenomenon and material erosion should not just depend on material properties or just the magnitude of the loads but also on the cyclic feature of the loading. Hattori [59] proposed a method to use the cavitation impact force to predict the incubation period. The relationship between the impact force and the number of impacts at failure is supposed to be given by the following equation:

$$F_i^\alpha N_i = C_1 \quad (3.2)$$

where  $N_i$  is the number of impacts at failure for impact force of  $F_i$  amplitude,  $\alpha$  and  $C_1$  are two empirical constants depending on the material. The number of impacts  $N_i$  corresponds to the number of impacts at the end of the incubation period after which material erosion starts. Then, under repetitive cavitation loadings the erosion is given by Miner's linear cumulative damage law, which is

$$D = \sum \frac{n_i}{N_i} \quad (3.3)$$

Where  $n_i$  is the number of impacts at amplitude  $F_i$ . However, it is obvious that none of the standard test could produce a constant force  $F_i$  and hence the model cannot produce reliable results in realistic cases.

### 3.7. Phenomenological models

Most of the empirical models do not take into account fluid aspects in the cavitation process, however it is obvious that material erosion does not only depend on the material properties but also on the cavities in the fluid and the phenomenon of cavitation on the fluid side. Hence models that can account for both the fluid phenomenon and the solid phenomenon of cavitation were developed and are known as phenomenological models [44, 64-66].

Franc and Michel [44] simplified a model initially proposed by Karimi and Leo [64] which is applicable in the steady state region of cavitation erosion. First, any load lower than the yield stress of the material is considered to not produce any plastic deformation. Then, under the impacts of higher magnitude ( $>\sigma_Y$ ), the material undergoes plastic deformation and when the accumulated plastic strain reaches the fracture strain ( $\epsilon_f$ ), a complete damage resulting in material removal is assumed. To take into account the fluid effect, the flow aggressiveness is defined by three parameters: a mean value of the impact stresses ( $\sigma_{mean}$ ), a mean value of the impacted areas ( $A_{mean}$ ) and their rate ( $N$ ) per unit time and unit surface area. This model uses average values and hence the details about time temporal distribution and spatial distribution of loads were not taken into account. These flow parameters can be estimated by using pressure transducers along with the target material. The time required ( $t_{cov}$ ) for such a mean impact load of ( $\sigma_{mean}$ ,  $A_{mean}$ ) at a rate of  $N$  to completely cover the material surface is  $1/(NA_{mean})$  which is one cycle time, after which a layer of the material is considered to have hardened uniformly. The strain profile into the hardened layer is given by the following equation

$$\epsilon = \epsilon_s \left(1 - \frac{x}{L}\right)^\theta \quad (3.4)$$

Where,  $\epsilon_s$  is the strain at the surface of the material,  $x$  indicates distance or depth from the surface,  $L$  is the thickness of the hardened layer and  $\theta$  is a measure of the steepness of the hardening gradient.

Following each cycle, an increase in the thickness of the hardened layer is observed. Thus values of  $\epsilon_s$  and  $L$  will increase continuously following the same strain profile until damage is initiated at the surface. Once damage is initiated the thickness of the hardened layer ( $L$ ) will remain constant. Now considering that the plastic strain varies from zero to the fracture strain ( $\epsilon_f$ ) in the thickness  $L$ , and in the steady-state period the material is being subjected to a mean impact load of ( $\sigma_{mean}$ ,  $A_{mean}$ ) eroding  $\Delta L$  thickness of the material from the surface, the strain profile given by equation 3.4 would give,

$$\varepsilon_f = \varepsilon_{mean} \left( 1 - \frac{\Delta L}{\Delta L + L} \right)^\theta \quad (3.5)$$

Where  $\varepsilon_{mean}$  is the plastic strain on the surface of the removed layer.

Considering a Ludwig type constitutive law for the material which is given by the following,

$$\sigma = \sigma_Y + K\varepsilon^n \quad (3.6)$$

Using equations 3.5 and 3.6 we can re-write the thickness of the eroded layer as,

$$\Delta L = L \left( \left( \frac{\sigma_{mean} - \sigma_Y}{\sigma_f - \sigma_Y} \right)^{1/n\theta} - 1 \right) \quad (3.7)$$

The mean depth of penetration rate (*MDPR*) which represents volume loss per unit surface area per unit time,

$$MDPR = \frac{\Delta L}{t_{cov}} = NA_{mean} L \left( \left( \frac{\sigma_{mean} - \sigma_Y}{\sigma_f - \sigma_Y} \right)^{1/n\theta} - 1 \right) \quad (3.8)$$

Although, the model takes into account the fluid and the solid phenomenon, it fails to match the experimental results [64]. Considering the complex phenomenon of cavitation and the various aspects not considered in the model, much better ways are needed to model material erosion. This can be achieved using numerical techniques for both the fluid and solid. An overview of such techniques is presented in the next section.

### 3.8. Numerical simulations

Numerical simulation of fluid cavitation has developed immensely over the years together with the continuous increase of computer power. The pressure obtained from a fluid simulation can then be used for solving the solid numerically in order to estimate the material erosion. There are broadly two approaches to the solving for material loss numerically. The first approach involves solving just the solid using pressure from the fluid or using a suitable pressure distribution. The second approach offers a much better alternative by solving both the fluid and solid systems together (fluid structure interaction).

An interesting work by Roy *et al.* [68] focussed on an inverse approach using Finite Element Method where it is assumed that the dimension of the cavitation pit is related to material property and a Gaussian pressure distribution. Once a dimension of a pit is known, using an inverse calculation the pressure distribution could be calculated, where the pressure is given by the following over the pit,

$$\sigma = \sigma_H \exp\left(-\left(\frac{2r}{d_H}\right)^2\right) \quad (3.9)$$

Where,  $\sigma_H$  is the maximum amplitude of the hydrodynamic impact pressure and  $d_H$  is the diametric extent of the load as shown in Figure 3.11.

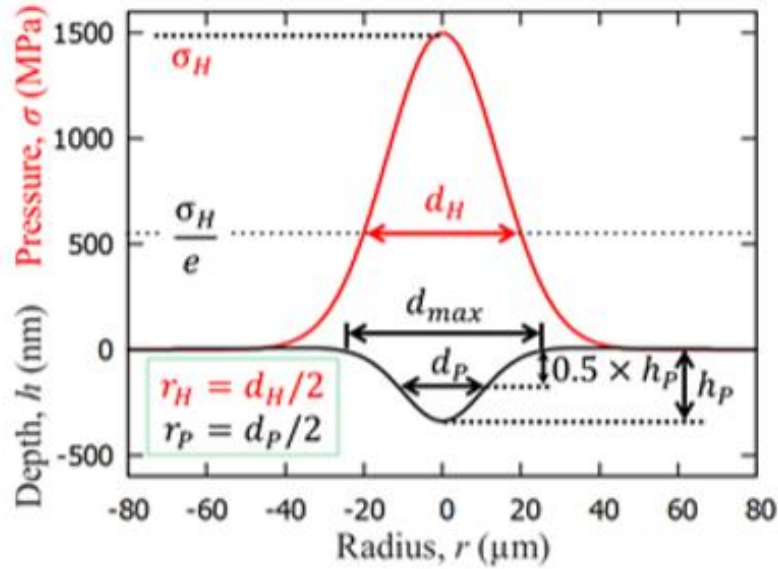


Figure 3.11 Gaussian shape of the hydrodynamic impact pressure and resulting cavitation pit. Here  $d_{max}$  represents the maximum diameter of the pit [68].

Roy *et al.* [69] also tried dynamic loading of the material using FEM, where they added a temporal evolution to the pressure, modifying equation 3.9 to the following equation,

$$\sigma = \sigma_H \exp\left(-\left(\frac{2r}{d_H}\right)^2\right) \exp\left(-\left(\frac{t - t_{max}}{t_H}\right)^2\right) \quad (3.10)$$

Where  $t$  is time and  $t_{max}$  is the time when  $\sigma = \sigma_H$  and  $t_H$  is the characteristic impact rise duration in a similar way  $d_H$  represents the radial spread of the load. They found that at high frequency or small characteristic time, the pits formed for the same pressure and radial spread appear to be smaller than the pits for the static case (without temporal evolution of pressure). They observed that strain rate sensitivity and inertial effects lead to lower plastic straining in case of high frequency loading. In case of fast loading, the inertial effects play an important role where significant amount of energy goes into kinetic energy instead of plastic energy and leads to lower plastic strain. On the other hand, higher strain rate leads to increase in yield stress leading to larger elastic deformation and lower plastic strain for the same load at a higher frequency. A similar FEM study was carried out by Pöhl *et al.* [70], where FEM simulations are carried out in order to determine the load based on a similar inverse loading algorithm. They found

that the pit obtained from the vibratory apparatus is related to a maximum pressure in the range of 2400 MPa to 3500 MPa using their inverse algorithm. FEM simulations and the inverse approach method can give some insights into the cavitation erosion phenomenon, although a complete understanding would require a fully coupled fluid structure interaction (FSI) solver. To understand the phenomenon of cavitation erosion in its entirety for a large scale machinery is still not within the purview of feasibility considering the humongous computational effort required for a fully coupled and fully resolved computation. Hence the initial footstep towards a numerical understanding using FSI would be to understand the cavitation erosion phenomenon for a single cavitation bubble. Some studies have attempted to develop a cavitation FSI solver wherein both fluid and solid response can be captured [11,42,67]. In order to solve for the fluid bubble collapse, they use three codes: two fluid solvers, namely, boundary element method code (3DYNAFS-BEM) and a finite difference code (GEMINI), for the solid response they use a finite element code (DYNA3D). The aim of having two fluid solvers is to create a hybrid scheme wherein the bubble collapse is solved using two different schemes which depend on the kind of system to be solved. Cavitation bubbles create no shock waves during the growth phase and even during the collapse the shock wave is generated towards the end of the collapse. Hence they use the incompressible BEM [71-73] until the end of the collapse where the flow is mostly incompressible. Once the shock wave generation is expected, the solver is switched to a compressible finite difference element [74]. The solid solver takes the pressure distribution as an input at each iteration and then solves for the material response. The code solves the material using a linear isotropic hardening law, however most materials exhibit non-linear isotropic hardening which is one of the drawbacks of the model as it cannot capture non-linear hardening effects. Also the code does not consider strain rate hardening effects which are significant for fast dynamic phenomena like cavitation erosion. Roy *et al.* [69] demonstrated for a dynamic phenomenon such as cavitation erosion that the strain rate hardening effect are significant and hence should be included in the material models to simulate cavitation erosion. However, it would be interesting to observe how significant these effects could be for an FSI simulation of a single cavity collapse.

Turangan *et al.* [13] studied fluid structure interaction using a Free-Lagrange scheme, FLM, that incorporates the compressibility, multi-phases and elastic plastic solid models and they simulated the collapse of 40  $\mu\text{m}$ -radius single bubbles attached to/near rigid and aluminium walls by a 60 MPa-lithotripter shock, and the collapse of a 255  $\mu\text{m}$ -radius bubble attached to a 25  $\mu\text{m}$ -thick aluminium foil by a 65 MPa-lithotripter shock. They simulated the bubble collapse with different stand-off distance and found that the attached cavity can produce larger

deformation compared to a detached cavity. However, the material constitutive behaviour is simplified to perfectly plastic and does not follow Johnson Cook criteria and hence cannot consider neither non-linear hardening nor strain rate sensitivity which are known to cause significant deviations in the results.

A recent thesis [88] has focused on using SPH for cavitation bubble simulation in fluid and FEM for the solid in 2D. However, using the same method i.e. SPH for both fluid and solid would be interesting and a less exhausting computational process in terms of coupling the two codes. Moreover, the solver is developed in 2D which does not represent an actual spherical cavity but an infinitely long cylindrical cavity.

## **Chapter Highlights**

- This chapter provides an overview of cavitation and cavitation erosion.
- Experimental studies of cavitation are vital but can only provide limited information due to the lack of appropriate measurement procedure for a fast phenomenon like cavitation. Hence numerical methods are commonly used to gain more insight into the phenomenon.
- There is an abundance of numerical studies for fluid cavitation but a lack of a complete understanding of the erosion phenomenon since there has not been much work on coupling the fluid and solid behaviour together.
- A few studies that have addressed the issue of coupling the fluid and solid have oversimplified the solid behaviour by not considering non-linear hardening behaviour and strain rate dependence of plasticity models.

# 4 CAVITATION EROSION FLUID STRUCTURE INTERACTION SOLVER IN 2D

## 4.1 Introduction

To initiate the development process, the solver is first developed in 2D. An SPH fluid solver SPHYSICS 2D [16] is used as a base to build up a cavitation solver. An SPH solid solver with elastic-plastic behavior is developed from scratch and then the two solvers are put together to have a fluid structure interaction cavitation solver. A description of the development can be found in the next section. To summarize, the various steps to developing a cavitation solver are the development of a fluid cavitation solver and its validation with 2D Rayleigh-Plesset bubble collapse, development of a solid solver with elastic-plastic response which is validated against FEM results and finally using the two solvers to develop a fluid structure interaction solver.

## 4.2 2D solver development

An existing fluid solver SPHYSICS\_2D [16] has been used as a base to develop further as a cavitation solver. The existing solver is modified to solve both fluid and solid behaviour as well as the two way coupling between the fluid and the solid.

### 4.2.1. Fluid Solver

The equations are modified such that the fluid and solid particles can be solved together, i.e. the solid particle takes part in the calculation for a fluid particle and vice-versa. Since the density difference across the fluid-solid interface is large the density equation is modified. For example, for a fluid particle  $a$  all neighbouring particles (whether solid or a fluid particle) are considered. The issue at the interface is the density difference between the fluid and the solid. Due to the nature of the density equation 2.9, the diffusion of density at the interface will occur if standard SPH form is used. However, in the present study a different form is used as given by equation 4.1, this reduces to the standard SPH form if particle  $a$  and  $b$  are the same material but makes sure no density diffusion occurs across the interface if  $a$  and  $b$  are different materials particles.

The density equation takes the form:

$$\rho_a = \sum_{b=1}^N m_b W_{ab} \times \frac{\rho_{a0}}{\rho_{b0}} \quad (4.1)$$

where  $\rho_{a0}$  and  $\rho_{b0}$  is the density of particle  $a$  and  $b$  respectively at the previous time step.

The momentum equation takes the following form:

$$\frac{dv_a^i}{dt} = \sum_b m_b \left( \frac{\sigma_a^{ij}}{\rho_a^2} + \frac{\sigma_b^{ij}}{\rho_b^2} - \Pi_{ab} \right) \frac{dW_{ab}}{dx_a^j} \quad (4.2)$$

Where

$$\sigma^{\alpha\beta} = -P \delta^{\alpha\beta} \quad (4.3)$$

The Tait equation of state has been used as in SPHYSICS\_2D [16]. The artificial viscosity term also remains the same as in SPHYSICS\_2D [16]. The real speed of sound of water,  $c_0 = 1480$  m/s has been used in the simulations. The actual sound speed is generally not used in typical SPH simulation as it results in a relative smaller time step. However, in cavitation simulations, the high speed micro jet has velocities high enough to allow for actual sound speed to be used in the simulation without any increase in the computational expense.

#### 4.2.2. Solid Solver

The density and momentum equation remain the same as equation (4.1) and (4.2). However, the definition of the stress tensor changes as compared to equation (4.3) (for a fluid). Since the constitutive equation is different for a solid the following relationship between stress and strain is used:

$$\begin{bmatrix} \sigma_{11} \\ \sigma_{22} \\ \sigma_{33} \\ \sigma_{23} \\ \sigma_{13} \\ \sigma_{12} \end{bmatrix} = \begin{bmatrix} 2\mu + \lambda & \lambda & \lambda & 0 & 0 & 0 \\ \lambda & 2\mu + \lambda & \lambda & 0 & 0 & 0 \\ \lambda & \lambda & 2\mu + \lambda & 0 & 0 & 0 \\ 0 & 0 & 0 & \mu & 0 & 0 \\ 0 & 0 & 0 & 0 & \mu & 0 \\ 0 & 0 & 0 & 0 & 0 & \mu \end{bmatrix} \begin{bmatrix} \varepsilon_{11} \\ \varepsilon_{22} \\ \varepsilon_{33} \\ 2\varepsilon_{23} \\ 2\varepsilon_{13} \\ 2\varepsilon_{12} \end{bmatrix} \quad (4.4)$$

The strain rate is calculated using a kinematic relation with the velocity, which is given as the following in SPH formulation:

$$\rho_a \dot{\varepsilon}_a^{ij} = \frac{1}{2} \sum_{b=1}^n m_b \left[ (v_b^i - v_a^i) \frac{\partial W_{ab}}{\partial x_a^j} + (v_b^j - v_a^j) \frac{\partial W_{ab}}{\partial x_a^i} \right] \quad (4.5)$$

The strain rate is integrated over time to give the strain and equation 4.4 is then used to obtain stress. The above set of equations then can be used in iterations to solve for an elastic response of a solid. However, plastic deformations are the main focus during a cavitation simulation. The following Yield criterion is then used to account for plasticity (for details refer to appendix B):

$$f = \min\left(\frac{\sigma_{vM}^2}{3J_2}, 1\right) \quad (4.6)$$

where  $J_2$  is:

$$J_2 = \frac{1}{6}[(\sigma_{11} - \sigma_{22})^2 + (\sigma_{22} - \sigma_{33})^2 + (\sigma_{33} - \sigma_{11})^2 + 6(\sigma_{23}^2 + \sigma_{31}^2 + \sigma_{12}^2)] \quad (4.7)$$

and  $\sigma_{vm}$  is the von Mises Yield stress.

As the value of parameter  $f$  falls below 1, the material starts to yield and the deviatoric stress tensor is multiplied by the same factor  $f$  which brings back the stress state to the Yield curve. Finally, a damage criterion is used where a damage parameter  $D_{DMG}$  is defined as follows:

$$D_{DMG} = \frac{\epsilon_p}{\epsilon_u} \quad (4.8)$$

Where  $\epsilon_p$  is the equivalent plastic strain in the material and  $\epsilon_u$  is the permissible equivalent plastic strain after which the material fails. As the damage parameter increases, the Young's modulus of the material decreases linearly with  $D_{DMG}$  and the material is completely damaged once  $D_{DMG}$  reaches unity.

### 4.2.3. Fluid structure interaction

Numerical simulation of the Fluid structure interaction remains a big challenge due to the presence of geometrical and material non-linearity. There are two different numerical approaches to solve such problems using SPH. One approach is to treat the fluid and solid as two computational domains which are solved separately with their respective governing equations. Interface boundary conditions must then be applied between the two phases in order to couple them. However, the approach poses difficulties since the fluid-solid interface is not known beforehand but rather it is dynamic in nature, which makes the two way coupling difficult.

Another approach is to consider the fluid and solid within a same mathematical framework, and to develop a single system for the entire domain. This is the approach adopted in the present

study, in order to develop a uniform SPH framework. The equations for both fluid and solid are written in the stress form such that interaction between fluid and solid can be considered within the kernel interaction itself.

For any FSI (fluid structure interaction) system the following Dirichlet and Neumann boundary conditions should follow at the fluid-solid interface:

- Dirichlet boundary condition across the interface which satisfies the velocity continuity at the interface, where the normal velocities across the interface should be equal:

$$v_f^\perp = v_s^\perp \quad (4.9)$$

- Neumann boundary condition across the interface which satisfies the stress continuity at the interface in the direction normal to the interface:

$$\sigma_f^{\alpha\beta} n_{fs}^\alpha = \sigma_s^{\alpha\beta} n_{fs}^\alpha \quad (4.10)$$

Where  $f$  and  $s$  represent the fluid and the solid respectively and  $n_{fs}$  is the normal to the interface.

The Dirichlet boundary condition is automatically satisfied with the above mentioned equation used for solving fluid and solid within the same framework. To transfer force across the interface while solving all the particles together, for any interaction between particles across the interface, the total force on one particle due to the other (particle  $a$  and  $b$ ) can be resolved in the x-y direction, while considering there is no interface but a continuum across the interface (where  $\hat{i}$  and  $\hat{j}$  are unit vectors in x and y directions respectively).

$$\vec{F}_{ab} = F_x \hat{i} + F_y \hat{j} \quad (4.11)$$

However, since there exists a discontinuity at the interface and in the absence of viscous forces, the force parallel to the interface should be zero. Hence the force vector is multiplied by the vector normal to the interface to obtain the final force on the particle.

$$\vec{F}_{ab}^{Interface} = F_x n_x \hat{i} + F_y n_y \hat{j} \quad (4.12)$$

The above equation along with the momentum equation is enough to satisfy the Neumann boundary condition to transfer the forces across the interface.

### 4.3 Results and validation

While developing the new SPH cavitation solver, it is vital to validate the solutions with an existing solver or experimental result. Moreover, a convergence study is also performed to determine the right inter-particle distance to capture the physics accurately.

#### 4.3.1. Bubble collapse

The fluid cavitation solver is used to simulate the collapse of a single cavitation bubble. The formation of micro jet during a bubble collapse leads to a shock wave that results in a pressure loading on the solid surface. The accurate prediction of the micro jet velocity will make sure the shock wave and the pressure acting on the solid surface are accurately predicted.

The number of particles in the micro jet and hence the inter-particle distance could play an important role in determining the velocity of the micro jet. If the inter-particle distance is too large, there would be very few particles present in the micro jet, which could lead to an inaccurate prediction of the jet velocity. On the other hand, a very small inter-particle distance could lead to excessively large number of particles in the micro jet, leading to unnecessary increase in computational time. Hence determining the right inter-particle distance becomes important for such a simulation.

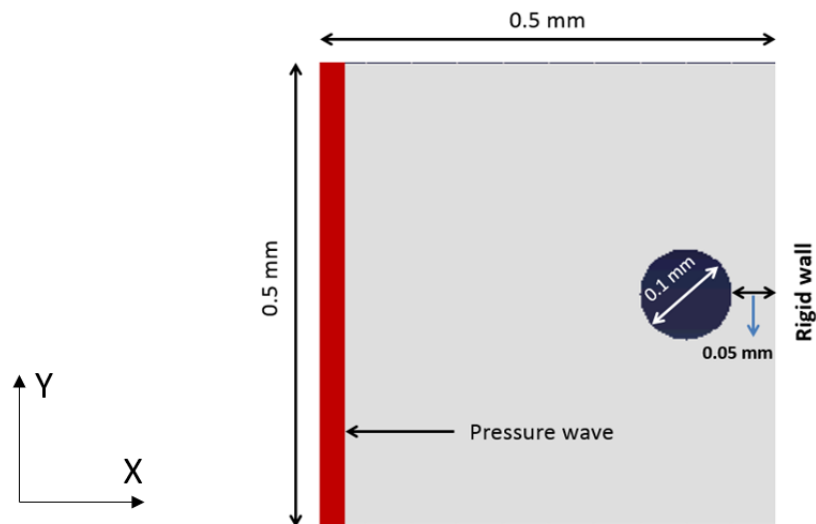
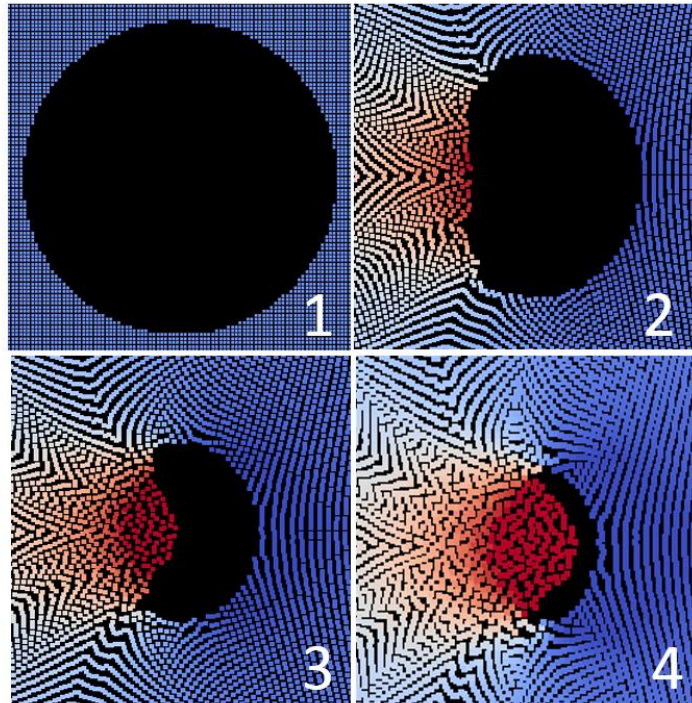


Fig 4.1. Computational domain for a cavitation bubble collapse in SPH.

The domain shown in fig 4.1 is used for SPH single bubble collapse simulation. A vacuum bubble (i.e. neither gas or vapor inside) of 100  $\mu\text{m}$  diameter is placed close to the wall with the wall at a distance of 50  $\mu\text{m}$  from the bubble surface. The right wall is a repulsive boundary which acts as a rigid wall, the top and bottom are walls with wave absorbers to avoid reflection of pressure waves from the wall. On the left is a wave maker (a set of repulsive particles) which

is moved to create a pressure wave (repulsive boundary condition have been discussed in section 2.3.10.2). As the pressure wave hits the bubble, the bubble starts to collapse with a micro jet towards the wall as shown in the sequence of images in fig 4.2.



*Fig 4.2. Sequence of images from various stages of a bubble collapse from the SPH simulation. Image 1 shows a full bubble and the subsequent images show the collapse after the pressure wave hits the bubble.*

To establish the convergence wrt inter-particle spacing, five different inter-particle distances were considered and the micro jet velocity just before hitting the other side of the bubble was recorded for comparison. Table 4.1 gives the value of micro jet velocity wrt inter-particle distance. The micro jet velocity seems to be more or less constant after  $dx=2.5 \mu\text{m}$ . An intuitive argument would suggest that the number of particles along the circumference of the bubble is an important criterion to maintain an accurate jet velocity. Hence we define a parameter which is the bubble radius divided by the inter-particle distance when convergence is reached ( $dx=2.5 \mu\text{m}$ ) and this has to be kept constant to maintain an accurate jet velocity. For example, if in this case with a bubble diameter of  $100 \mu\text{m}$  the inter-particle distance of  $dx=2.5 \mu\text{m}$  can give an accurate solution, then a bubble twice the size can be resolved accurately with twice the inter-particle distance.

Table 4.1. Convergence study of inter-particle distance for a cavitation bubble collapse.

dx ( $\mu\text{m}$ )	10	5	3.5	2.5	1.5
Micro jet velocity (m/s)	560	960	864	879	883

To be sure that the time-step does not affect the solution in any way, a time convergence study was carried out. Table 4.2 shows the micro jet velocity for  $dx=2.5 \mu\text{m}$  (determined from the inter-particle convergence study) and different CFL number. It could be seen that the CFL number up to 0.2 leads to a converged prediction, higher CFL numbers could also be used since the error between CFL=0.1 and CFL=0.5 is around 1%.

$$\Delta t = CFL * \min(\Delta t_1, \Delta t_2) \quad (4.13)$$

$$\Delta t_1 = \min_a (\sqrt{h/|f_a|}) \quad \Delta t_2 = \min_a \left( \frac{h}{c_a + \max \left| \frac{h \vec{v}_{ab} \cdot \vec{r}_{ab}}{\vec{r}_{ab}} \right|} \right) \quad (4.14)$$

where  $h$  is the smoothing length,  $|f_a|$  is the force per unit mass on a particle,  $c_a$  is the speed of sound for particle  $a$ ,  $\vec{v}_{ab}$  is the relative velocity of particle  $a$  &  $b$  and  $\vec{r}_{ab}$  distance between particle  $a$  and  $b$ .

Table 4.2. Convergence study wrt time for a cavitation bubble collapse.

CFL number	0.1	0.2	0.3	0.4	0.5
Micro jet velocity (m/s)	880.8	879.3	872.8	867.7	869.6

### 4.3.2. Solid solver

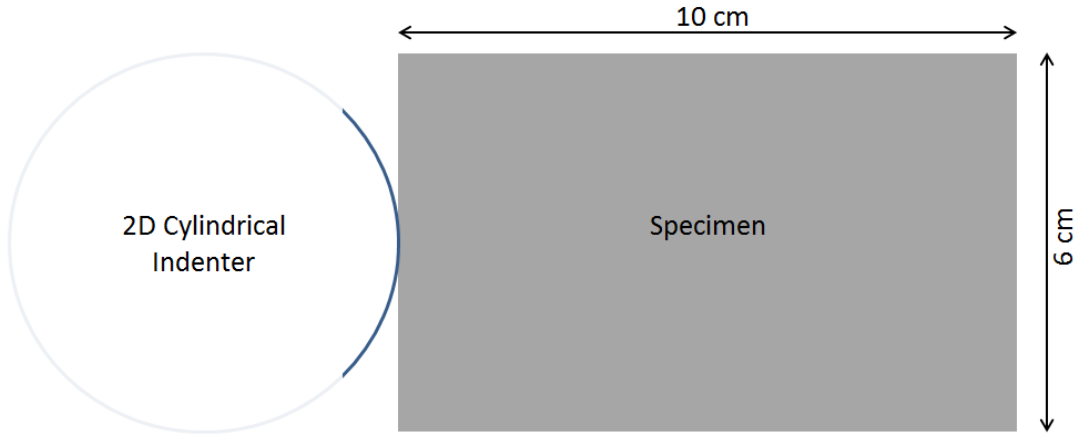


Fig 4.3 Computational domain for a 2D SPH indentation simulation with the indenter on the left and stainless steel specimen on the right (shaded in grey).

The solid solver can also be used without the fluid solver by considering an indenter to indent the material in order to estimate the plastic deformation. In the present study we do a similar simulation. As shown in fig 4.3, a 2D cylindrical indenter is used to indent a stainless steel specimen (A-2205) shaded in grey on the right. The material properties are as follows: Young's Modulus  $E=186$  GPa, Poisson's ratio  $\nu=0.3$  and the yield curve given by

$$\sigma_y(\epsilon_p) = [A_0 + B_0(\epsilon_p)^n] \quad (4.15)$$

where  $A_0= 508$  MPa,  $B_0 = 832$  MPa,  $n = 0.29$ .

To validate our SPH solid solver, we use results from FEM solver Cast3m [79]. A similar case is setup in Cast3m and the same indentation depth is given in both solvers. The right end of the domain is set as a rigid wall in both the simulations. The top and bottom end of the domain are open boundaries which are free to move. The quasi-static FEM calculation uses 4876 8 node cells, with minimum mesh size set to 0.5 mm. The SPH calculation uses 24000 particles with a constant mesh size set to 0.5 mm. Fig 4.4 shows contours from SPH and FEM solver for the shear component of stress. To compare the results quantitatively we plot all the stress components along the black vertical line (the line is at 10% of the indenter diameter inside the material surface) in the SPH contour in fig 4.5. The SPH results show a good agreement with FEM results with average error less than 5%.

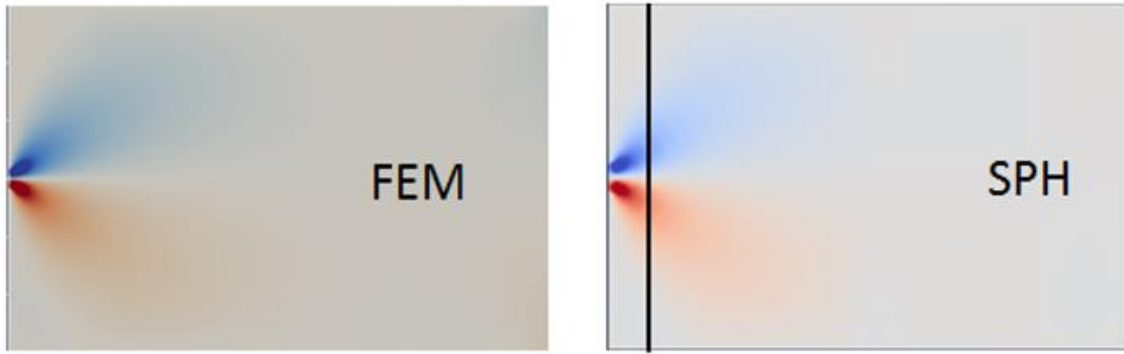


Fig 4.4. Shear stress contours for FEM and SPH (the black line in SPH contour is at 10% of the indenter diameter inside the material surface).

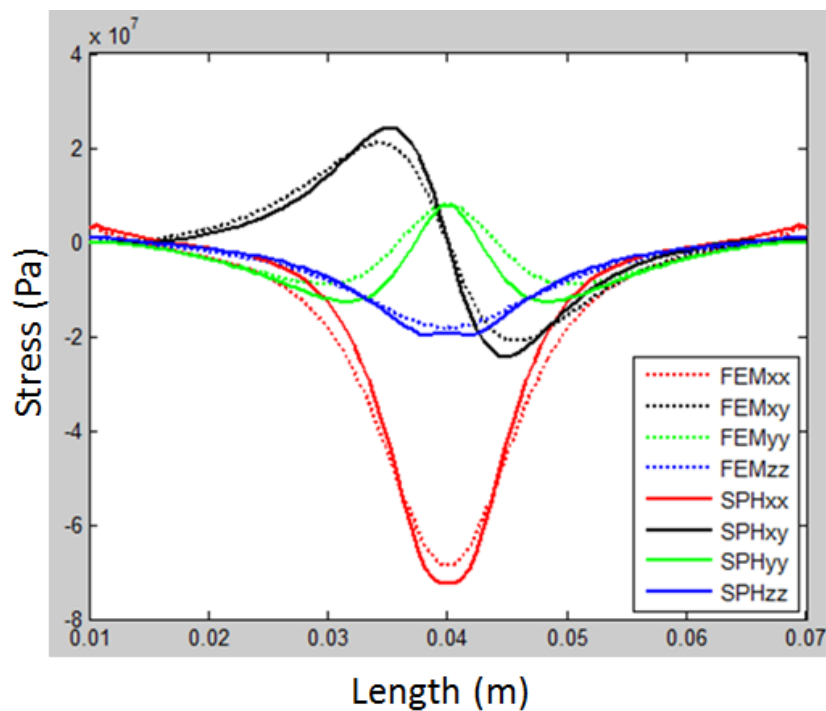


Fig 4.5. Comparison of all stress component FEM vs SPH (over the black line in SPH contour in fig 4.4).

Finally, a fluid structure interaction simulation is carried out and a sequence of images from the simulation is shown in fig 4.6. The collapsing bubble near a solid surface produces a shock wave which leads to plastic strain in the material. A total of 128000 particles were used for this simulation, the initial domain is shown in fig 4.6a where a bubble of 1 mm is placed in the fluid close to the wall. The distance between the bubble center and the interface is 1.5 mm. A pressure wave is initiated from the left boundary to initiate the collapse. The top, bottom and right boundaries are set as rigid walls. The fluid and material parameters for the present simulation are listed in table 4.3:

Table 4.3 Material parameters for the FSI simulation

Parameter	Fluid (Water)	Solid (A-2205)
Density (kg/m <sup>3</sup> )	1000	7800
Sound speed (m/s)	1500	4883.33
Young's Modulus	-	186 GPa
Poisson ratio	-	0.3
A <sub>0</sub> (in equation 4.15)	-	508 MPa
B <sub>0</sub> (in equation 4.15)	-	832 MPa
N (in equation 4.15)	-	0.29

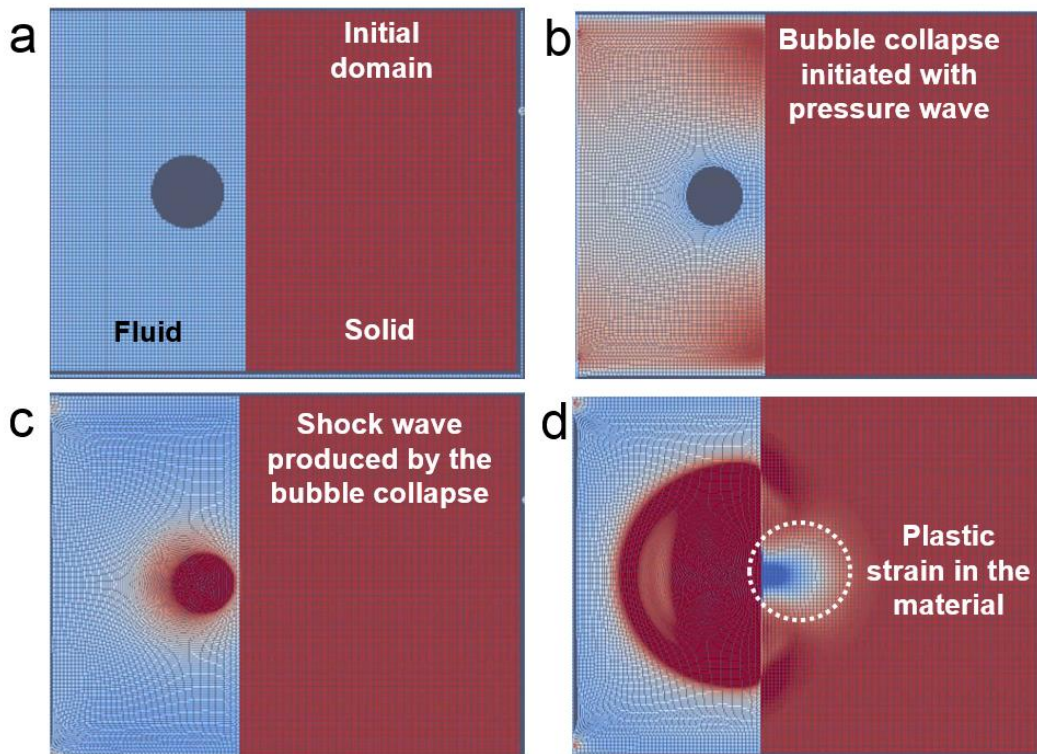
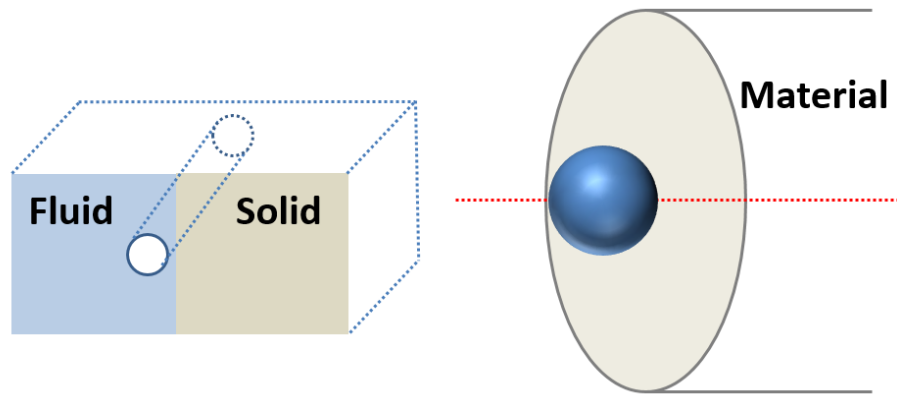


Figure 4.6. Image sequence for FSI simulation of bubble collapse near a solid, contours of pressure in fluid and plastic strain in solid.

However, a 2D solver can only be used to understand trends and behaviors at large. Calculating mass loss curves and predicting mass loss from a 2D solver does not represent the actual cavitation problem. Figure 4.7 shows why a 2D solver doesn't exactly represent cavitation

since a 2D bubble represents an infinitely long cylindrical cavity and not a spherical bubble. Moreover, the 2D plane strain analysis used for solid in the present study cannot reproduce the actual stress in 3D. To calculate mass loss and predict damage, we developed a 2D axisymmetric solver on the same lines as the 2D solver. The next section explains the development, validation and results.

Considering a case of a single cavitation bubble collapse or multiple bubble collapse at the same point in space, an axisymmetric solver could be used to calculate mass loss curves for different materials and predict material erosion. To develop a 2D axisymmetric solver, the 2D fluid structure interaction cavitation solver is used as a base where modifications are made in terms of changing SPH equations to cylindrical coordinates, creating symmetry at the axis and applying a density correction which eventually leads to changes in momentum equation for particles close to the axis. Such a correction has been derived in the literature for a fluid but was not available for the solid. Thus, a novel SPH scheme was implemented by deriving new momentum equations for a similar density correction for the solid. A fluid axisymmetric solver capable of solving bubble collapse and a solid axisymmetric solver capable of solving elastic-plastic damage and material loss was developed in 2D axisymmetric and is presented in chapter 5 & 6.



*Figure 4.7. Left schematic shows what a 2D plane-strain bubble collapse physically represent, the right schematic shows that an axisymmetric simulation can solve cavitation for a single bubble.*

## **Chapter Highlights**

- A convergence study is carried out for the 2D fluid SPH cavitation bubble collapse.
- The 2D solid SPH solver is validated against a FEM solver.
- The two solvers are put together to run a fluid structure interaction simulation in 2D.
- The inability of the 2D solver to represent the actual spherical cavity and thus the actual phenomenon leads to the development of a 2D axisymmetric FSI SPH solver which is presented in Chapter 5 & 6.

# 5 CAVITATION SOLID SOLVER IN 2D AXISYMMETRIC

This chapter is constructed from a paper which has been submitted to the Computer Methods in Applied Mechanics and Engineering. The paper has been used as it is in this chapter, hence there could be a repetition of text, figures or tables previously introduced in chapters 1-3. In order to help the reader, some sections already presented are identified in the text so that the reader could skip these parts.

## **An axisymmetric Solid SPH solver with consistent treatment of particles close to the symmetry axis: Application to cavitation erosion**

Shrey Joshi<sup>1,2</sup>, Jean Pierre Franc<sup>2</sup>, Giovanni Ghigliotti<sup>2</sup>, Marc Fivel<sup>1</sup>

<sup>1</sup>*Univ. Grenoble Alpes, CNRS, Grenoble INP, SIMaP, 38000 Grenoble, France*

<sup>2</sup>*Univ. Grenoble Alpes, CNRS, Grenoble INP, LEGI, 38000 Grenoble, France*

### **Abstract**

A meshless Smoothed Particle Hydrodynamics solid solver is developed in order to study fluid structure interactions and to predict cavitation erosion. The solid solver is developed in-house in an axisymmetric configuration. The existing SPH methods dedicated to solid materials do not allow a consistent treatment of particles close to the symmetry axis, so a density correction scheme is proposed here to derive new density and momentum equations for solid mechanics in axisymmetric SPH formulation. The new SPH equations are coded in the solver and the SPH solid solver is then validated against FEM results which shows excellent agreement.

**Keywords:** Smoothed Particle Hydrodynamics, plasticity, cavitation, material damage, axisymmetric

## 5.1 Introduction (skip if you read section 1.3 and 3.1)

Cavitation erosion is a major issue amongst a wide range of equipments such as hydraulic devices, diesel injectors, artificial heart valves, etc... Cavitation is defined as the appearance of vapor cavities inside a continuous and homogeneous liquid medium. The generation of vapor cavities could happen due to various reasons, but the cause is mostly associated to the drop of local pressure below the vapor pressure. Figure 5.1 shows a pressure-temperature phase diagram of water, showing that a drop of pressure below the vapor pressure leads to vaporization of liquid. This behavior is commonly known as cavitation.

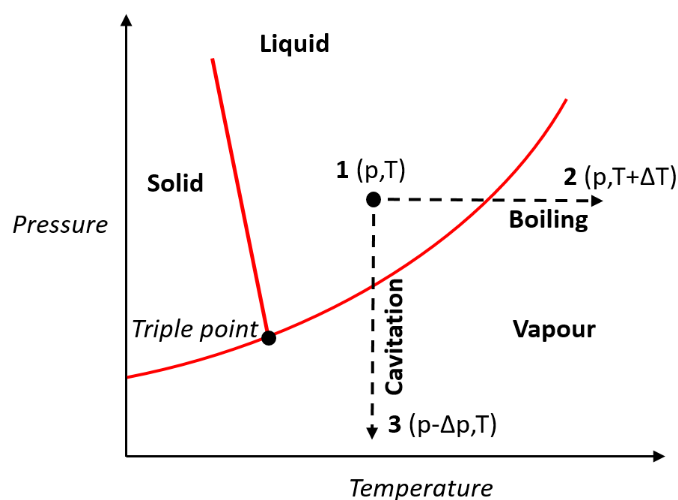
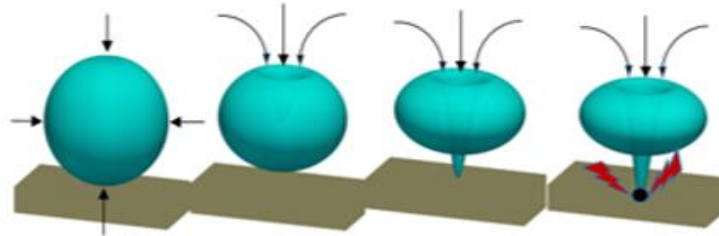


Figure 5.1. Pressure-temperature phase diagram for water showing the two forms of vaporization in water, namely, boiling (state 1 to state 2) and cavitation (state 1 to state 3).

During cavitation the continuum liquid medium breaks down to form vapor cavities. These vapor bubbles can collapse when the ambient pressure increases above the vapor pressure. The collapse of these bubbles can be very different depending on the position of the bubbles w.r.t. to a solid surface. When the bubble collapse is located near the surface, it can lead to the formation of a high velocity micro jet and subsequent shock wave. Such an asymmetry in the collapse dynamics is due to a weaker fluid flow on the wall side. Figure 5.2 shows a schematic description of a collapsing bubble and the resulting micro jet.

During the bubble collapse, the solid surface experiences a high pressure due to the shock wave and the high velocity micro jet hitting the surface. The magnitude of the pressure acting on the surface could be high enough to cause plastic damage to the material. Although the experimental measurement of these pressures acting on the surface still remains a challenge, various studies have estimated it to be around a few GPa [1-5]. Moreover, experimental

investigations offer only limited information about bubble collapses and the subsequent formation of micro jets and pressure waves since any intrusive measurement can cause deviations. Such difficulties in experimental investigations have led to the use of numerical studies to understand and analyze cavitation.



*Figure 5.2. Collapse of a single cavitation bubble near a surface.*

A vast majority of numerical studies have focused on solving the dynamics of the cavitation bubble collapse in the fluid. However, more work need to be done in order to get a thorough understanding of material damage induced by collapsing bubbles. For instance, most numerical CFD studies estimate cavitation erosion-prone areas using either peak pressures or Cavitation Aggressiveness Index (CAI) [8-10], however it is still debatable as to whether peak pressure or CAI can accurately characterize the cavitation erosion process taking place in the material. Moreover, these methods can only predict cavitation prone areas and cannot predict the actual pit sizes and the magnitude of material erosion. Typically, the deformation of the solid surface due to cavitation can change the load distribution and load intensity on the surface. In other words, any CFD calculation performed under the assumptions that the solid wall is infinitely rigid will automatically overestimate the load applied on the material. Hence to address the above issues better, recently there has been a thrust towards modelling cavitation erosion using fluid structure interaction solvers to understand the phenomenon of cavitation erosion in entirety [11-13]. A thorough numerical study of cavitation that can provide a holistic understanding, ideally requires a two-way fluid structure interaction coupling to get realistic results for cavitation erosion. A comprehensive cavitation numerical model should ideally include the following elements in the solver:

- A fluid model capable of capturing the dynamics of a collapsing bubble including the details about the micro jet and the shock waves. The fluid model should account for a deformable boundary.
- A solid model aiming at solving for the material response due to the pressure acting on the material surface as a result of the micro jet and the shock waves. The solver must take

into account the elasto-plastic behavior of the material as well as the development of damage. Since cavitation is a relatively fast process, strain rate dependent hardening behavior should be included in the model.

- A fluid structure interaction scheme: during a cavitation bubble collapse, high intensity shock waves are produced along with micro jet. The shock wave travels through the fluid to the solid, a part of the wave is reflected back into the liquid and the rest gets transmitted to the solid [14]. In the case of two elastic media, both the energy transfer and the solid-liquid interface velocity depend on the ratio of acoustic impedances of the liquid and solid. A two-way coupling is required to model this behavior properly.

The problem is quite complex since the fluid solver (typically a Eulerian Finite Volume Method (FVM) code) and the solid solver (typically a Lagrangian Finite Element Method (FEM) code) are generally two different codes which then need to be coupled in order to communicate data. Moreover, the elasto-plastic deformation of the solid medium due to cavitation loads implies the fluid mesh has to be re-constructed to match the solid mesh and maintain the continuity at the interface. Conventionally, ALE (Arbitrary Lagrangian Eulerian) methods have been used to simulate such a problem [15]. To overcome the above complexity, in the present study a first attempt has been made to solve cavitation erosion using a meshless particle method, namely the Smoothed Particle Hydrodynamics (SPH), to model both the fluid and the solid behavior in a unique Lagrangian framework. The method offers the following advantages:

- Both fluid and solid response can be captured using the same solver and the same numerical method i.e. SPH. Both the solid and the fluid can be coded and solved within a single code making it much easier from the development perspective.
- Coupling a FVM solver to a FEM solver can be quite complicated and requires dedicated procedures for data transfer across the two codes. The problem is eliminated here since the solver uses SPH for both solid and fluid in a common code; no such coupling is required; the data are easily exchanged within the RAM memory. For each particle, one only needs to specify if it is a fluid or a solid particle.
- The tricky mesh reconstruction for the fluid domain is eliminated when using meshless methods like SPH where both the fluid and the solid are solved using a Lagrangian formulation and hence such deformation are already taken care of via particle movement.

## 5.2 SPH solver

To develop the SPH FSI solver, the existing 2D open source fluid SPH code SPHYSICS is used as a basis to develop the solver further [16]. However, a 2D FSI solver for a collapsing bubble over a solid medium does not represent a spherical cavity but rather an infinitely long cylindrical cavity which is a misrepresentation of the geometry. Also the response of a 2D solid medium is quantitatively different from that in the actual case. To make sure the cavitation bubbles and the solid medium are represented as in reality, the 2D solver is modified to 2D axisymmetric. However, axisymmetric SPH solver suffer from an inconsistent definition of density near the symmetry axis. This paper presents a new method to mathematically resolve this issue inspired by an approach used in fluid axisymmetric SPH simulation. New density and momentum equations are derived for solid axisymmetric SPH solver which can treat particles to obtain accurate density field close to the axis, the solver is finally validated against FEM results.

### 5.2.1. SPH fundamentals (skip if you read section 2.2)

Smoothed Particle Hydrodynamics (SPH) is a meshless numerical method to solve partial differential equations by discretizing the computational domain using set of particles. It was first introduced by Lucy [17] in 1977 for astrophysics calculations and later by Monaghan [20] for fluid flows. The method is based around interpolation to express a function at any point in space using its values at a set of disordered neighboring points called the particles by using a kernel function.

The integral interpolant of any function  $A$  at a position  $\mathbf{r}$  is defined by the integration over the entire domain ( $\Omega$ ):

$$A(\vec{r}) = \int_{\Omega} A(\vec{r}') \mathcal{W}(\vec{r} - \vec{r}', h) d\vec{r}' \quad (5.1)$$

where  $\mathcal{W}$  is the kernel function and  $h$  an associated length. The kernel function ( $\mathcal{W}$ ) is used for interpolation and must verify the following properties: firstly, the integration of the kernel function over the whole domain should lead to unity as given by equation 5.2 and secondly, as the limit of  $h$  (commonly known as smoothing length) tends to zero the kernel function becomes a Dirac-Delta function as given by equation 5.3.

$$\int \mathcal{W}(\vec{r} - \vec{r}', h) d\vec{r}' = 1 \quad (5.2)$$

and

$$\lim_{h \rightarrow 0} W(\vec{r} - \vec{r}', h) = \delta(\vec{r} - \vec{r}') \quad (5.3)$$

Several formulations have been proposed for the Kernel function. In the present paper we chose to use a cubic spline function as detailed in appendix.

In order to use equation 5.1 for numerical purpose, the equation is transformed into a discretized form where it takes the form of a summation interpolant given by,

$$A(\vec{r}) \approx \sum_{j=1}^N A(\vec{r}_j) W(\vec{r} - \vec{r}_j, h) \frac{m_j}{\rho_j} \quad (5.4)$$

where the summation index  $j$  denotes a particle label, and the summation is performed over all the particles. Particle  $j$  has mass  $m_j$ , position  $\vec{r}_j$  and density  $\rho_j$ . The value of any quantity  $A$  at  $\vec{r}_j$  is denoted by  $A(\vec{r}_j)$ .

The key element is that we can write a differentiable interpolant of a function from its values at the particles by using a kernel which is differentiable. Derivatives of this kernel can be obtained by ordinary differentiation; there is no need to use finite differences or any other numerical method. For instance, if we want to compute the Laplacian  $\Delta A$ , we can use

$$\Delta A(\vec{r}) \approx \sum_{j=1}^N A(\vec{r}_j) \Delta W(\vec{r} - \vec{r}_j, h) \frac{m_j}{\rho_j} \quad (5.5)$$

### 5.2.2. 2D SPH formulation for Solid mechanics

The continuity and the momentum equations are formulated in SPH form by transforming the equations into a summation over a set of discrete particles, interpolated using the kernel function. The density equation takes the form

$$\rho_a = \sum_b m_b W_{ab} \quad (5.6)$$

where  $\rho_a$  is the density of particle  $a$ ,  $b$  is the index for neighboring particles,  $m_b$  is the mass and  $W_{ab}$  is the value of kernel function centered at particle  $a$  and estimated at the neighboring particle,  $b$ . Within the framework of isotropic linear elasticity, the stress state at a given time step for a given particle is calculated from the constitutive equation,

$$\sigma_{ij} = 2\mu \varepsilon_{ij} + \lambda \delta_{ij} \varepsilon_{kk} \quad (5.7)$$

where  $\boldsymbol{\sigma}$  is the stress tensor,  $\boldsymbol{\varepsilon}$  is the strain tensor,  $\lambda$  and  $\mu$  the Lamé elastic constants.

Once density and stress are calculated from the above equations, the values are used in the SPH form of the momentum equation given below,

$$\frac{dv_a^i}{dt} = \sum_b m_b \left( \frac{\sigma_a^{ij}}{\rho_a^2} + \frac{\sigma_b^{ij}}{\rho_b^2} - \Pi_{ab} \right) \frac{dW_{ab}}{dx_a^j} \quad (5.8)$$

where  $\Pi$  is the artificial viscosity term and the strain is compute using the particle velocities by the following

$$\rho_a \dot{\varepsilon}_a^{ij} = \frac{1}{2} \sum_{b=1}^n m_b \left[ (v_b^i - v_a^i) \frac{dW_{ab}}{dx_a^j} + (v_b^j - v_a^j) \frac{dW_{ab}}{dx_a^i} \right] \quad (5.9)$$

where  $\dot{\varepsilon}_a$  is the time derivative of strain for particle  $a$ ,  $v_a^i$  is the velocity in x direction for particle  $a$ .

For modelling strain-rate dependent plasticity, we use the phenomenological Johnson-Cook model [19] relating the yield stress ( $\sigma_y$ ) to the plastic deformation  $\varepsilon_p$  and the plastic strain rate

$\dot{\varepsilon}_p$ :

$$\sigma_y(\varepsilon_p, \dot{\varepsilon}_p, T) = [A_0 + B_0(\varepsilon_p)^n][1 + C_0 \ln(\dot{\varepsilon}_p^*)][1 - (T^*)^m] \quad (5.10)$$

where  $T^* = \frac{(T - T_0)}{(T_m - T_0)}$  is the non-dimensional effective temperature and  $\dot{\varepsilon}_p^* = \frac{\dot{\varepsilon}_p}{\dot{\varepsilon}_{p0}}$  the non-

dimensional effective plastic strain rate. In this paper, the temperature effects are neglected and equation (5.10) reduces to,

$$\sigma_y(\varepsilon_p, \dot{\varepsilon}_p, T) = [A_0 + B_0(\varepsilon_p)^n][1 + C_0 \ln(\dot{\varepsilon}_p^*)] \quad (5.11)$$

In the Johnson-Cook model,  $A_0$ ,  $B_0$ ,  $C_0$ ,  $n$  and  $m$  are material constants. Also  $\dot{\varepsilon}_{p0}$  is the reference plastic strain-rate of the quasi-static test used to determine the yield and hardening parameters  $A_0$ ,  $B_0$  and  $n$ .  $T_0$  is a reference temperature, and  $T_m$  is the reference melting temperature. For conditions where  $T^* < 0$ , we assume that  $m = 1$ .

Details regarding plasticity calculation and return mapping algorithm for non-linear isotropic hardening is provided in Appendix B.

### 5.2.3. Moving the particles (skip if you read section 2.3.7)

The particles are moved using XSPH variant [21]

$$\frac{d\vec{r}_a}{dt} = \vec{v}_a + \varepsilon_{coef} \sum \frac{m_b}{\bar{\rho}_{ab}} \vec{v}_{ba} W_{ab} \quad (5.12)$$

where  $\varepsilon_{coef} = 0.5$  and  $\bar{\rho}_{ab} = (\rho_a + \rho_b)/2$ . The method moves the particle with a velocity close to the neighborhood and helps in avoiding inter-penetration of particles.

#### 5.2.4. Time integration (skip if you read section 2.3.6)

Consider the momentum equation (equation 5.13) and position equation (equation 5.14) in the following form

$$\frac{d\vec{v}_a}{dt} = \vec{F}_a \quad (5.13)$$

$$\frac{d\vec{r}_a}{dt} = \vec{v}_a \quad (5.14)$$

where  $F_a$  represents the force and  $\vec{v}_a$  represents the velocity contribution from particle  $a$  and from neighboring particles (XSPH correction).

The predictor step uses the time derivatives from the last time step to predict velocities and position at half-time step

$$\vec{v}_a^{n+1/2} = \vec{v}_a^n + \frac{\Delta t}{2} \vec{F}_a^n \quad (5.15)$$

$$\vec{r}_a^{n+1/2} = \vec{r}_a^n + \frac{\Delta t}{2} \vec{v}_a^n \quad (5.16)$$

These values are then corrected using derivatives estimated at the half step

$$\vec{v}_a^{n+1/2} = \vec{v}_a^n + \frac{\Delta t}{2} \vec{F}_a^{n+1/2} \quad (5.17)$$

$$\vec{r}_a^{n+1/2} = \vec{r}_a^n + \frac{\Delta t}{2} \vec{v}_a^{n+1/2} \quad (5.18)$$

Finally using the values of velocity and position from the predictor and corrector step one can obtain the values at the end of the time step by,

$$\vec{v}_a^{n+1} = 2\vec{v}_a^{n+1/2} - \vec{v}_a^n \quad (5.19)$$

$$\vec{r}_a^{n+1} = 2\vec{r}_a^{n+1/2} - \vec{r}_a^n \quad (5.20)$$

### 5.2.5. Artificial viscosity

The artificial viscosity term to be used in equation 5.8 is given by:

$$\Pi_{ab} = \begin{cases} \frac{-\alpha \bar{c}_{ab} \mu_{ab}}{\bar{\rho}_{ab}} & \vec{v}_{ab} \cdot \vec{r}_{ab} < 0 \\ 0 & \vec{v}_{ab} \cdot \vec{r}_{ab} > 0 \end{cases} \quad (5.19)$$

$$\mu_{ab} = \frac{h \vec{v}_{ab} \cdot \vec{r}_{ab}}{\vec{r}_{ab}^2 + \eta^2} \quad (5.22)$$

where  $\alpha$  ( $=1$ ) is a constant,  $h$  is the smoothing length,  $\vec{v}_{ab}$  is the relative velocity of particle  $a$  &  $b$ ,  $\bar{c}_{ab}$  is the average sound speed for particle  $a$  and  $b$ ,  $\vec{r}_{ab}$  is the position vector from particle  $a$  to  $b$  and  $\eta$  is set to  $10^{-8}$ , this is to avoid the denominator of eq 5.22 from going to zero if the interparticle distance  $\vec{r}_{ab}$  goes to zero. Additional information regarding the equations 5.21 and 5.22 can be found in the work by Monaghan [20].

## 5.3 Axisymmetric SPH for Solid Mechanics

### 5.3.1. Methodology

The original solver SPHYSICS only solves for fluid in 2D. Thus, a solid solver is added to the original fluid SPHYSICS in 2D plane strain. However, in that case, a 2D bubble represents a 3D infinitely long cylindrical bubble which is far from reality. Also a 2D plane-strain solid simulation is physically very different from the reality (in 3D) even for a similar cavitation load. To overcome this and not increase the simulation time significantly we chose to convert the 2D solver to an axisymmetric solver so that the spherical shape of the bubble is preserved. We present a detailed methodology which can be adopted to change 2D SPH solid solver to axisymmetric. Broadly the following changes are required to change the solver to axisymmetric:

1. Changing formulations and equations to cylindrical coordinate system
2. Adding a symmetry axis to the solver
3. Density corrections for particles close to the symmetry axis

An elegant approach to the axisymmetric Euler fluid equations was proposed by Brookshaw [80] who derived the SPH form of these basic equations using the minimal action principle (see work by Monaghan [81] and references thereafter for the history of variational SPH). A similar

approach is used in the present work and the following changes are made to convert the 2D Solid SPH solver to an axisymmetric Solid SPH solver (this can also be used as a guide to develop an axisymmetric solver from any commonly available 2D open source SPH solvers): the density in axisymmetric formulation can be classified as the 3D density (which is the actual material density) and a 2D effective density which is used in the axisymmetric calculations. The 2D effective density is given by,

$$\eta_a = \sum_{b=1}^N m_b W_{ab} \quad (5.20)$$

where the 2D density is defined as  $\eta_a = 2\pi|r_a|\rho_a$  which of course is different from the 3D density  $\rho_a$ . To achieve this the mass of particle is allocated according to the following equation,

$$m_a = 2\pi|r_a|\rho_a drdz \quad (5.24)$$

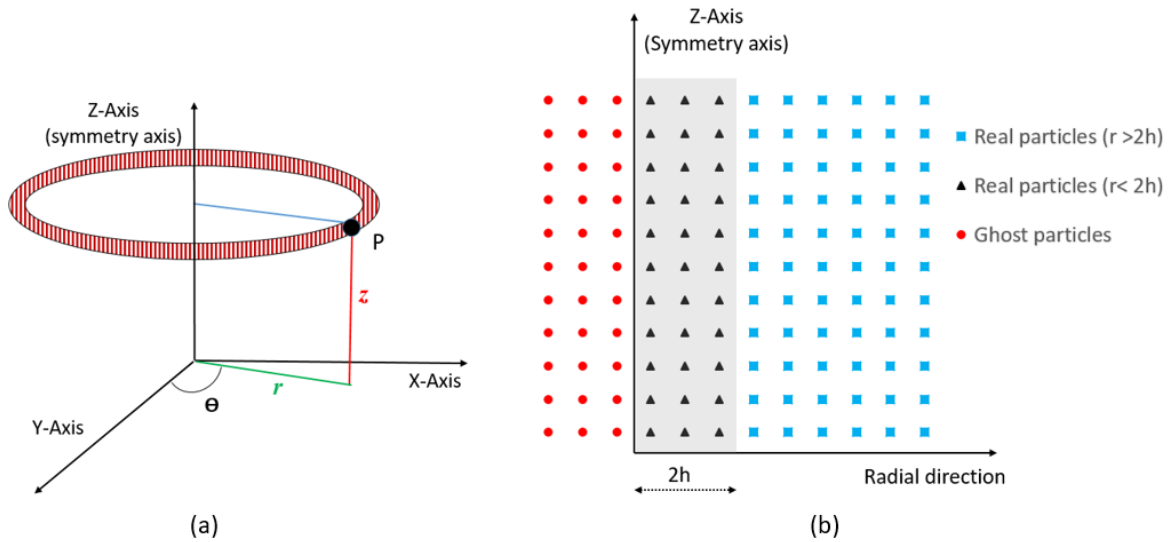


Figure 5.3(a) Sketch of the coordinate system and notation used to describe axisymmetric formulation, (b) shows a schematic of how particles are placed in an axisymmetric system where real particles on right of the symmetry axis at a distance less than  $2h$  from the axis are mirror imaged across to the axis as ghost particles.

The z-axis is defined as the symmetry axis. As shown in Figure 5.3b particles at a distance of  $2h$  or less from the axis are mirror imaged across the z-axis to create ghost boundary particles. For any particle  $i$  with coordinate  $(r, z)$ , velocity  $(\dot{r}, \dot{z})$ , mass  $m_i$ , density  $\rho_i$  and stress  $(\sigma^{rr}, \sigma^{zz}, \sigma^{\theta\theta}, \sigma^{rz})$ , the corresponding ghost particle  $k$  has position  $(-r, z)$ , velocity  $(-\dot{r}, \dot{z})$ , mass

$m_k$ , density  $\rho_k$  and stress  $(\sigma^{rr}, \sigma^{zz}, \sigma^{\theta\theta}, -\sigma^{rz})$ . Thus position, velocity as well as other quantities such as density and stress for ghost particles are updated at each step not using the SPH equations but from the evolution of real particles not the ghost ones. Even though the use of ghost particles is not strictly necessary in axisymmetric geometry, it is possible to use a line of reflective particle at the symmetry axis without using ghost particle. However, it is recommended to use ghost particles to correctly represent the density and its derivatives near the singularity axis.

The equations of motion in cylindrical coordinate system are given by,

$$\frac{dv^r}{dt} = \frac{1}{\rho} \left( \frac{\partial \sigma^{rr}}{\partial r} + \frac{\sigma^{rr}}{r} \right) + \frac{1}{\rho} \frac{\partial \sigma^{rz}}{\partial z} - \frac{1}{\rho} \frac{\sigma^{\theta\theta}}{r} + b^r \quad (5.25)$$

$$\frac{dv^z}{dt} = \frac{1}{\rho} \left( \frac{\partial \sigma^{zz}}{\partial z} + \frac{\sigma^{rz}}{r} + \frac{\partial \sigma^{rz}}{\partial r} \right) + b^z \quad (5.26)$$

where  $\mathbf{b}$  is the body force vector.

The SPH form of the above equations of motion in cylindrical form are given by the following [82],

$$\frac{dv_a^r}{dt} = 2\pi \sum_b m_b \left( \frac{\sigma_b^{rr} r_b}{\eta_b^2} + \frac{\sigma_a^{rr} r_a}{\eta_a^2} \right) \frac{dW_{ab}}{dr_a} + 2\pi \sum_b m_b \left( \frac{\sigma_b^{rz} r_b}{\eta_b^2} + \frac{\sigma_a^{rz} r_a}{\eta_a^2} \right) \frac{dW_{ab}}{dz_a} - 2\pi \frac{\sigma_a^{\theta\theta}}{\eta_a} \quad (5.27)$$

$$\frac{dv_a^z}{dt} = 2\pi \sum_b m_b \left( \frac{\sigma_b^{rz} r_b}{\eta_b^2} + \frac{\sigma_a^{rz} r_a}{\eta_a^2} \right) \frac{dW_{ab}}{dr_a} + 2\pi \sum_b m_b \left( \frac{\sigma_b^{zz} r_b}{\eta_b^2} + \frac{\sigma_a^{zz} r_a}{\eta_a^2} \right) \frac{dW_{ab}}{dz_a} \quad (5.28)$$

### 5.3.2. Correction close to symmetry axis

A major issue with axisymmetric SPH is the treatment of particles that are close to the symmetric axis. Indeed, large errors in density and consequently other quantities can be observed with particles at distance less than  $2h$  from the axis. Errors in evaluating density and other parameters such as velocity, stress, strain etc. close to the axis can lead inaccurate or even unstable simulations. A mathematically consistent solution to tackle this issue is especially necessary for a problem like cavitation where the dynamics of the imploding bubble, near the symmetry axis, is very rapid and therefore the region close to the symmetry axis is of utmost importance. To understand the issue better, let's consider a particle in the vicinity of the symmetry axis moving towards the axis. Equation 5.24 suggests that the 2D density of a particle is directly and linearly proportional to the radial distance from the axis. As the particle approaches the symmetry axis, the 2D density of the particle should tend to zero. However,

because of the presence of the ghost particles, the profile of  $\eta = 2\pi|r|\rho$ , is no longer linear when the particle radius is lower than  $2h$ . The limited capability of standard kernels to interpolate accurately non-linear functions introduces error in the density calculation. In other words, the density of a particle on the symmetry axis should be zero according to equation 5.24; however, the interpolation using particles on the right of the axis (actual particles) and the left of the axis (ghost particle) using the standard kernels would lead to a non-zero 2D density which is clearly wrong. Usually, the errors are small and the interpolation is precise to second order in  $h$  far from the axis. Unfortunately, close to the symmetry axis errors are much larger so that density and other physical quantities are not well reproduced.

One mathematically consistent way to overcome the issue is to use a modified interpolation kernel according to the particular geometry of the system (spherical or cylindrical) [83]. The resulting scheme does not have inaccurate density when the particles approach the axis. However, the modified kernel does not have an analytical expression and numerical integration is required to calculate the value of the kernel and its derivatives at every time step which require significantly higher computational effort. Later, a fitting formula for the modified kernels was proposed [84] but still involving a large number of operations which slow down the calculation. An alternative approach was proposed where without modifying the basic SPH scheme, correction terms are introduced to equations 5.6, 5.25 and 5.26, which become significant only close to the symmetry axis [77]. A detailed derivation has been provided by García-Senz *et al.* [77] where density is corrected close to the symmetry axis and consequently the momentum and energy equations as well for a fluid system.

We start with the same approach as proposed in [77], where the corrected density equation is given by

$$\hat{\eta}_a = \sum_{b=1}^N m_b W_{ab} \times f_1^a \quad (5.29)$$

where  $\hat{\eta}_a$  is the new corrected 2D density for particle  $a$  and  $f_1^a$  is the correction function which is prominent close to the symmetry axis and equals 1 far away from the symmetry axis such that the density of the particle tends to zero as the radial distance of the particle goes to zero. A detailed derivation for the correction factor  $f_1^a$  can be found in [77]. The function  $f_1^a$  for a particle  $a$  is given by

$$f_1^a = \begin{cases} \left[ \frac{7}{15} \zeta_a^{-1} + \frac{2}{3} \zeta_a - \frac{1}{6} \zeta_a^3 + \frac{1}{20} \zeta_a^4 \right]^{-1} & 0 \leq \zeta_a \leq 1 \\ \left[ \frac{8}{15} \zeta_a^{-1} - \frac{1}{3} + \frac{4}{3} \zeta_a - \frac{2}{3} \zeta_a^2 + \frac{1}{6} \zeta_a^3 - \frac{1}{60} \zeta_a^4 \right]^{-1} & 1 \leq \zeta_a \leq 2 \\ 1 & \zeta_a \geq 2 \end{cases} \quad (5.30)$$

where  $\zeta_a = r_a/h_a$ ,  $r_a$  being the radial distance from the symmetry axis and  $h_a$  is the smoothing length of the kernel. However, the above corrective function  $f_1^a$  is only applicable to the cubic-spline kernel function. Hence, the above-mentioned density correction function is applicable to any axisymmetric SPH solver using a cubic-spline kernel. It applies to all materials irrespective of it being fluid and solid. However, the further derivations required for the momentum equations due to the density correction will vary depending on whether we solve for a solid or a fluid. The momentum correction derivation provided in [77] is only applicable for a fluid solver and not a solid solver, we thereby present a detailed derivation of the corrected equation in the case of a solid solver.

Since the density equation has been re-written as equation 5.29, the momentum equations should also be corrected to obtain correct acceleration and velocities for a particle close to the axis. For instance, the acceleration in the radial direction for a cylindrical system is given by

$$\frac{dv_a^r}{dt} = \frac{1}{\rho} \left( \frac{\partial \sigma^{rr}}{\partial r} + \frac{\sigma^{rr}}{r} + \frac{\partial \sigma^{rz}}{\partial z} - \frac{\sigma^{\theta\theta}}{r} \right) \quad (5.31)$$

We start with the first term on the right hand side of equation 5.31:

$$\left. \frac{dv_a^r}{dt} \right|_I = \frac{1}{\rho} \frac{\partial \sigma^{rr}}{\partial r} \quad (5.32)$$

This is calculated using the following identities:

$$\frac{\partial(r\sigma^{rr})}{\partial r} = \sigma^{rr} + r \frac{\partial \sigma^{rr}}{\partial r} \Rightarrow \frac{\partial \sigma^{rr}}{\partial r} = \frac{1}{r} \left( \frac{\partial(r\sigma^{rr})}{\partial r} - \sigma^{rr} \right) \quad (5.33)$$

$$\frac{\partial}{\partial r} \left( \frac{r\sigma^{rr}}{\eta} \right) = \frac{1}{\eta} \frac{\partial(r\sigma^{rr})}{\partial r} - \frac{1}{\eta^2} r\sigma^{rr} \frac{\partial \eta}{\partial r} \Rightarrow \frac{1}{\eta} \frac{\partial(r\sigma^{rr})}{\partial r} = \frac{\partial}{\partial r} \left( \frac{r\sigma^{rr}}{\eta} \right) + \frac{1}{\eta^2} r\sigma^{rr} \frac{\partial \eta}{\partial r} \quad (5.34)$$

Using corrected densities and the above identities, we can express equation 5.32 as

$$\left. \frac{dv_a^r}{dt} \right|_I = \frac{2\pi}{\hat{\eta}} \left( \frac{\partial(r\sigma^{rr})}{\partial r} - \sigma^{rr} \right) = \frac{\partial}{\partial r} \left( \frac{2\pi r \sigma^{rr}}{\hat{\eta}} \right) + \frac{2\pi r \sigma^{rr}}{\hat{\eta}^2} \frac{\partial \hat{\eta}}{\partial r} - \frac{2\pi \sigma^{rr}}{\hat{\eta}} \quad (5.35)$$

where the derivative of the corrected density can be expressed as

$$\frac{\partial \hat{\eta}}{\partial r} = \frac{\partial(\eta \cdot f_1(\zeta))}{\partial r} = f_1(\zeta) \frac{\partial \eta}{\partial r} + \eta \frac{\partial f_1(\zeta)}{\partial r} \quad (5.36)$$

A similar approach is used for the third term on the right hand side of equation 5.31:

$$\left. \frac{dv_a^r}{dt} \right|_{III} = \frac{1}{\rho} \frac{\partial \sigma^{rz}}{\partial z} \quad (5.37)$$

which can be re-written as

$$\left. \frac{dv_a^r}{dt} \right|_{III} = \frac{2\pi r}{\hat{\eta}} \frac{\partial \sigma^{rz}}{\partial z} = \frac{2\pi r \sigma^{rz}}{\hat{\eta}^2} \frac{\partial \hat{\eta}}{\partial z} + \frac{\partial}{\partial z} \left( \frac{2\pi r \sigma^{rz}}{\hat{\eta}} \right) \quad (5.38)$$

Finally, all the terms are added together to give the derivative of the radial velocity w.r.t. time

$$\frac{dv_a^r}{dt} = \frac{\partial}{\partial r} \left( \frac{2\pi r \sigma^{rr}}{\hat{\eta}} \right) + \frac{2\pi r \sigma^{rr}}{\hat{\eta}^2} \frac{\partial \hat{\eta}}{\partial r} + \frac{2\pi r \sigma^{rz}}{\hat{\eta}^2} \frac{\partial \hat{\eta}}{\partial z} + \frac{\partial}{\partial z} \left( \frac{2\pi r \sigma^{rz}}{\hat{\eta}} \right) - \frac{2\pi \sigma^{\theta\theta}}{\hat{\eta}} \quad (5.39)$$

The same approach is applied to derive a similar expression for derivative of z-velocity w.r.t. time (the first term of the right hand side of equation 5.26)

$$\left. \frac{dv^z}{dt} \right|_I = \frac{1}{\rho} \frac{\partial \sigma^{zz}}{\partial z} = \frac{2\pi r}{\hat{\eta}} \frac{\partial \sigma^{zz}}{\partial z} \quad (5.40)$$

Using the following identity

$$2\pi r \frac{\partial}{\partial z} \left( \frac{\sigma^{zz}}{\eta} \right) = \frac{2\pi r}{\eta} \frac{\partial \sigma^{zz}}{\partial z} - \frac{2\pi r}{\eta^2} \sigma^{zz} \frac{\partial \eta}{\partial z} \Rightarrow \frac{2\pi r}{\eta} \frac{\partial \sigma^{zz}}{\partial z} = \frac{2\pi r}{\eta^2} \sigma^{zz} \frac{\partial \eta}{\partial z} + 2\pi r \frac{\partial}{\partial z} \left( \frac{\sigma^{zz}}{\eta} \right) \quad (5.41)$$

equation 5.40 can be written as

$$\left. \frac{dv^z}{dt} \right|_I = \frac{2\pi r}{\hat{\eta}^2} \sigma^{zz} \frac{\partial \hat{\eta}}{\partial z} + 2\pi r \frac{\partial}{\partial z} \left( \frac{\sigma^{zz}}{\hat{\eta}} \right) \quad (5.42)$$

Similarly, the third term of equation 5.26 can be written as

$$\left. \frac{dv^z}{dt} \right|_{III} = \frac{1}{\rho} \frac{\partial \sigma^{rz}}{\partial r} = \frac{2\pi r}{\hat{\eta}} \frac{\partial \sigma^{rz}}{\partial r} \quad (5.43)$$

The above equation has the same form as equation 5.32 (the difference being that the quantities inside the derivative are different components of stress), hence applying the same identities as applied for equation 5.33 leads to

$$\left. \frac{dv^z}{dt} \right|_{III} = \frac{\partial}{\partial r} \left( \frac{2\pi r \sigma^{rz}}{\hat{\eta}} \right) + \frac{2\pi r \sigma^{rz}}{\hat{\eta}^2} \frac{\partial \hat{\eta}}{\partial r} - \frac{2\pi \sigma^{rz}}{\hat{\eta}} \quad (5.44)$$

Finally, all the terms are added together to give the derivative of the axial velocity (z-direction) w.r.t. time

$$\left. \frac{dv^z}{dt} \right| = \frac{\partial}{\partial r} \left( \frac{2\pi r \sigma^{rz}}{\hat{\eta}} \right) + \frac{2\pi r \sigma^{rz}}{\hat{\eta}^2} \frac{\partial \hat{\eta}}{\partial r} + \frac{2\pi r}{\hat{\eta}^2} \sigma^{zz} \frac{\partial \hat{\eta}}{\partial z} + 2\pi r \frac{\partial}{\partial z} \left( \frac{\sigma^{zz}}{\hat{\eta}} \right) \quad (5.45)$$

The resulting momentum equation given by equations 5.39 and 5.45 are rewritten in discrete SPH form as:

$$\frac{dv_a^r}{dt} = 2\pi \sum_b m_b \left( \frac{\sigma_b^{rr} r_b}{\hat{\eta}_b^2} + \frac{\sigma_a^{rr} r_a}{\hat{\eta}_a^2} \times f_1^a \right) \frac{dW_{ab}}{dr_a} + 2\pi \sum_b m_b \left( \frac{\sigma_b^{rz} r_b}{\hat{\eta}_b^2} + \frac{\sigma_a^{rz} r_a}{\hat{\eta}_a^2} \times f_1^a \right) \frac{dW_{ab}}{dz_a} - 2\pi \frac{\sigma_a^{\theta\theta}}{\hat{\eta}_a} + \frac{2\pi r_a \sigma_a^{rr}}{\hat{\eta}_a f_1^a} \times \frac{df_1^a}{dr_a} \quad (5.46)$$

$$\frac{dv_a^z}{dt} = 2\pi \sum_b m_b \left( \frac{\sigma_b^{rz} r_b}{\hat{\eta}_b^2} + \frac{\sigma_a^{rz} r_a}{\hat{\eta}_a^2} \times f_1^a \right) \frac{dW_{ab}}{dr_a} + 2\pi \sum_b m_b \left( \frac{\sigma_b^{zz} r_b}{\hat{\eta}_b^2} + \frac{\sigma_a^{zz} r_a}{\hat{\eta}_a^2} \times f_1^a \right) \frac{dW_{ab}}{dz_a} + \frac{2\pi r_a \sigma_a^{rz}}{\hat{\eta}_a f_1^a} \times \frac{df_1^a}{dr_a} \quad (5.47)$$

The above momentum equations give a mathematically consistent solution for the treatment of particles close to the symmetry axis.

### 5.3.3. Validation test case for the axisymmetric SPH solid solver

The axisymmetric elasto-plastic solver is implemented and the simulation of an indentation is carried out as a test case to validate the solver. The indentation test is chosen for two primary reasons. Firstly, the indentation will induce a maximum displacement in vicinity of the symmetry axis and hence it will be a good test to identify the possible errors caused by the new scheme developed in the paper. Secondly, the load applied during indentation is chosen to be similar to that of cavitation due to a single bubble collapse.

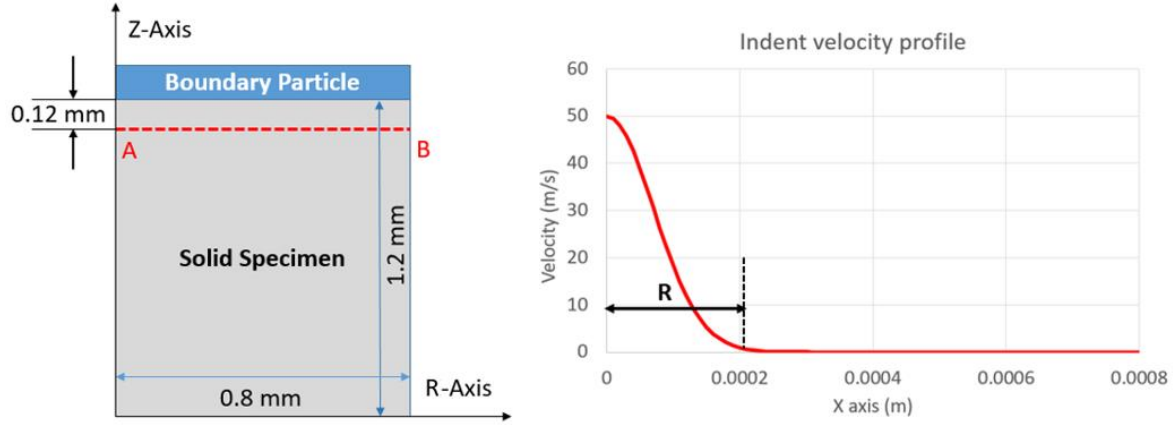


Figure 5.4. The figure on the left shows the computational domain for solid simulation, the boundary particles marked in blue are given a downward velocity with a Gaussian shape as plotted on the right. The extent of the velocity profile  $R$  is defined as the distance from the center where the velocity is 1% of the peak value, a non-uniform but constant velocity is given to the indenter.

Figure 5.4 shows the domain used for indentation simulations. Stainless steel A-2205 is simulated, the material properties are as follows [69]: Young's Modulus  $E=186$  GPa, Poisson's ratio  $\nu=0.3$  and the yield curve given by

$$\sigma_y(\varepsilon_p, \dot{\varepsilon}_p, T) = [A_0 + B_0(\varepsilon_p)^n][1 + C_0 \ln(\dot{\varepsilon}_p^*)] \quad (5.48)$$

where  $A_0=508$  MPa,  $B_0=832$  MPa,  $C_0=0.031$ ,  $n=0.29$  and  $\dot{\varepsilon}_p^* = \frac{\dot{\varepsilon}_p}{\dot{\varepsilon}_{p0}}$ , where  $\dot{\varepsilon}_{p0}$  (reference strain rate of the quasi static test) is  $0.05 \text{ s}^{-1}$ . The ultimate plastic strain to failure is set to  $\varepsilon_u=0.03$ . In this validation step, the strain rate sensitivity coefficient  $C_0$  will be taken as 0 so the behaviour will be assumed to be strain rate insensitive.

A localized indentation load is applied to the material using boundary particles with a prescribed velocity along the z-axis which depends on the distance to the axis. The velocity profile is shown in the right of Figure 5.4. Such a localized profile should create a continuously growing pit in the material. Consequently, it is expected that the material will first start to deform elastically, then some plasticity will develop in the most loaded region and finally some damage will initiate where the cumulated plastic strain exceeds the ultimate strain. The reason for using such a loading instead of an indenter itself is because using an indenter would require a free surface of the solid where indentation would be imposed. Free surfaces in solid or fluid SPH codes require special treatment as the particles near the free surface do not see a full kernel

but a truncated one. To solve this most solvers, use density normalization on algorithms, these algorithm work quite well with 2D and 3D solvers where all the particle have the same mass. However, for an axisymmetric solver where the mass of the particle is dependent on the initial radius and the mass is not constant for all particles, such a density normalization scheme does not work well, specially near the axis where density calculations are not straightforward. Hence to avoid such issues a layer of boundary particle is used such that the top surface could also see a full kernel due to the presence of the boundary particles. A velocity type boundary condition is imposed to create a continuously growing pit. The right end of the domain is set as a wall which is allowed to move in the Z direction. The bottom of the domain ( $z = 0$ ) is also set as a wall that is allowed to move in the X direction.

To validate whether the scheme and the equations derived using the density correction (equation 5.29, 5.46, 5.47) are capable of simulating the solid behaviour with an acceptable accuracy, the same case is setup in FEM and the axisymmetric SPH solver (with and without the novel mathematically consistent solution near the symmetry axis) is compared against FEM results. A quasi-static FEM simulations have been performed with CAST3M [79] using 3456 8-node cells with a minimum mesh size of 2  $\mu\text{m}$  and the same velocity profile is applied to the top nodes of the mesh as Dirichlet boundary conditions. The SPH simulation has been performed using 125570 particles and initial inter-particle distance of 2.5  $\mu\text{m}$  and a smoothing length  $2h = 6.5 \mu\text{m}$ .

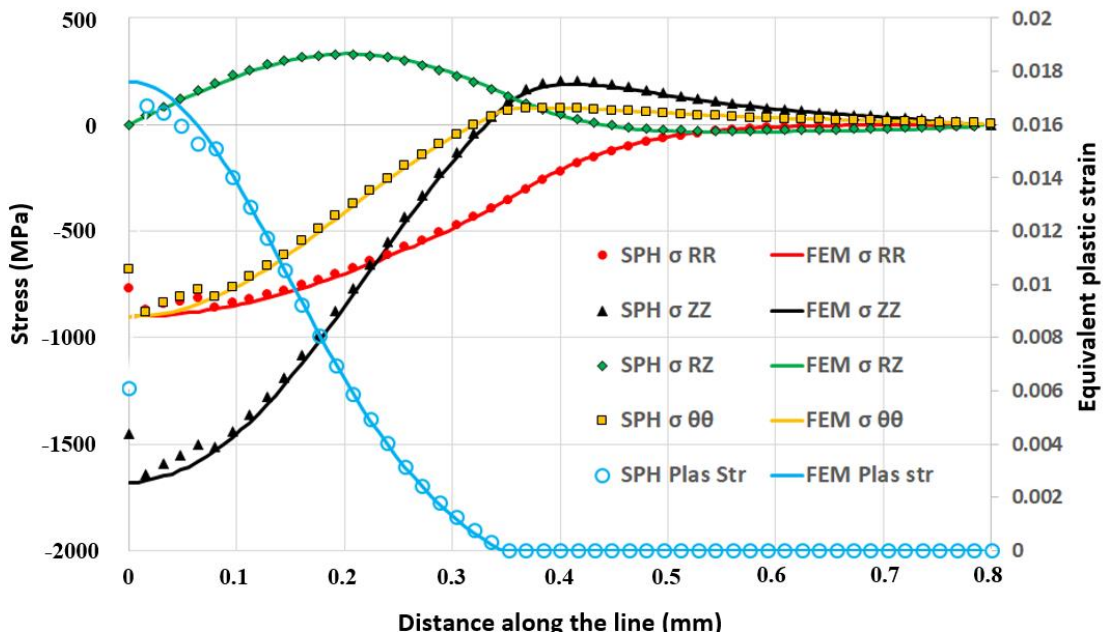


Figure 5.5a. FEM results compared against SPH (with ghost particles) without any correction near the axis (using equation 5.23, 5.27, 5.28) for a pit of 6 microns in depth and 0.4 mm in radius for a

stainless steel A-2205 specimen, the results are plotted on the horizontal red dotted line in figure 4 (0.12 mm below the top surface).

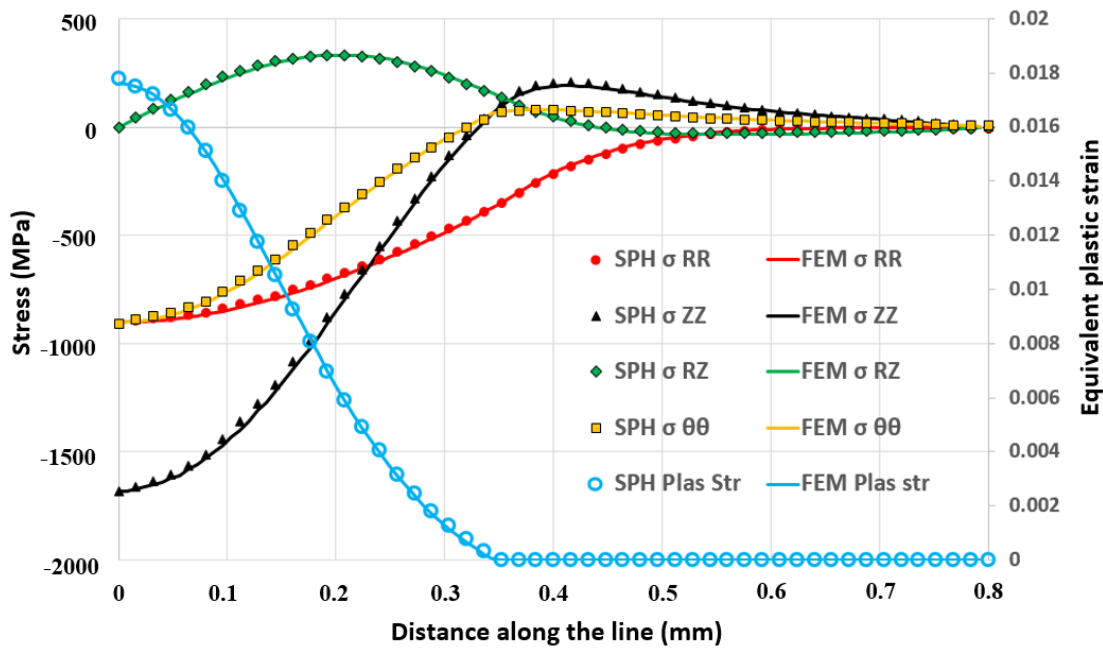


Figure 5.5b. FEM results compared against SPH (with ghost particles) with correction scheme proposed in this paper (using equation 5.29, 5.46, 5.47) for a pit of 6 microns in depth and 0.4 mm in radius for a stainless steel A-2205 specimen, the results are plotted on the horizontal red dotted line in figure 4 (0.12 mm below the top surface).

Firstly, we demonstrate that the existing method to solve solid mechanics in axisymmetric SPH without using the corrections derived in this paper (using equation 5.23, 5.27, 5.28) does not reproduce the solid behaviour close to the axis with acceptable accuracy. Figure 5.5a shows comparison of stress components (left axis of the graph in figure 5.5a) and plastic strain (right axis of the graph in figure 5.5a) along line AB (dashed in red) shown in the left of Figure 4 when the pit depth has reached 6  $\mu\text{m}$ . It is clearly observed that the stress and plastic strain near the axis are not well reproduced, a maximum error of 15% in stress components close to the axis and an error of 60% for plastic strain close to the axis is observed.

The same comparison is now performed in Figure 5.5b with the modified version of the SPH solver including the corrections derived in this paper. The average error is less than 1% suggesting an excellent agreement between the SPH and FEM results, hence validating the corrected density and momentum equations derived in this paper (equation 5.29, 5.46, 5.47). Also contours of plastic strain obtained from the FEM and SPH simulations are shown in figure

5.5c which shows that the FEM and SPH produce very similar plastic strain patterns in the material.

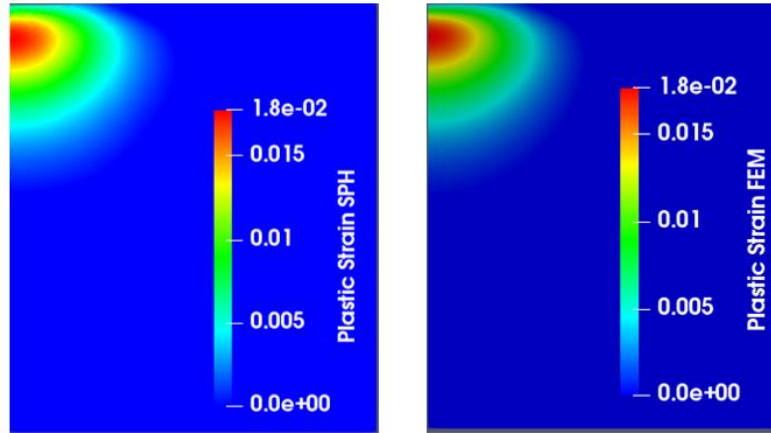


Figure 5.5c. FEM and SPH (with correction scheme proposed in this paper) plastic strain contours for a pit of 6 microns in depth and 0.4 mm in radius for a stainless steel A-2205 specimen.

## 5.4 SPH simulations for solid response

### 5.4.1. Mass loss simulation

We further use the solver to demonstrate that it is possible to run mass loss simulations using the axisymmetric SPH solver. We keep the same domain and the same simulation parameters as demonstrated in Figure 5.4. To account for mass loss, a damage criterion is to be introduced into the model. A thorough review of such models is provided by Pineau *et al.* [78], these models are based on void growth theory wherein the void coalesce either under tension or shear to form cracks which eventually leads to damage (for details on these models please refer to the review article by Pineau *et al.* [78] and the references therein). However, in this paper, to demonstrate that it is possible to simulate mass loss simulation with SPH, we use a simple damage criterion based on the rupture strain [64].

A critical value of rupture strain is defined to predict whether the SPH particle is damaged or not. If the equivalent plastic strain is above the rupture strain the material can sustain,  $\epsilon_u$ , the particle is assumed damaged. Therefore, once the plastic strain for a particle reaches a threshold value of rupture strain ( $\epsilon_u = 0.03$ ), the particle is considered as fully damaged and the particle thereafter does not contribute to the nearby particle interactions. The value of rupture strain under tension is around 0.25 for stainless steel, however in order to demonstrate the capability

of SPH to solve for damage and also keeping the simulation time within acceptable range, we chose a lower value of rupture strain as 0.03.

Figure 5.6 shows a sequence of images from a simulation where such a damage criterion is used, the first image (Figure 5.6a) shows the plastic strain developing as the boundary particles start indenting the solid, the following image (Figure 5.6b) shows a higher plastic strain with peak plastic strain occurring at a certain depth below the top surface of the material. As expected the crack starts to propagate from the region of maximum plastic strain, the third image (Figure 5.6c) shows the crack propagating inside the material and finally (Figure 5.6d) material removal.

#### 5.4.2. Parametric study for different extend of indent profile

A parametric study is performed to obtain mass loss curves for different extend of the applied velocity profile as indicated by radius R in Figure 5.4, keeping the maximum velocity of indentation and other parameters the same. It should be noted that R is not an actual radius but just the extent of the velocity profile till it goes to 1% of the peak value. The mass loss curves vs. time are plotted in figure 5.8 for three different values of the extend of velocity profile (R) with coefficient  $C_0$  in equation 11 (Johnson-Cook model) varied as 0 and 0.031 to obtain non strain rate sensitive response and strain rate sensitive response respectively.

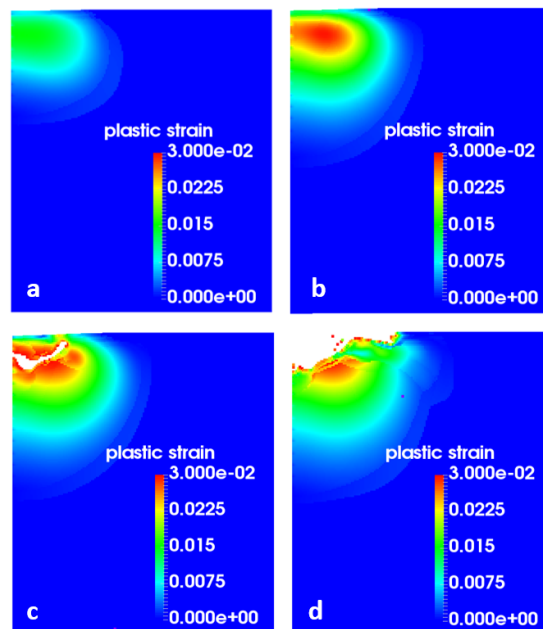


Figure 5.6. Sequence of images from SPH damage simulation of a stainless steel A-2205 specimen, (a) Shows the plastic strain accumulation in material without damage, (b) high plastic strain zone just

beneath the top surface, (c) damage initiation from the point of highest plastic strain, (d) material loss due to a single indent (domain size shown in the figure is same as in figure 5.4).

It can be noted that over a long period of time the larger radius of indent ( $R$ ) is able to produce larger mass loss. This is expected, since a larger extent of the applied load is able to create plastic deformation in a larger volume of material, hence producing higher mass loss. However, what is intriguing is the lower incubation period for a smaller radius of indent ( $R$ ). The incubation period is indicated as  $A$  in Figure 5.7. It is defined as the time required for material under load to initiate mass loss. The incubation period is an important parameter for most cavitation studies as it marks the initiation of material erosion. The cavitation erosion rate is roughly inversely proportional to the incubation time [89], which means that a longer incubation time would mean a slower rate of erosion. However, the trend observed from the mass loss curves in figure 5.8 is quite the opposite. An important aspect to investigate would be to understand how does the smaller radius of indent ( $R$ ) cause a quicker damage (low incubation time) in the material even though it produces higher rate of erosion.

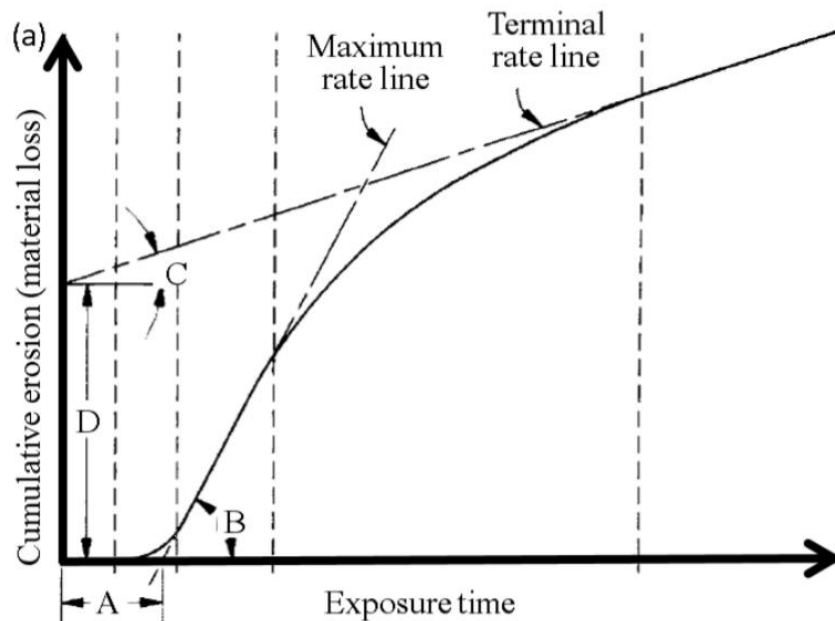


Figure 5.7. Characteristics of typical cumulative erosion versus exposure time curve.  $A$  = nominal incubation time;  $B$  = maximum erosion rate;  $C$  = terminal erosion rate; and  $D$  = terminal line intercept ([29]).

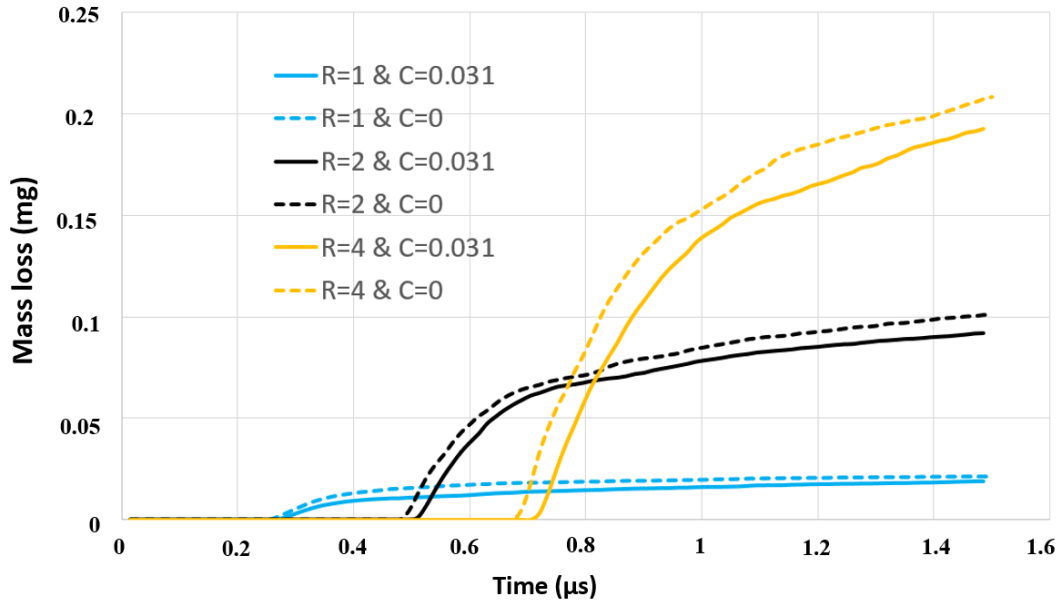


Figure 5.8. Mass loss curves for different extend of velocity profile ( $R$ ) on a stainless steel A-2205 specimen obtained from SPH simulations. The indentation depth is kept constant at  $6 \mu\text{m}$  for all cases while the indenter radius is varied from  $0.1 \text{ mm}$  to  $0.4 \text{ mm}$ .

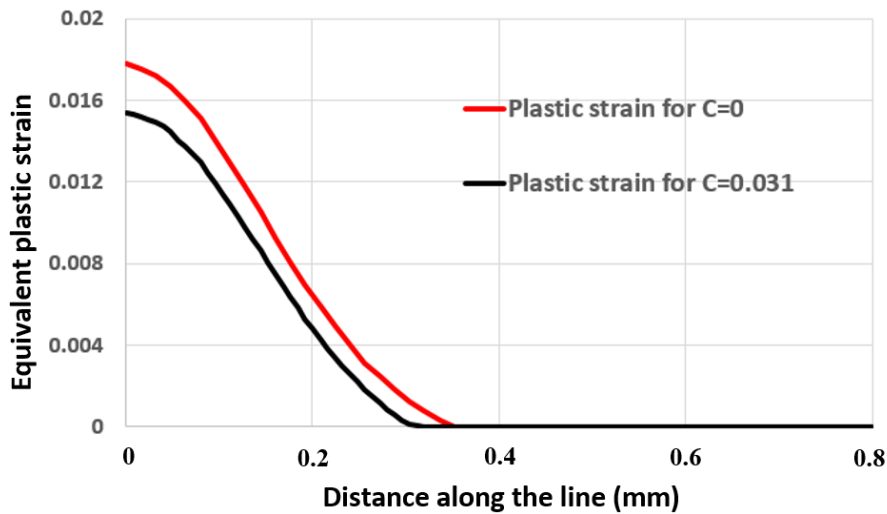


Figure 5.9. Shows plastic strain along the line AB marked for two cases, namely, one without strain rate sensitivity and the other with strain rate sensitivity.

To investigate this, Figure 5.10 shows a comparison of the stress profiles and the plastic strain for two different  $R$  ( $0.2 \text{ mm}$  and  $0.4 \text{ mm}$ ) along the line AB shown in figure 5.4. It can be observed that close to the symmetry axis, all the stress components are higher for the  $R=0.2$  compared to  $R=0.4$  leading to a higher plastic strain and hence a smaller incubation period. However, the larger radius of indent ( $R=0.4$ ) is able to induce plasticity within a larger volume of material and hence over a longer period of time shows higher mass loss. It should be noted

that the type of loading simulated here (indentation generated by the indent velocity) is quite different from the impact load due to bubble collapse and hence it remains to be seen whether such a phenomenon (relatively higher incubation time for higher erosion rate) could be observed for a fluid structure interaction simulation of a bubble collapse near a solid. If indeed a smaller bubble could lead to a lower incubation period and a low rate of erosion compared to larger bubble still remains to be investigated in further studies.

#### **5.4.3. Strain rate effects**

An important aspect of cavitation loading is that it can produce high strain rates and hence could lead to strain rate hardening in the material, thus lowering the rate of erosion. We numerically investigate the phenomenon by varying the coefficient  $C_0$  in equation 5.11 as 0 and 0.031, where 0 corresponds a non-strain rate sensitive material and 0.031 for a strain rate sensitive material like stainless steel. Rest of the material constants and simulation parameters are kept the same while  $C_0$  is varied from 0 to 0.031. We plot plastic strain for the two cases in figure 5.9 along the line AB (marked in figure 5.4), the strain rate insensitive simulation produces 10% higher plastic strain compared to the strain rate sensitive simulation. A similar behaviour could be observed in figure 8 where mass loss shows a deviation of around 8-15% between a strain rate insensitive and sensitive simulation. Incubation time is found to be 3-8% higher for the strain rate sensitive case ( $C_0=0.031$ ) compared to the strain rate insensitive case ( $C_0=0$ ). However, it should be noted that the maximum strain rate during these simulations were observed to be of the order of  $10^3 \text{ s}^{-1}$ , numerical and experimental cavitation studies indicate that the strain rate involved in cavitation erosion process could be as high as  $10^5$  or  $10^6 \text{ s}^{-1}$  [44, 69]. Hence the strain rate hardening effects in cavitation erosion can be expected to be much more prominent during cavitation loading.

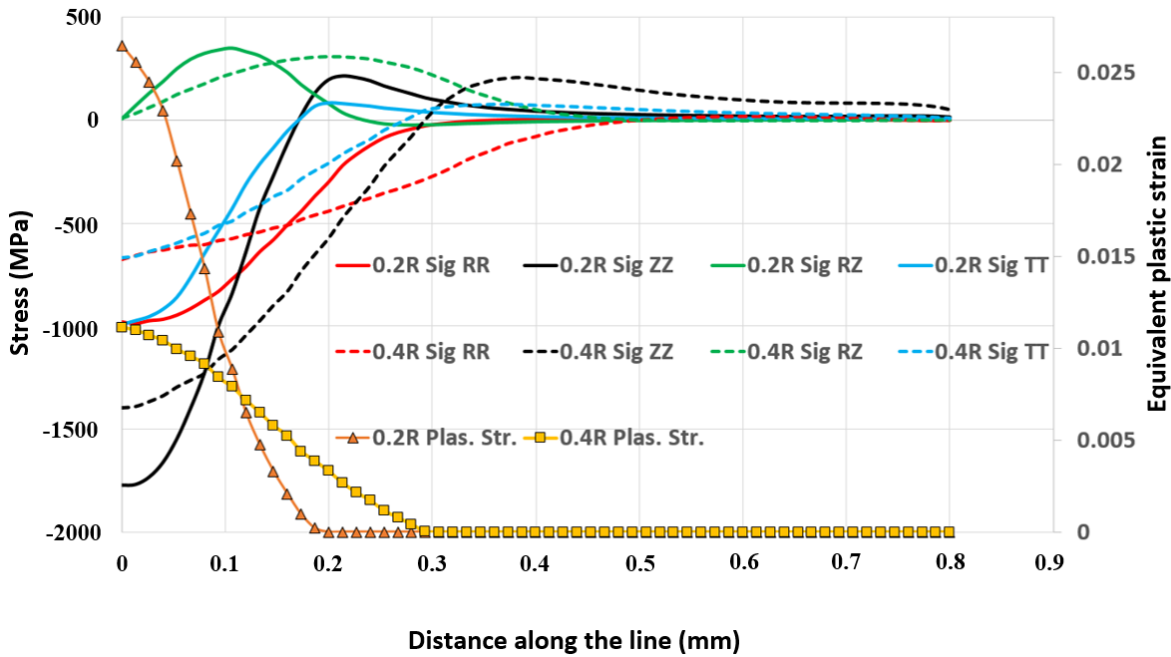


Figure 5.10. The graph shows components of stress and plastic strain plotted along the length of the red dotted line shown in figure 4 for two different values of extent of the velocity profile  $R=0.2$  (written as  $0.2R$  in the graph) and  $R=0.4$  mm (written as  $0.4R$  in the graph). The left axis indicates values for all component of stress and the right axis indicates plastic strain along the length of the line.

## 5.5 Conclusion and future work

An axisymmetric SPH solid solver is developed that can treat the particles close to the symmetry axis in a mathematically consistent way. The solver is capable of solving elasto-visco-plastic simulations with material damage and strain rate effects. An indentation test case is selected as a validation test case for reasons that firstly it can test the capability of the scheme in dealing with phenomenon near the symmetry axis and secondly that indentation loading is similar to cavitation loading. The results are compared against FEM results for the same case and an excellent agreement is observed. It is also demonstrated that the new formulation derived in the paper provides a much more accurate result near the symmetry axis compared to the existing method.

Mass loss curves were computed to demonstrate the capability of the model to solve for material damage. In this first study, the damage behaviour was simplistic. A more precise and sophisticated damage model should depend on various aspects such as [78]: cumulated plastic strain, stored energy, surface energy, stress triaxiality and strain rate. Various predictive models have been proposed so far in the past to determine fracture criteria considering all the above

parameters. Future work will consist of including a more realistic damage models in the SPH code using experimental measurements.

The mass loss curves obtained for different extents of the applied load have shown that the smallest extent of the indenter velocity profile  $R$  is the fastest to initiate damage but produces the lowest rate or erosion. The type of loading simulated here (indentation generated by the indent velocity) is quite different from the impact load due to bubble collapse. To understand the actual behaviour, further this solver will be coupled to a fluid SPH solver to solve for cavitation bubble collapse near a solid, it remains to be seen if such a trend can also be observed when comparing erosion caused due to two different size of bubbles.

## **Chapter Highlights**

- An axisymmetric SPH solid solver is developed that can treat the particles close to the symmetry axis in a mathematically consistent way using a novel method based on density correction close to the symmetry axis.
- The solver is capable of solving elasto-visco-plastic simulations with material damage and strain rate effects.
- Indentation simulation test is carried out and the results are compared against FEM results with and without the correction method derived in this thesis.
- Without the correction method derived in this thesis, large errors (60%) close to the symmetry axis can be observed. However, while using the corrections, the SPH results are observed to be within 1 % error close to the symmetry axis when compared to FEM results.
- Mass loss simulation are carried out for different indenter radius. Where, smaller the indenter, smaller the incubation time and higher the erosion rate.

# 6 FLUID STRUCTURE INTERACTION SOLVER

This chapter is constructed as the following paper which has been submitted to the Journal of Mechanics and Physics of Solid. The paper has been used as it is in the chapter, hence there could be a repetition of text, figures or tables as in the last chapters (1-5).

## **Fluid Structure-Interaction in cavitation erosion: Influence of strain rate and inertial effects on material response**

Shrey Joshi<sup>1,2</sup>, Jean Pierre Franc<sup>2</sup>, Giovanni Ghigliotti<sup>2</sup>, Marc Fivel<sup>1</sup>

<sup>1</sup>*Univ. Grenoble Alpes, CNRS, Grenoble INP, SIMaP, 38000 Grenoble, France*

<sup>2</sup>*Univ. Grenoble Alpes, CNRS, Grenoble INP, LEGI, 38000 Grenoble, France*

### **Abstract**

A Smoothed Particle Hydrodynamics axisymmetric solver was developed in order to simulate the collapse of a single cavitation bubble close to an elastic-plastic material and study plasticity formation and hence material erosion. Findings indicate the relative importance of the material deformation due to the impact of the micro-jet and the shock wave that develop during collapse. A shock-wave dominated impact has a much higher material erosion ability compared to a micro-jet impact. Strain rate is found to have a significant effect on plastic deformation, with an overestimation of the plastic deformation up to 60% if strain rate effects are neglected in the case of stainless steel A2205. We also demonstrate that, although the impact pressure is maximum just below the collapsing bubble, maximum plastic strain occurs at a radial offset from the symmetry axis. This is the result of inertial effects that have an impact on both the magnitude and the position of the plastic domain in the material. A new non-dimensional parameter called effective pressure is introduced that can predict plastic strain location accurately for higher stand-off ratios. Alternatively, a characteristic time analysis also shows that it can

be used for prediction of plastic strain zone in the solid for detached cavities.

**Keywords:** Smoothed Particle Hydrodynamics, cavitation erosion, fluid structure Interaction, plastic strain, inertial effects, strain rate effects

## 6.1. Introduction

Understanding cavitation erosion better has been a constant quest for cavitation research. The simplest cavitation erosion empirical models relate the erosion resistance derived from a standard cavitation test [5, 51-55] to the mechanical properties of the material such as Yield stress, Young's Modulus, hardness, toughness etc. Other kinds of empirical models relate the erosion resistance to the pitting rate or flow aggressiveness most often without considering material properties [59-61]. Models that can account for both the fluid and the solid behaviour were developed [44, 64-66], but some studies show that they fail to match the experimental results [64]. Considering the complex phenomenon of cavitation and the various aspects not considered in these models, hence it is needed to have much better ways to model material erosion. A lack of accurate numerical model for erosion calculation has been a bottleneck in understanding cavitation erosion. Most models as mentioned above either are empirical or phenomenological models that oversimplify the phenomenon of cavitation erosion. However, a few studies have tried solving for cavitation erosion using numerical methods such as FEM or even fluid structure interaction solvers that can provide a much better understanding. We focus on these studies and the shortcomings therein in order to improve the numerical scheme in the present work.

Some studies have used an inverse approach based on the Finite Element Method where it is assumed that the impact pressure due to a single bubble collapse has a Gaussian distribution in space [12, 68].

$$\sigma = \sigma_H \exp\left(-\left(\frac{2r}{d_H}\right)^2\right) \quad (6.1)$$

where,  $r$  is the radial distance to the symmetry axis and  $\sigma_H$  is the maximum amplitude of the hydrodynamic impact pressure and  $d_H$  is the diametric extent of the load. The inverse calculation provides the characteristics and the pressure distribution that could have led to a pit of given diameter and depth. This study was extended to dynamic loading [69] by adding a temporal evolution to the pressure, modifying equation 6.1 to the following equation

$$\sigma = \sigma_H \exp\left(-\left(\frac{2r}{d_H}\right)^2\right) \exp\left(-\left(\frac{t-t_{max}}{t_H}\right)^2\right) \quad (6.2)$$

Where  $t$  is time and  $t_{max}$  is the time when  $\sigma = \sigma_H$  and  $t_H$  is the characteristic impact rise duration. In a similar way  $d_H$  represents the radial spread of the load. The authors found that at high frequency or small characteristic loading time, the pits formed for the same pressure and radial spread appear to be smaller than the pits for the static case i.e. without temporal evolution of pressure. The results were attributed to strain rate and inertial effects. However, it would be interesting to analyse these effects under the actual loading due to a bubble collapse which is much more complicated than a simple Gaussian pressure.

To understand cavitation erosion in entirety, some studies have focused on fluid structure interaction (FSI) solvers [11, 13]. An initial footstep towards a numerical understanding of cavitation using FSI would be to understand the cavitation erosion phenomenon for a single cavitation bubble. Hsiao *et al.* have attempted to develop a cavitation FSI solver wherein both fluid and solid response can be captured [11]. In order to solve for the fluid bubble collapse, they use three codes: two fluid solvers, namely, boundary element method code (3DYNAFS-BEM) and a finite difference code (GEMINI), whereas the solid response was simulated using a finite element code (DYNA3D). The aim of having two fluid solvers is to create a hybrid scheme wherein the bubble collapse is solved using two different schemes which depend upon the kind of system to be solved. Cavitation bubbles create no shock waves during the growth phase and even during the collapse, shock waves are generated only towards the end of the collapse. Hence, they use the incompressible BEM until the end of the collapse where the flow is mostly incompressible. Once the shock wave generation is expected, the solver is switched to a compressible finite difference solver. At each iteration, the solid solver takes the pressure as input and solves for the material response. The code solves the material using a linear isotropic hardening law, however, most materials exhibit non-linear isotropic hardening. Also, the code does not consider strain rate hardening effects which are significant for fast dynamic phenomena like cavitation erosion.

Another work by Turangan *et al.* [13] studied fluid structure interaction using a Free-Lagrange scheme, FLM, that incorporates the compressibility, multi-phases and elastic plastic solid models. They simulated the collapse of 40  $\mu\text{m}$ -radius single bubbles attached to/near rigid and Aluminium walls by a 60 MPa-lithotripter shock, and the collapse of a 255  $\mu\text{m}$ -radius bubble attached to a 25  $\mu\text{m}$ -thick Aluminium foil by a 65 MPa-lithotripter shock. They simulated the

bubble with different stand-off distance and found that an attached cavity can produce larger deformation compared to a detached cavity. However, again the material model does not consider non-linear hardening and strain rate sensitivity.

A comprehensive cavitation FSI numerical model should ideally take into account the elastoplastic behaviour of the material as well as the development of damage. Since cavitation is a fast process, strain rate dependent hardening behaviour should be included in the model. Also, a fluid structure interaction scheme is required. During bubble collapse, high intensity shock waves are produced along with a micro jet. The shock wave travels through the fluid to the solid, a part of the wave is reflected back into the liquid and the rest gets transmitted to the solid [14]. A two-way coupling is required to model this behaviour properly.

In the present study a first attempt has been made to solve cavitation erosion using a meshless particle method, namely the Smoothed Particle Hydrodynamics (SPH) technique, and model both the fluid and the solid behaviour in a unique Lagrangian framework. The method offers the following advantages:

- Both fluid and solid response can be captured using the same solver and the same numerical method i.e. SPH. Both the solid and the fluid can be coded and solved within a single code making it much easier from the development perspective.
- Conventional methods of coupling a FVM solver to a FEM solver can be quite complicated and require dedicated procedures for data transfer across the two codes. The problem is eliminated here since the solver uses SPH for both solid and fluid in a common code; no such coupling is required; the data are easily exchanged within the RAM memory. For each particle, one only needs to specify if it is a fluid or a solid particle.
- The tricky mesh reconstruction for the fluid domain is eliminated when using meshless methods like SPH since both the fluid and the solid are solved using a Lagrangian formulation and hence such deformations are already taken care of via particle movement.

The existing 2D open source fluid SPH code SPHYSICS is used as a basis to develop the solver further [16]. The 2D solver is modified to 2D axisymmetric for the fluid solver. The axisymmetric solid solver is developed in-house. However, the axisymmetric SPH solver suffers from an inconsistent definition of density near the symmetry axis. A new method to mathematically resolve this issue for the axisymmetric solid SPH solver inspired by an approach used in fluid axisymmetric SPH simulations is used in the present study. The

axisymmetric fluid and solid solvers are validated against Rayleigh-Plesset collapse and FEM simulation respectively. The two solvers are eventually coupled together to obtain a fully coupled FSI solver capable of solving single bubble collapses over a solid medium to obtain elastic-plastic response using the Johnson-Cook model [19]. The paper presents simulations for a detached cavity and an attached cavity to understand the distinct material response the two cavities can produce. Attached and detached refers to whether the cavity surface is attached or detached to the solid medium respectively.

## 6.2. Methodology

A detailed methodology to change a 2D SPH solver to an axisymmetric SPH solver is provided in section 5.3.1. The SPH algorithm for solving a fluid and a solid together within a single code is provided in the following sections.

### 6.2.1. Fluid solver

A major issue with axisymmetric SPH is the treatment of particles that are close to the symmetry axis. Indeed, large errors in density and consequently other quantities can be observed with particles at distance less than  $2h$  from the axis. The fluid axisymmetric SPH scheme implemented in the present study uses a corrective function for density calculation near the symmetry axis. Further, the density correction leads to a corrected momentum equation [77].

The 2D density is calculated using the following equation,

$$\hat{\eta}_a = \sum_{b=1}^N m_b W_{ab} \times f_1^a \quad (6.3)$$

where  $\hat{\eta}_a$  is the new corrected 2D density for particle  $a$  and  $f_1^a$  is the correction function which is prominent close to the symmetry axis and equals 1 far away from the symmetry axis such that the density of the particle tends to zero as the radial distance of the particle goes to zero. Axisymmetric calculations use 2D density which is related to the actual 3D density by the following:

$$\eta_a = 2\pi |r_a| \rho_a \quad (6.4)$$

Detailed derivation for the correction factor  $f_1^a$  can be found in [77]. The function  $f_1^a$  for a particle  $a$  is given by

$$f_1^a = \begin{cases} \left[ \frac{7}{15} \zeta_a^{-1} + \frac{2}{3} \zeta_a - \frac{1}{6} \zeta_a^3 + \frac{1}{20} \zeta_a^4 \right]^{-1} & 0 \leq \zeta_a \leq 1 \\ \left[ \frac{8}{15} \zeta_a^{-1} - \frac{1}{3} + \frac{4}{3} \zeta_a - \frac{2}{3} \zeta_a^2 + \frac{1}{6} \zeta_a^3 - \frac{1}{60} \zeta_a^4 \right]^{-1} & 1 \leq \zeta_a \leq 2 \\ 1 & \zeta_a \geq 2 \end{cases} \quad (6.5)$$

where  $\zeta_a = r_a/h_a$ ,  $r_a$  being the radial distance from the symmetry axis and  $h_a$  is the smoothing length of the kernel.

Once the density is calculated, the pressure at each particle can be computed using an equation of state. In the present work, we use for liquid water the Tait equation of state that is given by the following,

$$P = B_1 \left[ \left( \frac{\rho}{\rho_0} \right)^\gamma - 1 \right] \quad (6.6)$$

where  $\gamma = 7$  and  $B_1 = c_0^2 \rho_0 / \gamma$ ,  $\rho_0 = 1000 \text{ kg m}^{-3}$  is the reference density and  $c_0$  is the sound speed at the reference density.

Since the density equation has been re-written as equation 6.3, the momentum equations should also be corrected to obtain correct acceleration and velocities for a particle close to the axis.

The acceleration in the radial and axial directions for a cylindrical system is given by,

$$\frac{dv_a^r}{dt} = 2\pi \frac{P_a}{\hat{\eta}_a} - 2\pi \sum_b m_b \left( \frac{P_b r_b}{\hat{\eta}_b^2} + \frac{P_a r_a}{\hat{\eta}_a^2} \times f_1^a \right) \frac{dW_{ab}}{dr_a} - \frac{2\pi r_a P_a}{\hat{\eta}_a f_1^a} \times \frac{df_1^a}{dr_a} - \sum_b m_b (\Pi_{ab}) \frac{dW_{ab}}{dr_a} \quad (6.7)$$

$$\frac{dv_a^z}{dt} = -2\pi \sum_b m_b \left( \frac{P_b r_b}{\hat{\eta}_b^2} + \frac{P_a r_a}{\hat{\eta}_a^2} \times f_1^a \right) \frac{dW_{ab}}{dz_a} - \sum_b m_b (\Pi_{ab}) \frac{dW_{ab}}{dz_a} \quad (6.8)$$

where,

$$\Pi_{ab} = \begin{cases} \frac{-\alpha \bar{c}_{ab} \mu_{ab} + \beta \mu_{ab}^2}{\bar{\rho}_{ab}} & \vec{v}_{ab} \vec{r}_{ab} < 0 \\ 0 & \vec{v}_{ab} \vec{r}_{ab} > 0 \end{cases} \quad (6.9)$$

$$\mu_{ab} = \frac{h \vec{v}_{ab} \vec{r}_{ab}}{\vec{r}_{ab}^2 + \eta^2} \quad (6.10)$$

Additional information regarding the equations 6.9 and 6.10 can be found in the work by Monaghan [20]. Once the particle acceleration is obtained from equations 6.7 and 6.8, the

acceleration is time integrated to obtain the velocities of each particle and eventually particles are moved at each time step according to their velocities (for details see [16]).

### 6.2.2. Solid solver

Section 5.3.2 presents a detailed derivation of corrected density and momentum equations near the symmetry axis for a solid SPH axisymmetric solver. The 2D density is calculated using equation 6.3 which remains the same as for the fluid. Velocities from the last time step are used to calculate the strain rate which is given by,

$$\rho_a \dot{\varepsilon}_a^{ij} = \frac{1}{2} \sum_{b=1}^n m_b \left[ (v_b^i - v_a^i) \frac{dW_{ab}}{dx_a^j} + (v_b^j - v_a^j) \frac{dW_{ab}}{dx_a^i} \right] \quad (6.11)$$

The strain rate can be time integrated to obtain the strain and eventually the stress using the following relation for an elastic solid,

$$\sigma_{ij} = 2\mu \varepsilon_{ij} + \lambda \delta_{ij} \varepsilon_{kk} \quad (6.12)$$

Once the stress is obtained, the acceleration of each particle is calculated using the following

$$\frac{dv_a^r}{dt} = 2\pi \sum_b m_b \left( \frac{\sigma_b^{rr} r_b}{\hat{\eta}_b^2} + \frac{\sigma_a^{rr} r_a}{\hat{\eta}_a^2} \times f_1^a \right) \frac{dW_{ab}}{dr_a} + 2\pi \sum_b m_b \left( \frac{\sigma_b^{rz} r_b}{\hat{\eta}_b^2} + \frac{\sigma_a^{rz} r_a}{\hat{\eta}_a^2} \times f_1^a \right) \frac{dW_{ab}}{dz_a} - 2\pi \frac{\sigma_a^{\theta\theta}}{\hat{\eta}_a} + \frac{2\pi r_a \sigma_a^{rr}}{\hat{\eta}_a f_1^a} \times \frac{df_1^a}{dr_a} \quad (6.13)$$

$$\frac{dv_a^z}{dt} = 2\pi \sum_b m_b \left( \frac{\sigma_b^{rz} r_b}{\hat{\eta}_b^2} + \frac{\sigma_a^{rz} r_a}{\hat{\eta}_a^2} \times f_1^a \right) \frac{dW_{ab}}{dr_a} + 2\pi \sum_b m_b \left( \frac{\sigma_b^{zz} r_b}{\hat{\eta}_b^2} + \frac{\sigma_a^{zz} r_a}{\hat{\eta}_a^2} \times f_1^a \right) \frac{dW_{ab}}{dz_a} + \frac{2\pi r_a \sigma_a^{rz}}{\hat{\eta}_a f_1^a} \times \frac{df_1^a}{dr_a} \quad (6.14)$$

Detailed derivation of these equations can be found in section 5.3.2. Further the accelerations can be used to obtain the new position of each particle in the same way as for the fluid. The above equations are only valid for an elastic solid. However plastic deformation is a key aspect in material response under cavitation load. To calculate plastic strain, the Johnson-Cook model is used (temperature effects are neglected in the paper),

$$\sigma_y(\varepsilon_p, \dot{\varepsilon}_p, T) = [A_0 + B_0(\varepsilon_p)^n][1 + C_0 \ln(\dot{\varepsilon}_p^*)] \quad (6.15)$$

where,  $A_0$ ,  $B_0$ ,  $C_0$ ,  $n$  are material constants,  $\dot{\varepsilon}_p^* = \frac{\dot{\varepsilon}_p}{\dot{\varepsilon}_{p0}}$  (the non-dimensional effective plastic strain rate) where  $\dot{\varepsilon}_{p0}$  is the reference plastic strain-rate of the quasi-static test used to determine the yield and hardening parameters  $A_0$ ,  $B_0$  and  $n$ . Details regarding plasticity calculation and return mapping algorithm for non-linear isotropic hardening are provided in Appendix B.

### 6.2.3. Fluid structure interaction in SPH

Since the solid and the fluid solver are coded within a single code, all particles irrespective of them being solid or fluid particles are solved at the same time. However, a few modifications are required for the particles close to the interface. Consider the situation in figure 6.1, where particle  $\mathbf{a}$  is a solid particle and its kernel contains fluid particles, one of them being particle  $\mathbf{b}$ . While calculating the density of the solid particle  $\mathbf{a}$ , the contribution from the fluid particle (which has a lower mass) can lead to underestimation of the density in the solid and overestimation of density in the fluid. In other words, a numerical density diffusion would be observed near the interface unless corrective measures are taken. To achieve this and avoid any numerical density diffusion, the density equation is modified to the following,

$$\hat{\eta}_a = \sum_{b=1}^N m_b W_{ab} \times f_1^a \times \frac{\rho_{a0}}{\rho_{b0}} \quad (6.16)$$

where  $\rho_{a0}$  and  $\rho_{b0}$  are the density of particle  $\mathbf{a}$  and  $\mathbf{b}$  respectively at the start of the simulation.

To transfer force across the interface while solving all the particles together, for any interaction of particle across the interface, the total force on a given particle  $\mathbf{a}$  due to particle  $\mathbf{b}$  can be resolved in the r-z direction (as marked in figure 6.1), while considering there is no interface but a continuum across the interface.

$$\vec{F}_{ab} = F_r \hat{i} + F_z \hat{j} \quad (6.17)$$

However, since there exists a discontinuity at the interface and in the absence of viscous forces, the force parallel to the interface should be zero. Hence the force vector is multiplied by the vector normal to the interface to obtain the final force on the particle.

$$\vec{F}_{ab}^{Interface} = F_r n_r \hat{i} + F_z n_z \hat{j} \quad (6.18)$$

The above equation along with the momentum equation is enough to satisfy the Neumann boundary condition to transfer the forces across the interface. As the particles across the interface are solved together within a single code and at the same time, the velocity at the interface always satisfies the Dirichlet boundary condition. However, to avoid any penetration and avoid disorder, XSPH [21] is used which takes into account not just the velocity of the particles itself but also the velocity of the nearby particles while moving it.

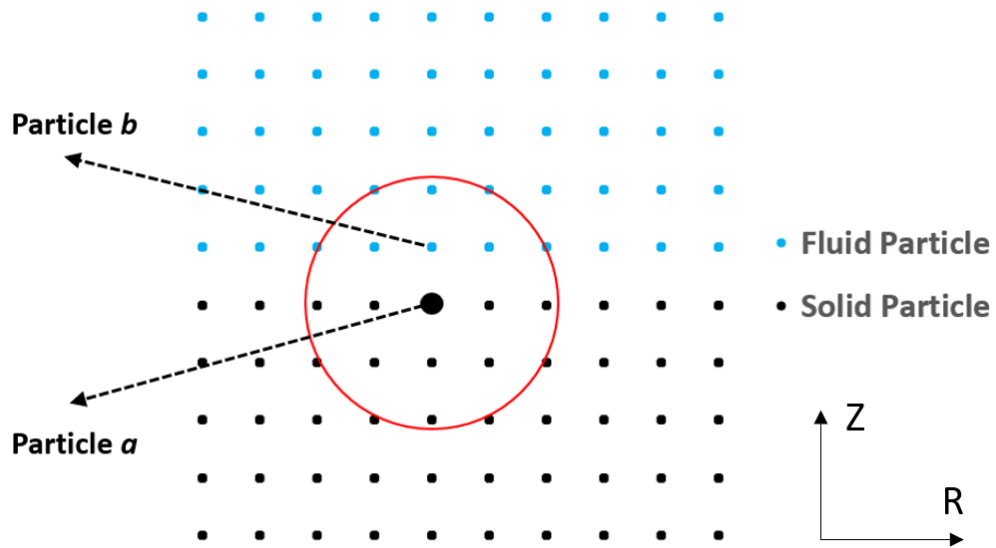


Figure 6.1. Interaction of solid and fluid particles near the interface, red circle represents the kernel of particle *a*.

### 6.3. Validations

#### 6.3.1. Fluid solver validation

To validate the fluid solver, a classic case of a spherical bubble collapse is carried out using SPH and compared against the analytical solution to the Rayleigh-Plesset equation. Figure 6.2 shows the domain used for a bubble collapse simulation in a large medium. A void bubble of radius 0.095 mm is placed in a spherical domain which is 7 times the bubble radius. A pressure wave of 60 MPa is generated by the wavemaker whereas the initial pressure inside the bubble is 0 Pa. All the domain walls are given a non-reflective boundary condition (the pressure waves are absorbed at these boundaries) to avoid any wave reflections hitting the bubble. To obtain such a pressure absorption boundary in SPH, the velocity of the particle near the boundary is progressively reduced to zero in order to avoid any reflection. The flow is treated as non-viscous and no surface tension forces are considered in the model. The wavemaker shown in the figure is a set of repulsive particles which apply force on the nearby particles, hence acting as a pressure wave generator. Figure 6.3 shows good agreement between SPH results and the analytical solution of Rayleigh-Plesset equation, which validates the fluid solver. The increase in bubble radius at the end of the collapse is due to the impact force at the center of the collapse which causes a rebound of these particles.

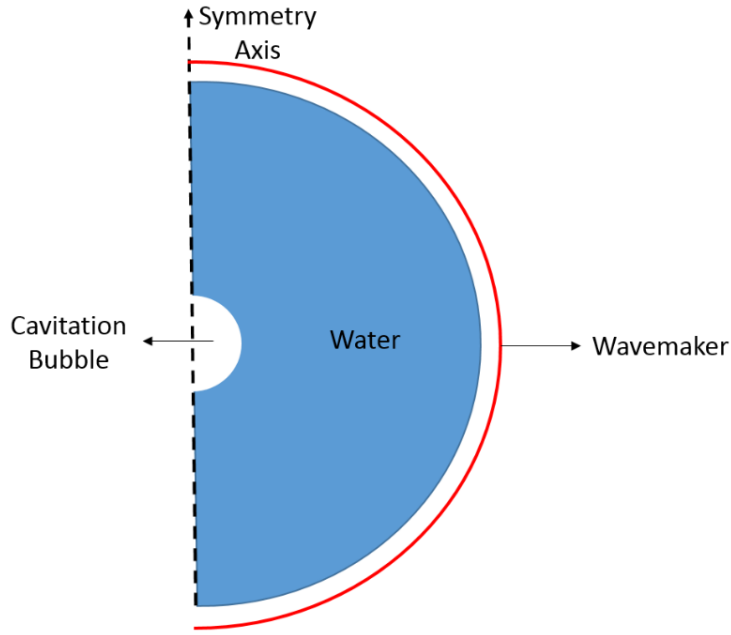


Figure 6.2. Simulation domain for bubble collapse simulation in 2D axisymmetric.

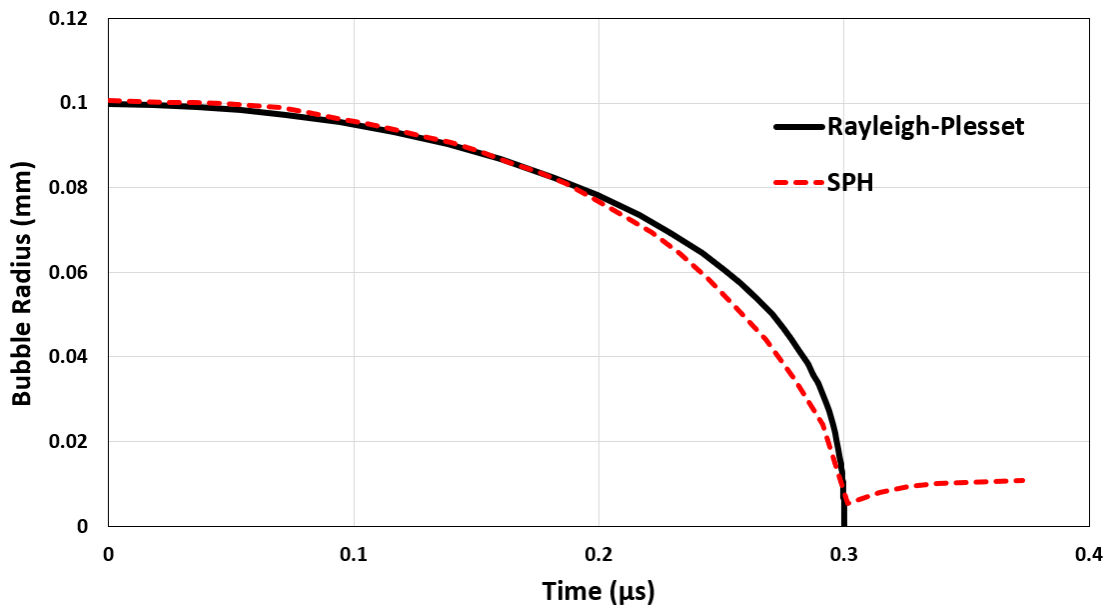


Figure 6.3. Comparison of bubble radius vs. time, SPH against Rayleigh-Plesset solution for a bubble collapse simulation (domain shown in figure 6.2).

### 6.3.2. Solid solver validation (skip if you read 5.3.3)

An indentation test is used to validate the SPH solid solver against an FEM solver. Figure 6.4 shows the domain used for indentation simulations. Stainless steel A-2205 is simulated. The material properties are as follows [69]: Young's Modulus  $E=186$  GPa, Poisson's ratio  $\nu=0.3$  and yield curve given by Johnson-Cook equation (6.15) where  $A_0 = 508$  MPa,  $B_0 = 832$  MPa,

$C_0 = 0.031$  &  $n = 0.29$  for A-2205 (Stainless Steel). In this validation step, the strain rate sensitivity coefficient  $C_0$  will be taken as 0 so the behaviour will be assumed to be strain rate insensitive.

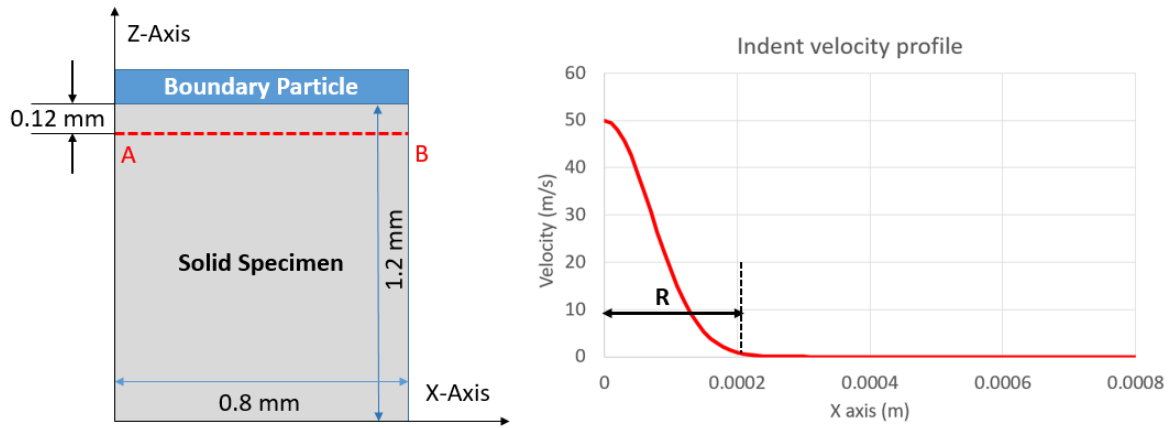


Figure 6.4. The figure on the left shows the computational domain for solid simulation, the boundary particles marked in blue are given a downward velocity with a Gaussian profile with the distance to the axis shape as plotted on the right. The extent of the velocity profile  $R$  is defined as the distance from the center where the velocity is 1% of the peak value, a non-uniform but constant velocity is given to the indenter.

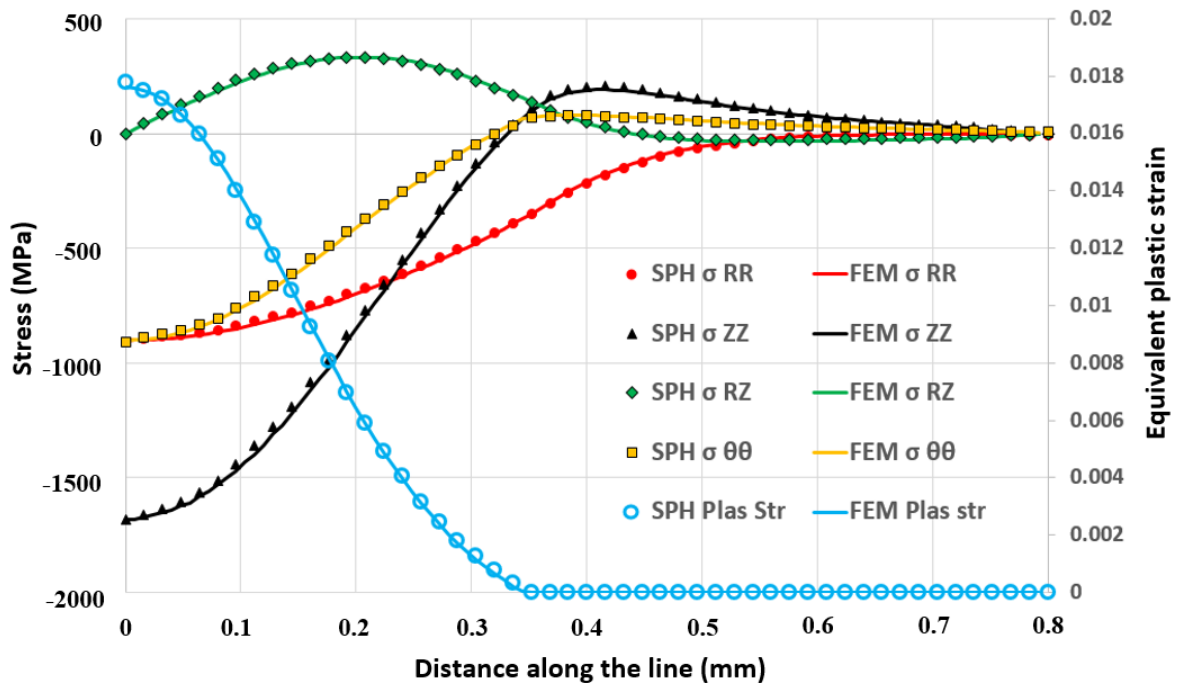


Figure 6.5. FEM results compared against SPH (for a pit of 6 microns in depth and 0.4 mm in radius for a stainless steel A-2205 specimen, the results are plotted on the horizontal red dotted line in figure 6.3 (0.12 mm below the top surface).

The same case is setup in FEM and the axisymmetric SPH solver, with the novel mathematically consistent solution near the symmetry axis. The FEM simulations have been performed with CAST3M [79] using 3456 8-node elements with a minimum mesh size of 2  $\mu\text{m}$  and the same velocity profile is applied to the top nodes of the mesh as Dirichlet boundary conditions. The SPH simulation has been performed using 125570 particles and initial inter-particle distance of 2.5  $\mu\text{m}$  and a smoothing length  $2h = 6.5 \mu\text{m}$ . Figure 6.5 shows a comparison of stress components and plastic strain along the line AB (marked in figure 6.3) for the SPH and FEM simulation. The comparison shows excellent agreement with average error less than 1% between the SPH and FEM. Figure 6.6 shows the plastic strain contours obtained for the SPH and FEM simulation.

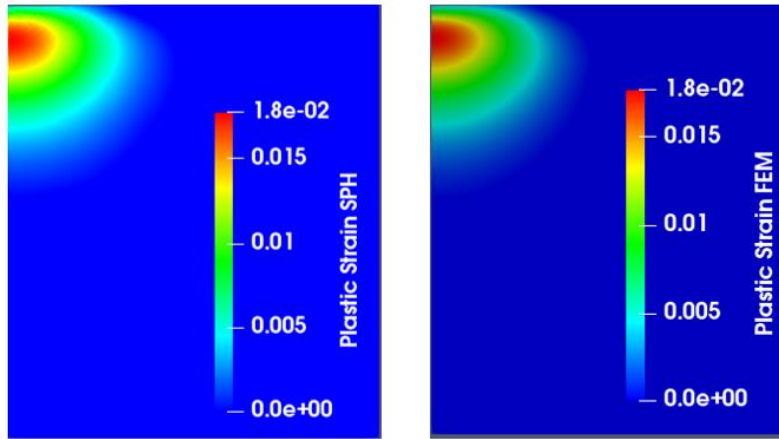


Figure 6.6. FEM and SPH plastic strain contours for a pit of 6 microns in depth and 0.4 mm in radius for a stainless steel A-2205 specimen.

#### 6.4. Results and discussion

In this paper, we present two different cases of bubble collapse over a deformable solid medium, one with the bubble attached to the solid and the other with the bubble detached from the solid. The following sections present the results for the two cases and we point out some interesting findings about the response of the material due to cavitation loading. The material parameters correspond to A2205 duplex stainless steel including strain rate sensitivity effects as identified by Roy *et al.* [69] i.e.:  $E = 186 \text{ GPa}$ ;  $n = 0.29$ ;  $A_0 = 508 \text{ MPa}$ ;  $B_0 = 832 \text{ MPa}$ ;  $C_0 = 0.031$ ;  $\dot{\epsilon}_{p0} = 0.05 \text{ s}^{-1}$ .

#### 6.4.1. Single bubble collapse: Detached cavity vs Attached cavity

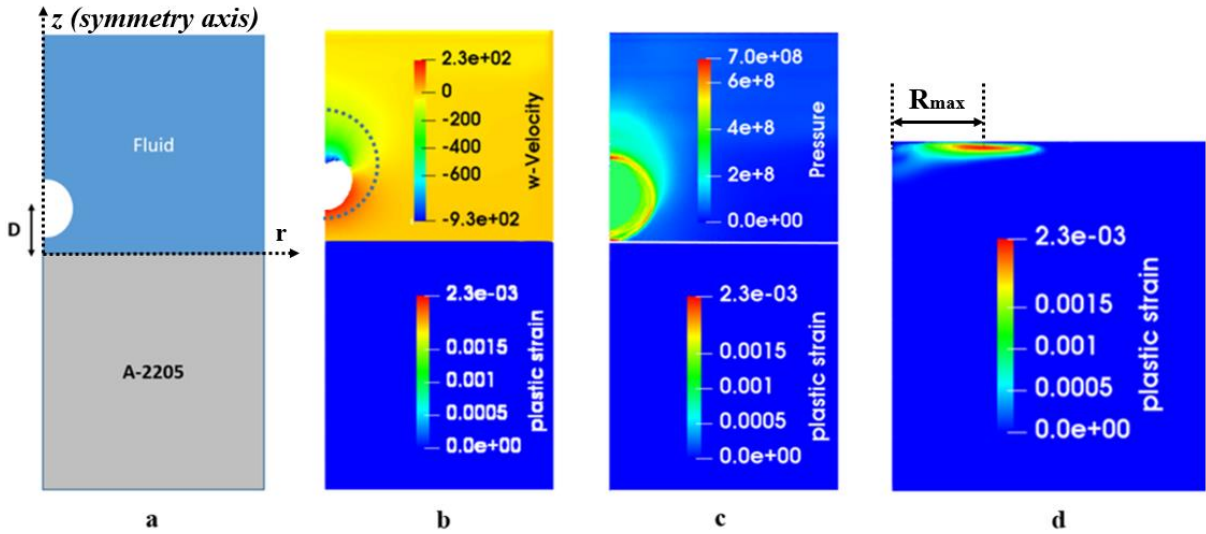


Figure 6.7(a) Sketch of the initial simulation domain for axisymmetric SPH FSI simulation of a detached cavity of radius  $R = 0.15$  mm and standoff ratio  $SR = 1.33$ , (b) shows contours of axial velocity in the fluid and plastic strain in the solid, a micro jet formation can be observed (the dotted semi-circle represents the initial bubble shape) at  $\tau = 0.92$ , (c) contours of pressure in the fluid and plastic strain in the solid, a shock wave generated due to the bubble collapse can be observed as it just reaches the interface at  $\tau = 1.053$ , (d) plastic strain contours in the solid at the end of the simulation, the maximum plastic strain occurs at a radial offset of  $R_{max}$  from the symmetry axis.

Figure 6.7a shows the sketch of the initial domain used for simulating a detached cavity collapse over a solid. A bubble diameter of 0.15 mm and a standoff ratio (SR) of 1.33 are used for the initial domain (where SR is defined as  $D/R$ ,  $D$  is the distance from the bubble centre to the interface and  $R$  is the radius of the bubble). The figures 6.7b-d show a sequence of images for the collapse of the cavity and subsequent response of the material. To initiate the collapse, a pressure wave of 50 MPa is generated using a wave generator from the top of the fluid domain, the right and bottom boundaries are set as rigid walls. Figure 6.7b shows contours of axial velocity ( $z$ -direction) in the fluid and plastic strain in the solid at  $\tau = 0.92$  (where  $\tau$  is the simulation time at that instance divided by time required for the bubble to collapse), with the formation of a micro jet after the pressure wave hits the bubble (the dotted circle in figure 6.7b shows the initial bubble before the start of collapse). Figure 6.7c shows contours of pressure in the fluid and plastic strain in the solid at  $\tau = 1.053$ . A shock wave is generated due to the micro jet hitting the liquid on the other side of the bubble as shown in figure 5.2. Figure 6.7c shows the shock just reaching the interface. This shock wave produces plastic deformation in the material as shown in Figure 6.7d. A maximum plastic strain of 0.23% can be observed just

beneath the interface and not at the solid surface. Surprisingly, the maximum plastic strain does not occur right beneath the center of the bubble but at an offset from the symmetry axis marked as distance  $R_{\max}$  in figure 6.7d. This material behaviour for the detached cavity will be dealt with in detail in section 6.4.4.

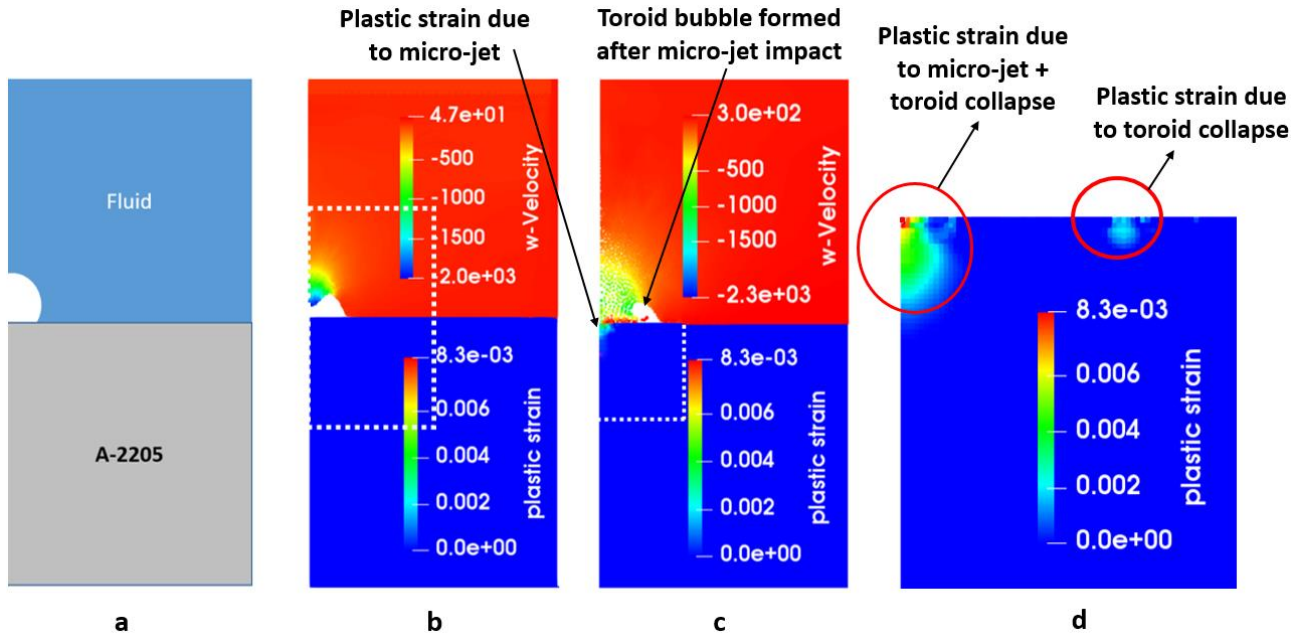


Figure 6.8(a) Sketch of the initial simulation domain for axisymmetric SPH FSI simulation of an attached cavity of radius  $R = 0.15$  mm, (b) shows contours of axial velocity in the fluid and plastic strain in the solid, a micro jet formation can be observed, (c) contours of axial velocity in the fluid and plastic strain in the solid, the micro jet shown in figure 6.8b hits the material and produces a very tiny zone of plastic strain (max plastic strain 0.0042) at the center (the contours in figure 6.8c are magnified along the white dotted rectangle shown in figure 6.8b), it also demonstrates the formation of a toroid bubble after the micro jet impact on the solid, (d) plastic strain contours in the solid at the end of the simulation, contour in the material shown in figure 6.8d is magnified along the white dotted line in figure 6.8c, two zones of plastic strain can be seen: one due to the toroid collapse and the other at the center due to the micro jet and also the shock wave from the toroid collapse.

Figure 6.8a shows the sketch of the initial domain used for simulating an attached cavity collapse over a solid. A bubble diameter of 0.15 mm and a standoff ratio (SR) of 0.66 are used for the initial domain. To initiate the collapse, a pressure wave of same amplitude 50 MPa is generated, still using a wave generator from the top of the fluid domain. As for the previous case of a detached cavity, a micro jet can be observed after the pressure wave hits the bubble (Fig. 6.8b). Figure 6.8c shows contours of axial velocity (z-direction) in the fluid and plastic strain in the solid (the contours are magnified along the white dotted rectangle marked in figure

6.8b). A tiny zone of localized plastic deformation (maximum plastic strain 0.42%) at the center is observed due to the micro jet hitting the material. Also, a toroidal bubble can be observed towards the right of the micro jet. The toroidal cavity then collapses to further produce plastic deformation in the material as shown in Figure 6.8d corresponding to the end of the simulation. As the toroid collapses, it produces plastic deformation below it (marked as plastic strain due to toroid collapse in figure 6.8d). Also, the shock wave due to the collapse of the toroidal bubble travels towards the center of the material and focuses on the axis to produce additional plastic deformation. A maximum plastic strain of 0.42% is produced due to the micro jet and thereafter an additional plastic deformation is observed at the center due to the shock wave produced by the toroid collapse to give a final maximum plastic strain of 0.83% at the center. This can be referred to as the primary zone of plastic deformation. A secondary zone of plastic deformation is observed below the point of toroid collapse with maximum plastic strain of 0.2%.

Comparing the two cases, the results suggest that the micro jet generated by the collapse of an attached cavity (see fig 6.8c, before the toroid collapse) has an ability to cause a larger (almost 2 times larger) plastic strain in the material as compared to the shock wave generated by the collapse of a detached cavity, for the same magnitude of pressure wave initiating the collapse and the same bubble size. As a result, it could be conjectured that, the repeated collapse of an attached cavity would lead to a smaller incubation time compared to the repeated collapse of a detached cavity. But it should also be noted that the volume of material that is plastically deformed in case of a micro jet is miniscule compared to a shock wave impact (almost 800 times smaller). This would imply that even though the incubation time for material erosion might be lower for a micro jet collapse, the shock wave can plastify a much larger volume of material and hence the erosion rate should be higher for a shock wave impact. Hence it could be inferred that the material erosion ability of a shock wave is much higher than that of a micro jet.

#### **6.4.2. Detached cavity material response**

We get our attention back to the unexpected material response observed for the detached cavity. As shown in Figure 6.7d, the maximum plastic strain does not occur right below the center of the bubble but at an offset  $R_{\max}$  from the symmetry axis. To understand this behaviour, we plot the pressure in the fluid along the interface (r-axis as shown in figure 6.7a) in figure 6.9 at different times. The plot shows that the maximum pressure decreases as we move ahead in time (time 1 to time 6), which is the expected behaviour for a spherical wave. Although the

maximum pressure for all times is observed at the symmetry axis, the maximum plastic strain occurs at an offset  $R_{\max}$  from the symmetry axis as shown by the red circle markers in figure 6.9. This behaviour is contrary to the popular belief that cavitation erosion occurs where the maximum pressure is observed at the interface. Two options are considered below to explain this behaviour.

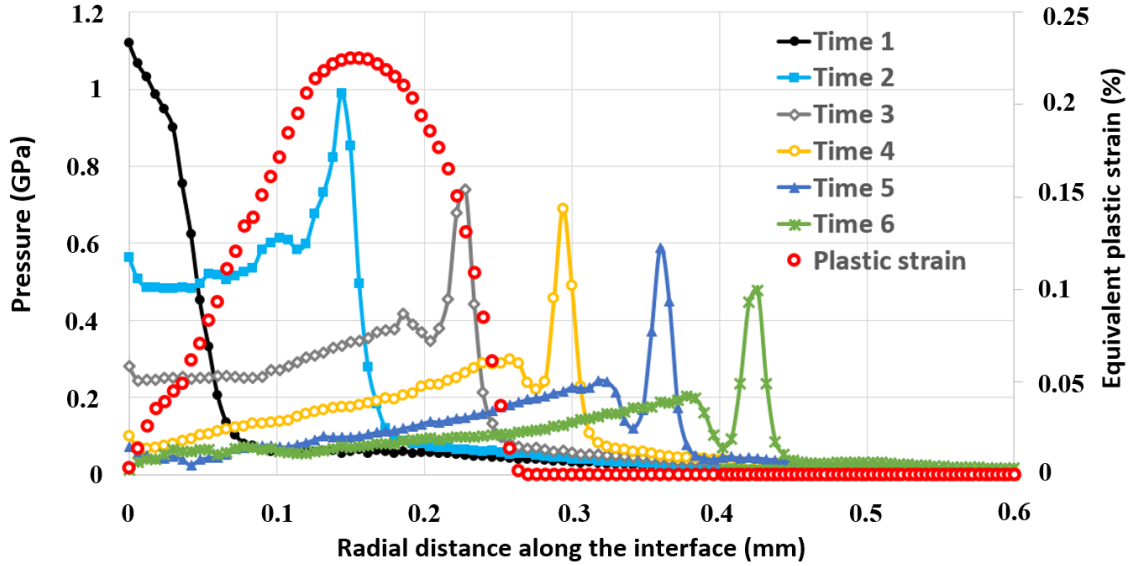


Figure 6.9. Plot of pressure (left axis) vs the distance along the interface for different times: Time 1 to Time 6 ( Time 1-6 refers to  $\tau = 1.053, 1.106, 1.16, 1.2, 1.24$  &  $1.28$  respectively, where  $\tau$  is the simulation time divided by the bubble collapse time), the right axis corresponding to the red circle markers refers to the plastic strain plotted along a line located just below the interface and parallel to it at the end of the simulation ( the line passes through the point of maximum plastic strain in the material).

### 6.4.3. Detached cavity: Strain rate effect

It could be due to strain rate effects, as the material can demonstrate hardening when strain rates are high. In order to examine this hypothesis, we eliminate strain rate dependency of yield stress by substituting  $C_0 = 0$  in equation 6.15, instead of  $C_0 = 0.031$  for the results presented in section 4.1. The contours of plastic strain for  $C_0 = 0$  are shown in figure 6.10. A maximum plastic strain of 0.37% can be observed which is 60% higher than for the  $C_0 = 0.0031$  case. However, the offset  $R_{\max}$  still remains the same for the two cases. Thus such a material behaviour is not due to the strain rate effects.

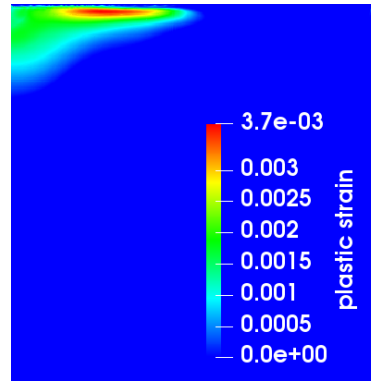


Figure 6.10. Contour of plastic strain in the material for  $C_0 = 0$  in equation 6.15 (refers to the case with no strain rate effect).

#### 6.4.4. Dynamic loading in cavitation

Since strain rate effects cannot account for the unexpected material behaviour for the detached cavity case, it could well be the fast dynamics during cavitation loading that can lead to such a behaviour. In order to analyse whether this is true, we follow the same strategy (as for the analysis of strain rate effects) by eliminating dynamic effects from the simulation. We achieve this by using the same load as seen by the material during an FSI simulation, but run a static simulation using an FEM solver since the present SPH solid solver cannot be used for static simulations.

##### 6.4.4.1. Static vs dynamic loading in cavitation

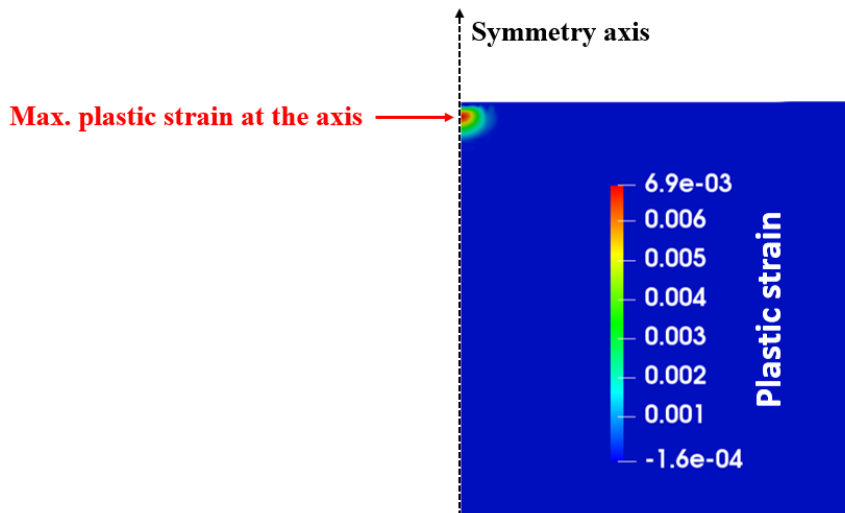


Figure 6.11. Contour of plastic strain in the material for static simulation, simulated using FEM with pressure as boundary condition (pressure obtained from the interface pressure in SPH simulation at 500 time steps).

In order to setup a static case in FEM using the same load as experienced by the material in the FSI simulation, we use the load data between the time when the shock wave hits the solid material as shown in figure 6.7c (where the shock wave just reached the interface at its left end, let's call this instance T1) to when the shock wave travels along the interface and reaches the right end of the interface, let's call this instance T2. Between these times T1 and T2, we capture the pressure along the interface in the fluid from SPH simulation reported in figure 6.7, for 500 intermediary steps. Thereafter, the FEM solver [79] is used to setup a solid simulation with, as a boundary condition, the pressure data obtained at 500 time steps from the FSI SPH simulation. The minimum mesh size is set as  $5 \mu\text{m}$  (using a QUA8 mesh type) and 5920 cells are used for the FEM simulation. The material properties are set the same as in the SPH simulation with  $\alpha = 0$  which refers to no strain rate effect. The FEM solver solves the material for each of the 500 steps one after the other. The plastic strain is accumulated in the material for all the 500 steps to obtain a static response of the material for the same load as the solid experiences during the SPH simulation. Figure 6.11 shows the response of the solid when subjected to a static loading simulated using FEM. Contours of plastic strain show that the static response does not have an offset  $R_{\text{max}}$  for the maximum plastic strain which occurs at the symmetry axis. This result would suggest that the reason for the offset of maximum plastic strain as shown in figure 6.7d is the dynamic loading. A dynamic simulation differs from a static one in terms of the rate of loading. A very fast rate of loading (dynamic simulation) would not allow sufficient time for the material to respond to the load because of inertial effects which are dealt with in the next section.

#### **6.4.4.2. Inertial effects on material response**

To understand the inertial effects on material response, we now look at the dynamics of the shock wave produced by the bubble collapse when it interacts with the fluid-solid interface. Figure 6.12 shows the shock wave interaction at the interface. The contours are taken from the SPH FSI simulation for detached cavity with  $\text{SR} = 1.33$  as previously presented in figure 6.7. Contours of pressure are plotted in the fluid and plastic strain in the solid at a certain time during the simulation after the shock wave has hit the interface. A primary shock wave can be observed in the fluid which is generated by the bubble collapse. Once this shock wave reaches the interface, a part of the shock is reflected back in the fluid which is marked as a reflected shock wave in figure 6.12. The point of intersection of the primary and reflected shock wave corresponds to the maximum pressure along the interface as seen in the contours in figure 6.12.

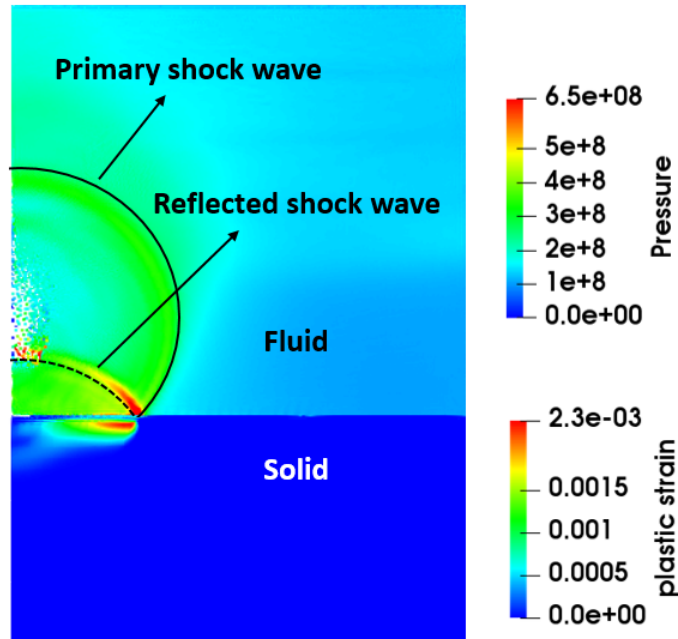


Figure 6.12. Contours of pressure in the fluid and plastic strain in the solid, shows the primary shock wave (generated by the bubble collapse) and a reflected shock wave (generated by the reflection of primary shock wave at the interface).

In order to understand the phenomenon better, a schematic is presented in figure 6.13, demonstrating the shock wave evolution wrt time. Consider a spherical shock wave generated in the fluid at  $T=0$  as marked in the figure 6.13 ( $T$  corresponds to a fictitious time used to exhibit the time evolution of the shock wave). The red dot corresponds to the point where the shock wave initiates, supposed to be at an axial distance  $\alpha_z$  from the interface. The shock wave then travels spherically outwards from the point of shock generation. At time  $T=3$ , the shock just reaches the interface. At  $T=4$ , along with the primary shock wave, a reflected shock wave is observed as the primary shock wave gets reflected from the interface. The point of intersection of the primary and reflected shock waves is marked as A, B & C corresponding to the time  $T=4$ ,  $T=5$  &  $T=6$  respectively. These points correspond to the location of the maximum pressure along the interface at a given time as shown in figure 6.9. We will refer to this point where the primary and reflected shock wave intersect as the '*shock front*' from now on in the article. Consider an SPH particle right below point A. This solid particle would respond to the pressure it experiences from the fluid and deform accordingly. If the *shock front* moves really quickly, the material might not have enough time to react to the load and deform as much as it would have had for the same magnitude of pressure under a static load. It is then of primary importance to compute the speed of the shock wave along the interface.

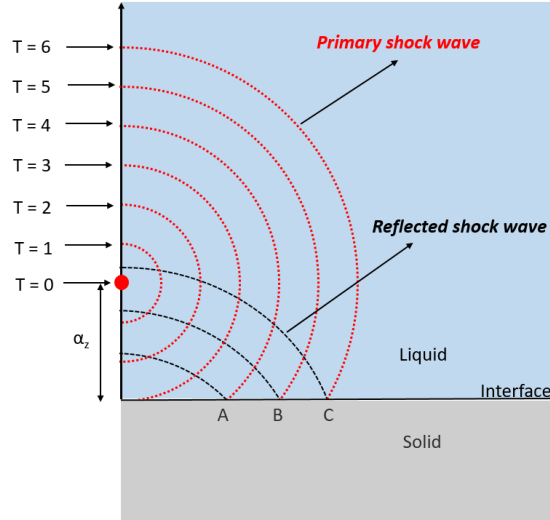


Figure 6.13. Schematic of time evolution of the primary shock wave and the reflected shock wave (times  $T=0$  to  $T=6$  correspond to fictitious time separated by a constant time interval, used to exhibit the position of the wave wrt time).

The equation of the primary shock wave (as shown in schematic in figure 6.13) in an  $r$ - $z$  plane can be represented by a circle and is given by,

$$r^2 + (z - \alpha_z)^2 = R(t)^2 \quad (6.19)$$

$$v_{SW} = c_l \sqrt{1 + \left(\frac{\alpha_z}{r}\right)^2} \quad (6.20)$$

where  $R(t)$  is the radius of the primary shock wave as a function of time. It can be written as  $R(t) = \int u(t)dt$ ,  $u(t)$  is the radial velocity of the primary shock wave as a function of time,  $r$  is the radial position and  $z$  is the axial position of the wave front. Substituting  $z = 0$  in equation 6.19 would give the position of the *shock front* (for example point A, B or C in figure 6.13) wrt time along the interface, the derivative of the radial position gives the velocity of the shock wave along the interface ( $v_{SW}$ ) given by equation 6.20. To obtain an analytical solution, we substitute  $c_l = 1500$  m/s (speed of sound in water) and  $\alpha_z = 0.09$  mm, which corresponds to the position where the micro jet hits the bubble surface for the detached cavity case with  $SR = 1.33$ . The solution of equation 6.19 & the equation 6.20) gives the position and velocity of the *shock front* wrt time. Figure 6.14 shows the plot of the theoretical velocity of the *shock front* wrt to the radial distance from the axis (legend marked as SW Intersection Velocity Analytical). The velocity of the *shock front* is high close to the symmetry axis and goes down till it reaches the speed of the shock wave itself, which is here set as 1500 m/s. The high velocity near the symmetry axis is due to the spherical shock front hitting a flat surface. As a result, the rate of

loading and unloading is also high close to the symmetry axis, which does not allow the material sufficient time to respond to the load, hence exhibiting lower plastic strain near the symmetry axis even though the pressure acting on the material is the highest at the symmetry axis.

To sum up the argument, we have plotted the pressure and the velocity corresponding to the *shock front* wrt to the radial distance from the axis in figure 6.14 as obtained from SPH simulations. The computed velocity of the *shock front* obtained from SPH compares well with the analytical solution. The difference in values could be due to the fact that the shock wave velocity is considered as a constant (1500 m/s) for the analytical solution, whereas it actually depends on the pressure difference between the shock front and rear. The background contour (plastic strain) on the graph is set to scale with the  $x$ -axis of the graph which corresponds to the distance along the interface. It can be clearly seen that the pressure at the *shock front* (which is also the maximum pressure for a given instance) is maximum at the symmetry axis and decreases as we move along the interface. Moreover, the point at which the pressure decreases below the material yield stress (508 MPa) also corresponds well to the end of the plastic zone. Clearly, the background contour demonstrates that the maximum plastic strain occurs not at the point of maximum pressure but at an offset somewhere between 0.1 mm to 0.2 mm from the symmetry axis along the interface.

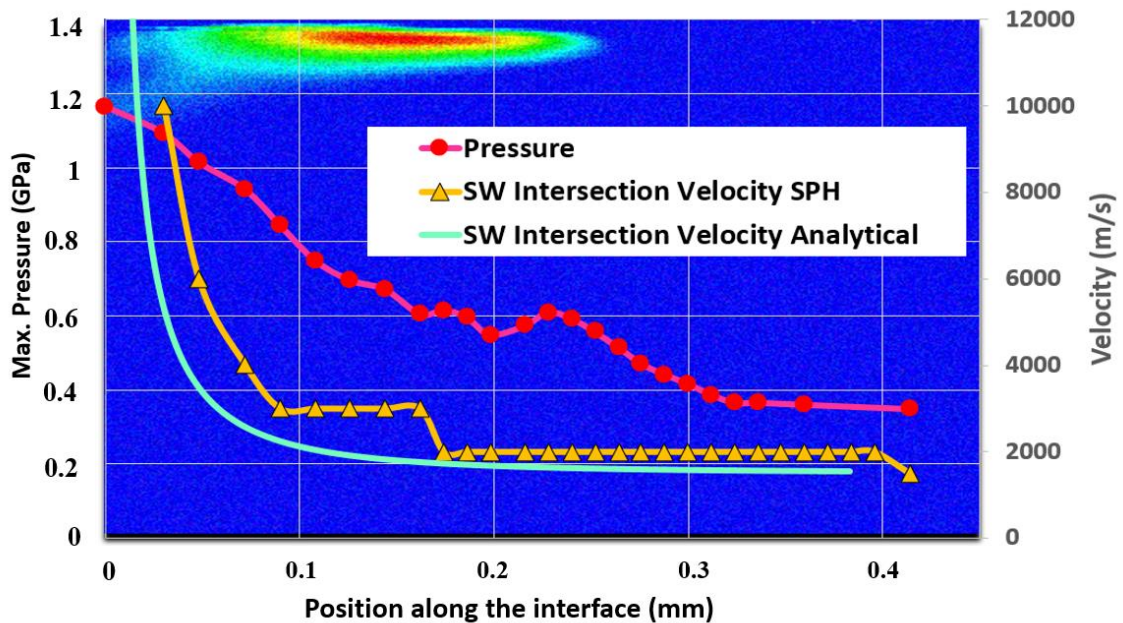


Figure 6.14. Plot for the velocity of the shock front (right axis) wrt its position along the interface obtained from both the SPH simulation and analytical expressions (equation 6.19). The plot also shows the pressure of the point of intersection (left axis) wrt its position along the interface obtained

from SPH simulation The background contours are for plastic strain in the solid and are set to scale with the x-axis.

#### 6.4.5. Effective Pressure

A physical explanation was given in the last section that demonstrates why the plastic deformation occurs at a radial offset. However, it would be interesting to understand the phenomenon from a quantitative perspective. Moreover, in this section we aim at providing a criterion that could predict the zone where plasticity will occur based on quantities available in classic CFD calculations, namely pressure and velocity in the fluid. We define a new variable named effective pressure as given below,

$$P_{effective} = \frac{(P - \sigma_{Y0})}{\rho(v_{sw} - c_l)^2} \quad (6.21)$$

where P is the pressure at the interface where the effective pressure is being calculated,  $\sigma_{Y0}$  is the initial Yield stress for the material (508 MPa in the present simulation),  $\rho$  is the density of the solid,  $v_{sw}$  is the velocity of the *shock front* along the interface at the point where the effective pressure is calculated and  $c_l$  is the speed of sound in the liquid. The effective pressure is a non-dimensional parameter that should indicate the pressure that effectively leads to plastic strain in the solid. The numerator gives the excess pressure above the Yield stress, as only the load above the Yield stress could lead to plasticity. The denominator takes into account the inertial effects due to the density of the solid and the excess velocity of the *shock front* above the sound speed of liquid. The excess velocity is the shock front velocity ( $v_{sw}$ ) minus the speed of sound in liquid ( $c_l$ ). The term  $(v_{sw} - c_l)$  makes sure that if the velocity of *shock front* along the interface is much higher than the sound speed, the effective pressure acting on the material (due to inertial effects) is reduced via the term  $\rho(v_{sw} - c_l)^2$ . The density term in the denominator plays an important role since the phenomenon is linked to the inertial effects in the material, however for the present simulation the density effects can be neglected as we simulate the same material for different cases.

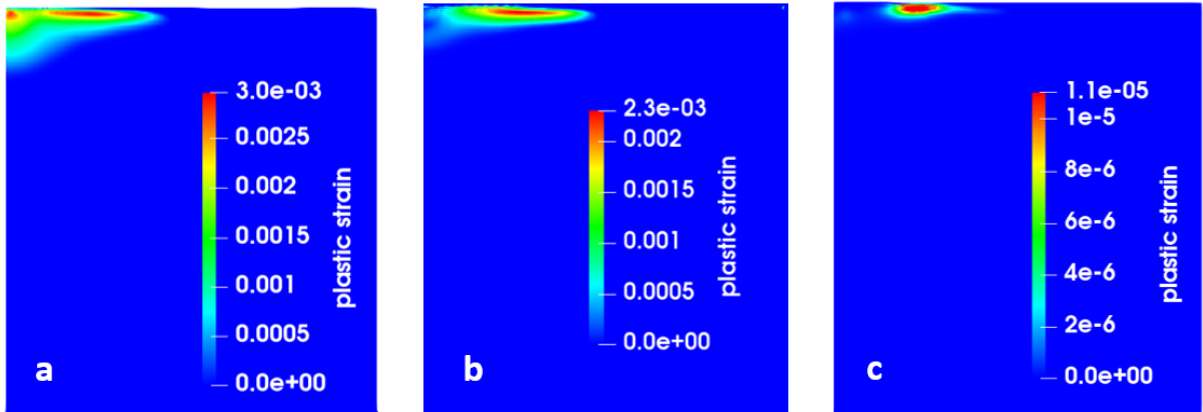


Figure 6.15. Contours of plastic strain for 50 MPa driving pressure and 0.15 mm bubble radius for (a) Stand-off ratio  $SR = 1.2$ , (b) stand-off ratio  $SR = 1.33$  & (c) stand-off ratio  $SR = 1.5$ .

We present three cases with different stand-off ratios (1.2, 1.33 & 1.5). The contours of plastic strain are shown in fig 6.15 a-c. It can be observed that the three cases produce distinctly different patterns of plastic strain. The effective pressure given by equation 6.20 will be used for all the three cases to check whether the effective pressure can qualitatively match the plastic strain in the solid, thus giving us a parameter (effective pressure) that can be used in fluid simulations to indicate the erosion prone areas better while considering the inertial effects.

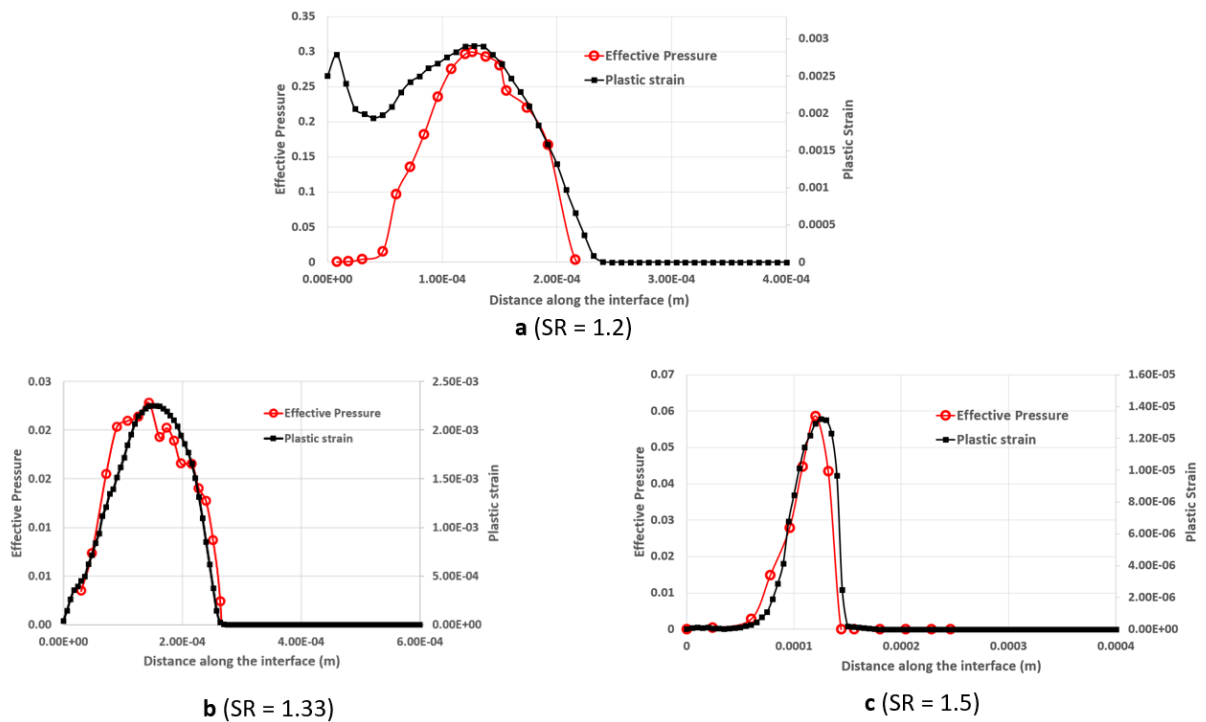


Figure 6.16. Plot of plastic strain and effective pressure for (a) Stand-off ratio 1.2, (b) stand-off ratio 1.33 & (c) stand-off ratio 1.5 for 50 MPa driving pressure and 0.15 mm bubble radius.

Plastic strain in the material (plotted along a line parallel to the interface in the material passing through the maximum plastic strain position) and effective pressure at the interface are plotted for all three cases (shown in fig 6.15) in fig 6.16 a-c. It can be observed that effective pressure defined by equation 6.20 qualitatively matches well with plastic strain in the material for  $SR = 1.33$  &  $1.5$ . However, for  $SR = 1.2$ , the plastic strain does not match equally well with effective pressure close to the symmetry axis. The contour in fig 6.15(a) for  $SR = 1.2$  shows a maximum plastic strain at an offset which is due to the inertial effects as explained earlier. However, close to the symmetry axis a tiny zone of relatively high plastic deformation can also be observed, which is actually due to the impact of the micro jet. The effective pressure definition (equation 6.20) being based on the assumption that all energy that reaches the interface is via the shock wave impact, it is difficult to predict the plastic strain developed near the symmetry axis for  $SR = 1.2$  that is due to the micro jet impact. The lower the stand-off ratio, the higher the dynamic pressure experienced by the interface would be. Hence the effective pressure definition can be used to predict plastic strain when the stand-off ratio is sufficiently large ( $SR > 1.3$ ). For lower stand-off ratios, the plastic strain close to the symmetry axis is under predicted by effective pressure and an alternative approach should be proposed that is the aim of the next section.

#### 6.4.6. Characteristic response time

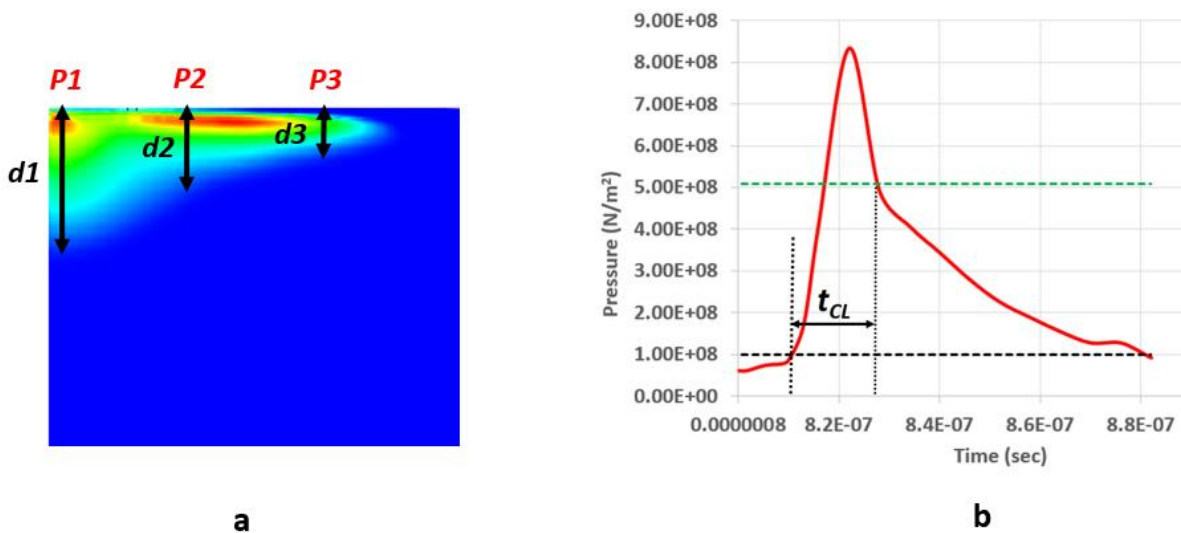


Figure 6.17. (a) Contour of plastic strain showing depth of plastic strain zone at different point on the interface. The material characteristic time is defined as the depth of the plastic strain divided by the speed of sound in the solid, e.g. material characteristic time at point P1 can be calculated as  $d1/c_s$  (where  $c_s$  is the sound speed in the solid), (b) shows a typical pressure vs time curve for a certain point

on the interface, to estimate the loading characteristic time we consider the time from when the pressure is above 100 MPa till it drops down to 508 MPa (initial yield stress).

An alternative approach to quantitatively analyse the material behaviour is presented in this section. We focus on two quantities: material characteristic time (or characteristic response time) and loading characteristic time. We use the definition of material characteristic time as mentioned in Roy *et al.* [69], which is given by the depth of the plastic zone divided by the speed of sound in solid and which signifies the amount of time required for the material to react to a load. Figure 6.17a shows the depth of the plastic zone at various points along the interface from which the material characteristic time was computed. On the other hand, the loading characteristic time for a point at the interface is defined as the time during which the pressure at that point first rises above 100 MPa (black dashed horizontal line in figure 6.17b) and finally drops down below 508 MPa (initial yield stress for the material marked as green dashed line in figure 6.17b). If the material characteristic time is greater than the loading characteristic time, the material behaviour would be dominated by the inertial effects.

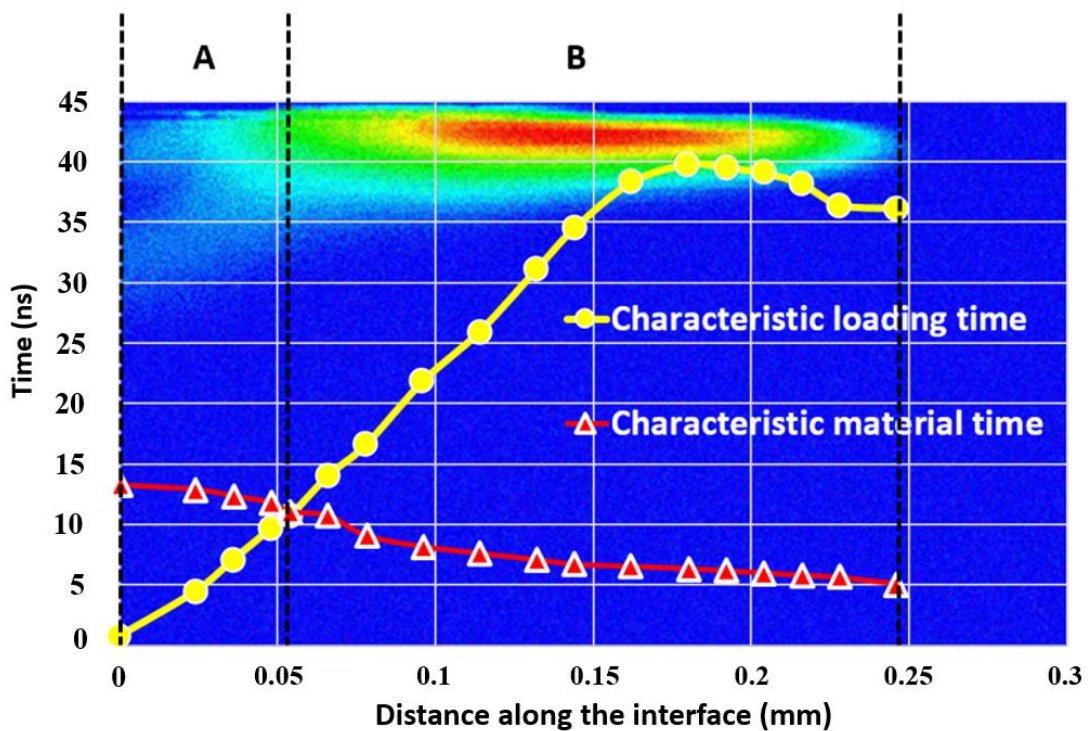


Figure 6.18. Plot shows material characteristic time and loading characteristic time along the interface for  $SR = 1.33$ , plot background image is the contours of plastic strain for  $SR = 1.33$ .

Figure 6.18 shows the plot of both material characteristic time and loading characteristic time along the interface for  $SR = 1.33$ , the contours of plastic strain are set as the background in the plot. It can be observed that for the region close to the symmetry axis where the material

exhibits relatively low plastic deformation (region marked as A in the figure), the loading characteristic time is lower than the material characteristic time and for region B where the material characteristic time is lower than the loading characteristic time, the material has time to deform under the load and hence exhibits relatively higher plastic deformation

For the case of  $SR = 1.2$ , where the effective pressure fails to capture the plastic zone close to the symmetry axis, it would be interesting to see whether characteristic time plot can capture it better. Figure 6.19 shows the characteristic time plots for  $SR = 1.2$ . It can be observed that in region A where the plastic strain is relatively high, the material characteristic time is lower than the loading characteristic time thus predicting well the effect of inertia and dynamic pressure. As we move further along the interface into region B, the material characteristic time becomes marginally larger than the loading characteristic time, thus leading to a slightly lower plastic strain zone as the inertial effects come into play. Further, in region C the material characteristic time is much lower than the loading characteristic time thus the material exhibits higher strain rate since the inertial effects are not dominant. Thus, characteristic time analysis can be used to predict plastic strain zone in the material. However, the definition of the material characteristic time used in this study requires knowing the plastic strain depth and hence cannot be estimated from an only fluid simulation.

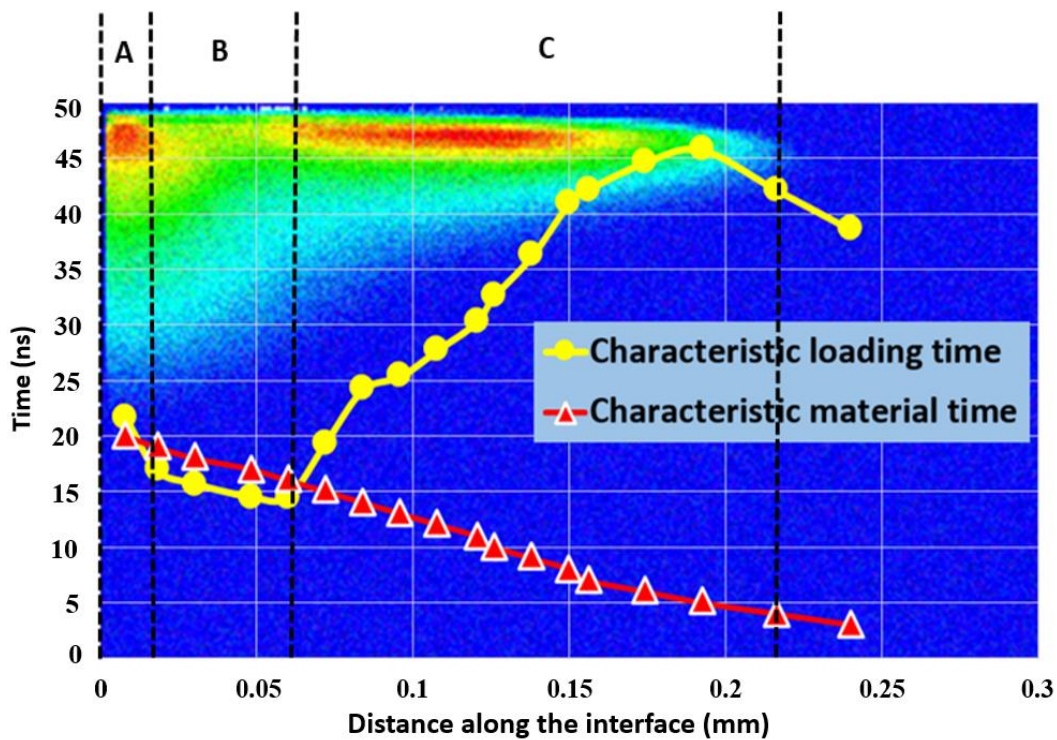


Figure 6.19. Plot shows material characteristic time and loading characteristic time along the interface for  $SR = 1.2$ . Background image is the contours of plastic strain for  $SR = 1.2$ .

## 6.5. Conclusions and future work

An axisymmetric SPH FSI solver has been developed, which is capable of computing the collapse of a single bubble over an elastic-plastic solid following Johnson-Cook yield criterion. The fluid solver was validated against the analytical solution of the Rayleigh-Plesset equation and the solid solver against an FEM solver for an indentation case.

Simulations of the collapse of a detached and an attached cavity suggest that the micro jet generated during the collapse of an attached cavity has an ability to cause a larger maximum plastic strain in the material as compared to the shock wave generated during the collapse of a detached cavity. It is observed that for the same magnitude of pressure wave initiating the collapse and the same size of the bubble, the micro jet can produce twice the maximum plastic deformation compared to a shock wave. Hence, in case of repeated collapse, a micro jet dominated impact would exhibit a smaller incubation time compared to the detached cavity. On the other hand, the volume of material that is plastically deformed in case of a micro jet is miniscule compared to a shock wave impact (almost 800 times smaller). This would imply that, even though the incubation time for material erosion might be lower for a micro jet collapse, the shock wave can plastify a much larger volume of material and hence the erosion rate should be higher for a shock wave impact. Hence it could be inferred that the material erosion ability of a shock wave dominated collapse is much higher than that of a micro jet dominated collapse.

An important aspect of cavitation loading is the high strain rate associated to the phenomenon. The present results show that the strain rate effects can significantly affect plastic deformation in the solid since non-strain rate sensitive simulations produce around 61% higher plastic deformation for a detached cavity compared to a strain rate sensitive model in the case of stainless steel A2205.

An important and novel finding in the present article is the response of the material for a detached cavity. It is shown that the maximum plastic deformation does not occur at the center of collapse but at an offset from the center (cf. figure 6.7d). Even though the pressure experienced by the material is the highest at the center, it does not produce the maximum plastic deformation there. This phenomenon is due to inertial effects, since the material tends not to respond to the load as the rate of loading and unloading is extremely high. The effect is linked to the high velocity of shock front along the interface close to the symmetry axis. The study clearly demonstrates that maximum pressure does not always correspond to the location of maximum plastic deformation.

A new parameter called effective pressure is defined in the article which matches well with the plastic strain in the material. for a standoff ratio  $SR=1.33$ . Such a parameter can easily be used in CFD calculation to predict the location where plasticity will be localized. It is found that the effective pressure can also predict the location of the plastic zone for a higher standoff ratio  $SR=1.5$ . However, the definition of effective pressure is based on the shock wave impacting the solid and hence is only valid for large stand-off ratios where plasticity is governed by wave propagation only. For lower stand-off ratios the effective pressure under predicts the plastic strain near the symmetry axis which is due to the impact of the micro jet and not due to the shock wave.

Another approach to quantifying material response while considering inertial effects is then proposed based on a characteristic time analysis. The material characteristic time and the loading characteristic time are compared for two cases ( $SR = 1.2$  &  $1.33$ ), where a lower material characteristic time relative to the loading characteristic time signifies more dominant inertial effects and hence relatively lower plastic strain. It is found that the characteristic time analysis predicts the zones of plastic deformation quite well. However, the definition of material characteristic time is such that it cannot be known without solving for the solid.

## Chapter Highlights

- FSI simulation validations are presented and one simulation each for an attached and detached cavity are carried out for a stainless steel specimen (A-2205).
- Different plastic deformation mechanisms for detached and attached cavity are demonstrated. It is shown that detached cavities have higher damage ability compared to attached cavities for the same bubble radius and driving pressure.
- Detached cavities show a unique plastic deformation behaviour where the maximum plastic strain does not occur at the symmetry axis but at an offset. The detailed study shows that it is caused by inertial effects where rate of loading and unloading are so high close to the symmetry axis that the material does not have time to react to the load.
- A new quantity named effective pressure has been formulated which matches well with plastic strain obtained from the FSI simulation in the case of plasticity induced by shock waves, i.e. for large standoff ratio  $SR > 1.3$ .
- Effective pressure can be used in CFD calculation to estimate erosion prone areas in solids in case of large standoff ratio.
- The characteristic time analysis presented in the chapter shows that it can be used to precisely predict plastic deformation in the material for any standoff ratio.



# 7 FLUID STRUCTURE INTERACTION

## PARAMETRIC STUDY

This chapter is constructed as the following paper which is planned to be submitted to the journal WEAR. The paper has been used as it is in the chapter, hence there could be a repetition of text, figures or tables as in the last chapters (1-6).

### **Cavitation material erosion: Focus on plastic strain energy absorption for different bubble size, stand-off distance, driving pressure & strain rate**

Shrey Joshi<sup>1,2</sup>, Jean Pierre Franc<sup>2</sup>, Giovanni Ghigliotti<sup>2</sup>, Marc Fivel<sup>1</sup>

<sup>1</sup>*Univ. Grenoble Alpes, CNRS, Grenoble INP, SIMaP, 38000 Grenoble, France*

<sup>2</sup>*Univ. Grenoble Alpes, CNRS, Grenoble INP, LEGI, 38000 Grenoble, France*

A meshless Smoothed Particle Hydrodynamics solver is used to simulate the collapse of a cavitation bubble near a solid taking into account the fluid structure interaction. A parametric study has been performed to study the effect of stand-off ratio, bubble size, driving pressure and strain rate on material response. We focus on plastic strain magnitude and plastic strain energy absorption to compare different cases and their ability to cause material erosion. Findings indicate that, in the case of repeated collapses, cavities attached to the solid should have an ability to initiate damage quicker but would exhibit lower erosion rate compared to the cavities detached from the solid. Bubble size has a weak effect on the time required to initiate damage but erosion rate has a strong dependence on bubble size, where larger bubbles would exhibit larger erosion rate. Strain rate insensitive simulations show a significantly larger plastic strain compared to the strain rate sensitive case, which suggests that using an appropriate plasticity model that includes strain-rate sensitivity is important while studying the phenomenon of cavitation.

**Keywords:** Cavitation erosion, fluid structure interaction, plastic strain energy absorption, strain rate effects, stand-off distance

## 7.1. Introduction

To understand the phenomenon of cavitation and the resulting material response has been the unified aim of cavitation research. Capturing of bubble dynamics and measurement of wall pressure due to a collapse still remains a challenge due to the small scale of the phenomenon and the fast dynamics. To assist experimental findings and to understand the phenomenon better, advances have been made in numerical studies of cavitation during the last decades. Most of them have vastly focused on bubble dynamics, to understand the cavitation bubble collapse. However, more work is required in order to get a thorough understanding of material response induced by collapsing bubbles. For instance, most numerical CFD studies estimate cavitation erosion-prone areas using either peak pressures or Cavitation Aggressiveness Index (CAI) [8-10]. However, there have been a number of proposed CAI in the literature which work in one case but not the other and hence there is a need to understand the material response at the fundamental level of a single bubble collapse in order to better predict cavitation erosion damage.

There has been recently a push towards modelling cavitation erosion using fluid structure interaction solvers [11, 13]. A thorough numerical study of cavitation that can provide a holistic understanding, ideally requires a two-way fluid structure interaction coupling to get realistic results. Earlier studies [11, 13] have simplified the material behaviour by using linear isotropic hardening models which cannot capture the non-linear hardening effects. Also, they generally do not consider strain rate hardening effects which can be significant for a phenomenon like cavitation that involves fast dynamics. Past studies have pointed out that, for a material following isotropic hardening, the most probable mechanism of plasticity accumulation for consecutive impact loads is the strain rate effect [85]. In order to gain a better understanding of the mechanisms involved, we developed a cavitation Fluid structure interaction solver capable of solving a single bubble collapse in the fluid and the associated solid response, taking into account non-linear hardening and strain-rate hardening effects.

The SPH FSI solver is developed using an existing 2D open source fluid SPH code SPHYSICS which is used as a basis to develop the solver further [16]. The 2D fluid solver is modified to 2D axisymmetric and the axisymmetric solid solver is developed in-house. However, axisymmetric SPH solvers suffer from an inconsistent definition of density near the symmetry

axis. A new method to mathematically resolve this issue for the axisymmetric solid SPH solver is used in the present study (section 5.3.2). The axisymmetric fluid and solid solvers were validated against Rayleigh-Plesset collapse and FEM simulations respectively (section 6.3). The two solvers are eventually coupled together to obtain a fully coupled FSI solver capable of solving single bubble collapse over a solid medium to obtain elastic-plastic response using the Johnson-Cook hardening model [19]. This paper presents a detailed parametric study on the effect of different bubble size, bubble stand-off distance and driving pressure on the material response. The analysis is based on energy calculations. Finally, the effect of strain rate hardening on the material response is also presented.

## 7.2. Simulation cases and description

In this section, we describe the simulation domain and the parameters used for the simulations. The fluid bubble collapse and the solid response are solved using SPH (details regarding the methodology are given in section 6.2). The fluid is treated as weakly compressible and compressibility effects are modelled using the Tait equation of state given by the following,

$$P = B_1 \left[ \left( \frac{\rho}{\rho_0} \right)^\gamma - 1 \right] \quad (7.1)$$

where  $\gamma = 7$  and  $B_1 = c_0^2 \rho_0 / \gamma$ ,  $\rho_0 = 1000 \text{ kg m}^{-3}$  is the reference density and  $c_0$  is the sound speed at the reference density.

The solid behaviour is simulated using the Johnson-Cook model which gives the Yield stress by the following expression,

$$\sigma_y(\varepsilon_p, \dot{\varepsilon}_p) = [A_0 + B_0(\varepsilon_p)^n] [1 + C_0 \ln(\dot{\varepsilon}_p^*)] \quad (7.2)$$

where,  $A_0$ ,  $B_0$ ,  $C_0$ ,  $n$  are material constants,  $\dot{\varepsilon}_p^* = \frac{\dot{\varepsilon}_p}{\dot{\varepsilon}_{p0}}$  (the non-dimensional effective plastic strain rate) where  $\dot{\varepsilon}_{p0}$  is the reference plastic strain-rate of the quasi-static test used to determine the yield stress and hardening parameters  $A_0$ ,  $B_0$  and  $n$ .

### 7.2.1. Simulation domain and cases

We simulate fluid structure interaction for single bubble collapse for different bubble sizes, standoff ratios (where the standoff ratio (SR) is defined as  $D/R$ ,  $D$  is the distance from the bubble center to the interface and  $R$  is the radius of the bubble) and driving pressures in 2D

axisymmetric. Figure 7.1 shows a typical simulation domain for single bubble collapse simulations. The  $z$ -axis is the symmetry axis and the  $r$  axis is along the fluid-solid interface. The part of the domain above the interface is the fluid where a cavitation bubble is placed and the part of the domain below the interface is the solid which would simulate an elastic-plastic response due to the bubble collapse. It should be noted that the cavitation bubble in the present study is not simulated as a vapour bubble but as a vacuum bubble, this means that the internal pressure of the bubble is 0 at all times during the simulation.

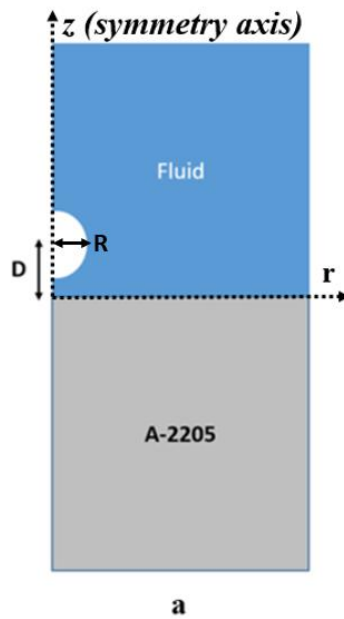


Figure 7.1. Sketch of the initial simulation domain for axisymmetric SPH FSI simulation (Standoff ratio  $SR$  is defined as  $D/R$ ).

To initiate a collapse, a pressure wave is generated at the top of the fluid domain. The magnitude of the pressure wave can be varied and three different driving pressures were used in the present work (25 MPa, 50 MPa and 75 MPa). The distance  $D$  of the bubble center from the interface is varied to produce different cases with varying stand-off ratio ( $SR = D/R = 1.66, 1.33, 1.0, 0.66 \text{ \& } 0.33$ ), where  $SR$  less than or equal to 1 is an attached cavity and  $SR$  greater than 1 is a detached cavity. In order to vary the bubble size, we keep the number of particles along the bubble radius as a constant. Hence, increasing bubble size would mean increasing the initial distance  $\Delta x$  between two adjacent particles by the same factor. Also the size of the domain scales with the radius of the bubble, e.g. a bubble of twice the radius is simulated using a domain that is scaled by a factor of 2, both in the  $r$  and  $z$  directions. Since both  $\Delta x$  and the domain size are scaled by the same factor as the bubble radius, the number of particles in the simulation is kept constant. We use three different bubble sizes (0.1 mm, 0.15 mm & 0.2 mm)

to run a parametric study on the effect of bubble size on the material response. The number of particles used for the simulation varies marginally from 320890 to 342680. The range comes from the fact that a different standoff distance can lead to a different number of particles for the same bubble size and initial particle spacing  $\Delta x$ .

### 7.2.2. Fluid and material parameters

The fluid and material parameters for the present simulations have been listed in table 6.1.

*Table 7.1. Table showing parameters for the fluid and solid used in the FSI simulations.*

<b>Parameter</b>	<b>Fluid (Water)</b>	<b>Solid (A-2205)</b>
<b>Density</b> (kg/m <sup>3</sup> )	1000	7800
<b>Sound speed</b> (m/s)	1500	4883.33
<b><math>\alpha</math></b> (in equation 6.9)	1	1
<b><math>\beta</math></b> (in equation 6.9)	2	2
<b>Young's Modulus</b>	-	186 GPa
<b>Poisson ratio</b>	-	0.3
<b><math>A_0</math></b> (in equation 7.2)	-	508 MPa
<b><math>B_0</math></b> (in equation 7.2)	-	832 MPa
<b><math>C_0</math></b> (in equation 7.2)	-	0.031
<b><math>n</math></b> (in equation 7.2)	-	0.29
<b><math>\dot{\epsilon}_{p0}</math></b> (in equation 6.15)	-	0.05 s <sup>-1</sup>

### 7.3. Results and discussion

Although this study only presents results for a single bubble collapse, some qualitative results can be deduced in the case of repeated bubble collapses. In order to do so we consider two important quantities related to material erosion: incubation time (marked as A in figure 7.2) and erosion rate. Figure 7.2 shows a typical mass loss curve for a material exposed to cavitation. Incubation time is the exposure time required by the material to initiate erosion and indicates how quickly a material under cavitation load will start to erode. On the other hand, erosion rate would indicate the rate of material removal after the incubation has been reached. Both the quantities together can provide a good measure of erosion ability under repeated cavitation loads.

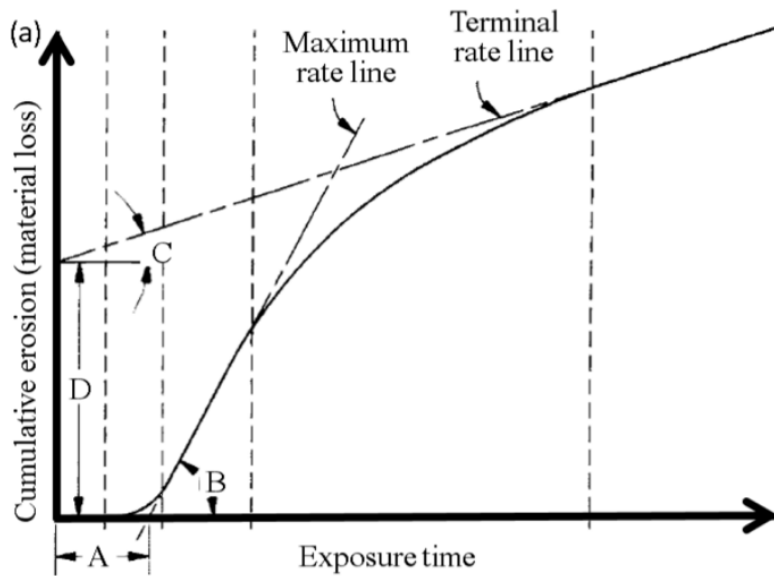


Figure 7.2. Characteristics of typical cumulative erosion versus exposure time curve. A = nominal incubation time; (B) = maximum erosion rate; (C) = terminal erosion rate; and D = terminal line intercept [69].

Let us consider that the energy absorbed by the material after a single impact is  $W$ . It could reasonably be expected that the absorbed energy is of the order of  $n.W$  after  $n$  impacts. It could be argued that the volume loss ( $VL$ ) would be of the order of  $VL = n.W/K$  (where  $K$  is the material fracture toughness, which indicates the amount of energy absorbed per unit volume until fracture). Therefore, the erosion rate ( $ER$  i.e. volume loss per impact) would be  $ER = VL/n = W/K$ . Since material toughness ( $K$ ) is a constant for a material, the energy absorbed by the material after a single impact could be considered as an indicator of the erosion rate for multiple impacts. The higher the absorbed energy, the higher the erosion rate.

For incubation time estimation, let us consider that the volume of the plastic deformed zone for a single impact is  $V$ , we assume that it still remains of the order of  $V$  for consecutive impacts. Moreover, it could be assumed that the incubation time corresponds roughly to the critical number of impacts  $nc$  required to reach fracture toughness in that volume  $V$ . The energy absorbed by the material would then be  $V.K$ . Since it is also  $nc.W$ , we have  $V.K = nc.W$  so that the incubation time (or more precisely the critical number of impacts) would be  $nc = K/(W/V)$ . This would suggest that the incubation time  $nc$  would vary as the inverse of the absorbed energy density  $W/V$ . Hence higher the absorbed energy density, lower the incubation time.

In the absence of computational results on repeated cavitation bubble collapse, it can then be assumed that the energy absorbed by the material after a single bubble collapse and the corresponding absorbed energy density are, in a first approximation, relevant indicators of the erosion rate and incubation time respectively.

In order to calculate the total absorbed energy, the area under the stress strain curve for each particle is calculated and then multiplied by the volume occupied by that particle to obtain energy absorbed by one particle. This quantity is summed up for all particles to obtain the total energy absorbed by the solid. To obtain the absorbed energy density, the total absorbed energy is divide by the volume of the plastic strain zone. The volume of the plastic strain zone is obtain by adding the volume occupied by each particle that has undergone plastic deformation.

### **7.3.1. Effect of stand-off ratio**

To understand the effect of stand-off ratio, we vary stand-off ratio while keeping the bubble size at 0.15 mm and driving pressure constant at 50 MPa. Material response for seven different stand-off ratios are presented in this section:  $SR = 1.66, 1.5, 1.33, 1.2, 1.0, 0.66 \text{ \& } 0.33$ . A stand-off ratio of more than 1 corresponds to a detached cavity (when bubble surface does not touch the solid) and stand-off ratio less than and equal to 1 corresponds to attached cavity (when bubble surface touch the solid). Figure 7.3 shows contours of plastic strain in the material for all the seven cases, figure 7.3d-g shows plastic strain contours for detached cavities ( $SR = 1.2, 1.33, 1.5 \text{ \& } 1.66$  respectively) and figure 7.3 a-c are magnified contours (magnified over the white dashed rectangle in figure 7.3g) for attached cavity ( $SR = 0.33, 0.66 \text{ \& } 1.0$  respectively). The reason that the contours for attached cavities are magnified is because the attached cavity produces a very tiny zone of plastic deformation compared to the detached cavities which would not be clearly noticeable in a non-magnified contour.

Attached cavities produce two distinct zones of plastic deformation: a primary plastic deformation zone very close to the symmetry axis and a secondary plastic deformation zone away from the symmetry axis (section 6.4.1). A detailed description of plasticity evolution in the case of an attached cavity was presented in section 6.4.1. It was suggested that the primary plastic zone is a consequence of the micro jet hitting the solid plus the wave originating from the toroid bubble collapse occurring on the side. The secondary plasticity zone is only due to the shock wave from the toroid collapse. It can be clearly observed that for attached cavities the highest maximum plastic strain occurs for  $SR = 1.0$ . It is because the micro jet will gain higher speed for a high stand-off ratio in case of an attached cavity and a higher speed of micro

jet would lead to a higher pressure acting on the solid. However, while comparing  $SR = 0.66$  and  $SR = 0.33$ , it would be expected that  $SR = 0.66$  should produce higher maximum plastic strain as it would have a higher micro jet velocity, but an opposite trend is observed. The trend reverses because the plastic strain at the center is not just due to the micro jet but also to the shock wave from the toroid collapse. From the secondary plastic strain zone, it can be observed that the toroid collapse point for  $SR = 0.33$  is closer to the center compared to  $SR = 0.66$ . Hence the shock wave from the toroid collapse produces a higher plastic strain at the center for  $SR = 0.33$  compared to  $SR = 0.66$ . So even though the micro jet should produce a higher plastic strain at the center for  $SR = 0.66$ , the higher additional plastic strain due to the toroid collapse supersedes the effect, leading to a higher plastic strain in the material for  $SR = 0.33$ .

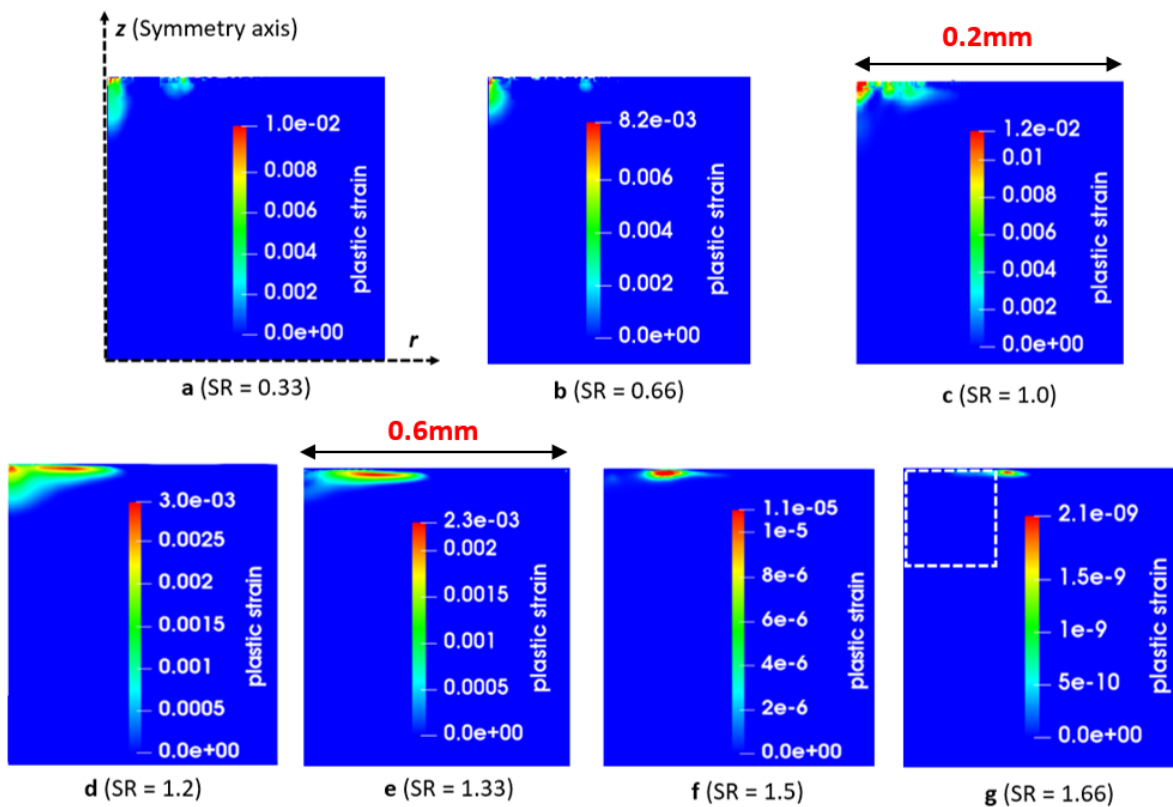


Figure 7.3. Plastic strain contours for a bubble radius  $R = 0.15$  mm, driving pressure  $P = 50$  MPa and for different stand-off ratios for (a)  $SR = 0.33$ , (b)  $SR = 0.66$ , (c)  $SR = 1.0$ , (d)  $SR = 1.2$ , (e)  $SR = 1.33$ , (f)  $SR = 1.5$ , (g)  $SR = 1.66$  (the contours in figure 7.3 a, b & c are magnified on the white dashed rectangle in figure 7.3g). The scale of the contours 7.3 a-c is marked in fig 7.3c and for 7.3 d-e is marked in fig 7.3e.

For a detached cavity, the plastic strain is only due to the shock wave impact. It is clear that the higher the stand-off ratio, the lower the shock wave pressure becomes by the time it reaches the interface, hence producing lower plastic deformation. This is observed from the maximum

plastic strain for  $SR = 1.2, 1.33, 1.5 \text{ \& } 1.66$ , where the lower the stand-off ratio, the higher the maximum plastic strain. For detached cavity simulations, the maximum plastic strain does not occur at the symmetry axis but at an offset from the symmetry axis especially for higher stand-off ratios ( $SR = 1.33, 1.5 \text{ \& } 1.66$ ). The phenomenon has been dealt with in detail in section 6.4.4 and it has been shown that for higher stand-off ratios, the shock wave impact at a flat material surface is the reason for such a behaviour. When the shock wave front travels along the interface, its velocity decreases as it moves further from the symmetry axis. Near the symmetry axis, the velocity of the shock wave is high and consequently the rates of loading and unloading are high. This does not allow the material to respond to the load because of its inertia, thus leading to a lower plastic strain close to the symmetry axis even though the maximum pressure acts at the symmetry axis

However, it can be noted that for  $SR = 1.2$ , there is a tiny zone of relatively high plastic deformation close to the symmetry axis. This is because the material deformation can happen due to two reasons: either by the shock wave impinging on material surface or by the impulse momentum of the liquid micro jet impinging first on the bubble surface and then on the material surface. For cavities far from the material surface ( $SR = 1.33$  and above), the impulse momentum of the micro jet is mostly converted in shock wave energy when it reaches the material surface. However, for  $SR = 1.2$ , where the distance between the solid surface and the bubble surface is smaller, the solid surface experiences both the shock wave (that causes plastic strain at offset from symmetry axis in fig 7.3d) and an impulse momentum created by the liquid micro jet (that causes plastic strain very close the symmetry axis).

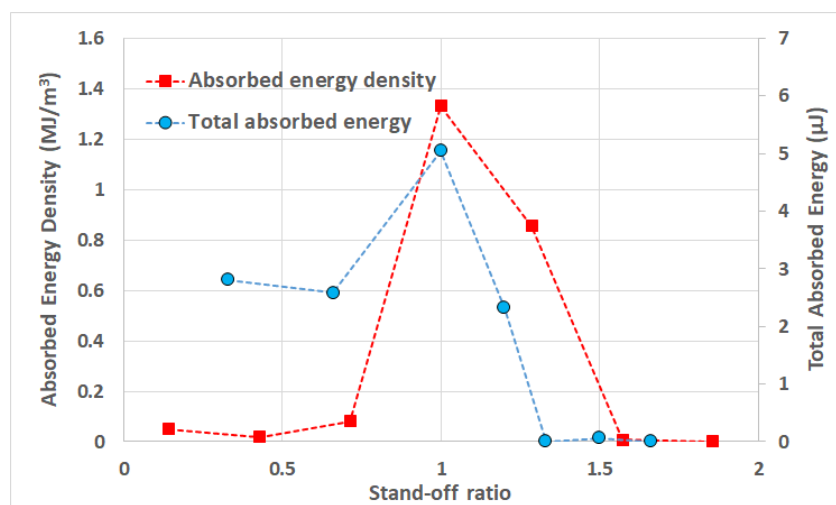


Figure 7.4. Plot of absorbed energy density and total absorbed energy wrt stand-off ratio for FSI single bubble collapse simulations (bubble radius and driving pressure are kept at 0.15 mm and 50 MPa respectively).

The above results show a clear comparison of plastic deformation mechanism for attached and detached cavities. We observe that the maximum plastic strain in the case of an attached cavity is generally much higher compared to a detached cavity but the volume of the plastically deformed zone for a detached cavity is much higher than for an attached cavity, which makes it difficult to understand the erosion ability of bubble collapses with different stand-off ratio.

In order to understand the erosion ability of the different cases presented in this section, we focus on two quantities as mentioned earlier: absorbed energy density (possible indicator of incubation time) and total absorbed energy (possible indicator of erosion rate). They are plotted in figure 7.4 for the seven stand-off ratios. For attached cavities ( $SR \leq 1$ ), it can be observed that the absorbed energy density is higher compared to detached cavities, which would suggest a smaller incubation time and possibly a quicker initiation of erosion. Within the attached cavities, for different stand-off ratios, the maximum absorbed energy density is observed for stand-off ratio of 1.0 which would lead to the fastest incubation during repeated impacts.

However due to the large volume of plastic zone for detached cavities close to solid ( $SR = 1.2$  &  $1.33$ ), the total absorbed energy which is an indicator for the erosion rate is much higher compared to attached cavities. Hence, even though the incubation time for  $SR = 1.2$  &  $1.33$  is lower than for attached cavities, the results suggest that thereafter the erosion rate could be a magnitude higher for detached cavities close to the solid compared to attached cavities. For detached cavities farther away from the wall ( $SR \geq 1.5$ ), the pressure of the shock wave decreases by the time it reaches the interface and could not produce high plastic strain.

### **7.3.2. Effect of driving pressure**

We present results for 3 different driving pressures (25 MPa, 50 MPa & 75 MPa) for an attached cavity ( $SR = 0.66$ ) and a detached cavity ( $SR = 1.33$ ), keeping the bubble radius constant at 0.15 mm. Contours of all these simulations are presented in figure 7.5. For detached as well as attached cavities, the maximum plastic strain increases with increase in driving pressure, which is expected as a higher pressure can produce a higher micro jet velocity leading to higher pressure on the solid.

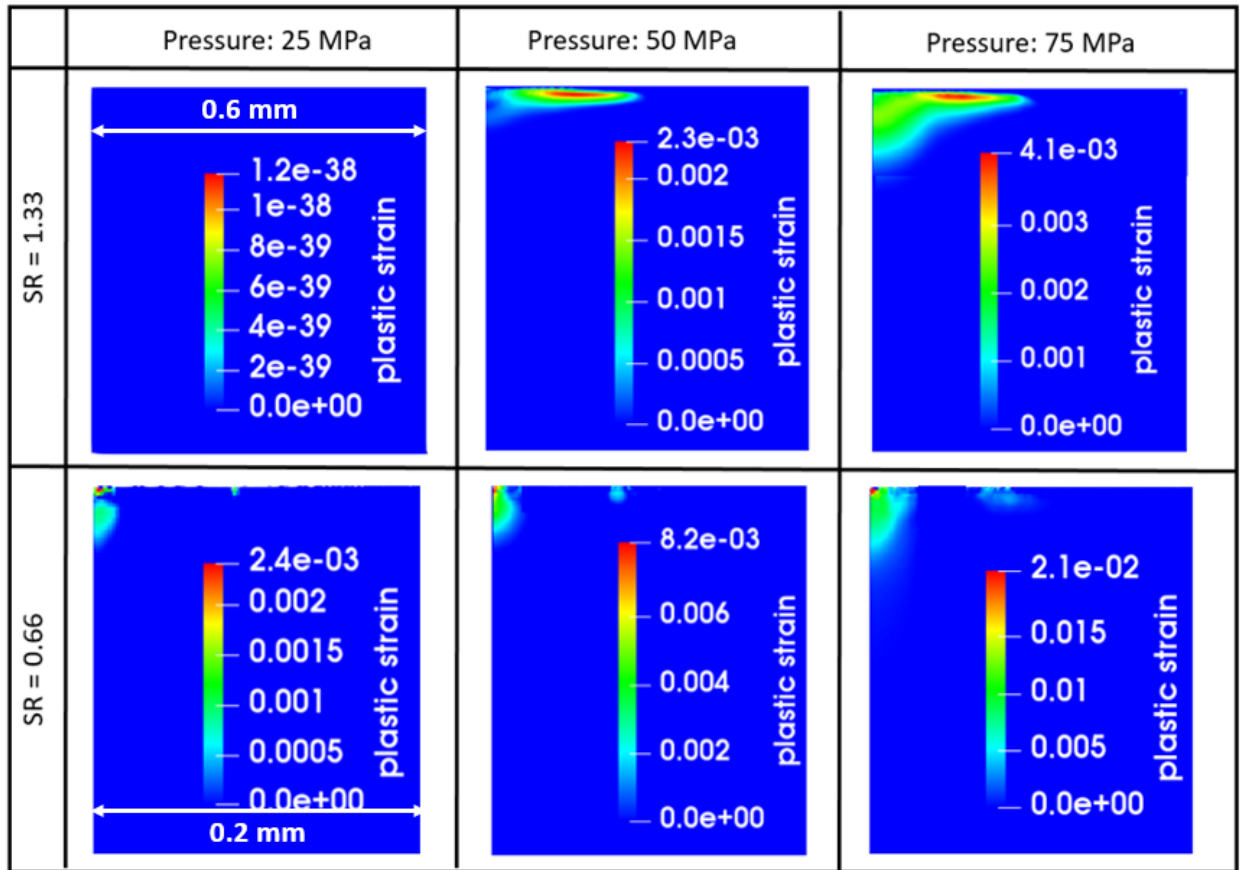


Figure 7.5. Contours of plastic strain for 3 different driving pressure (25 MPa, 50 MPa & 75 MPa) for detached cavity (SR = 1.33) and attached cavity (SR = 0.66) while keeping the bubble radius constant at 0.15 mm. All attached cavity contours (on the lower row) are magnified contours over the white dashed rectangle in figure 7.3g. The scale of the contours for SR = 1.33 is marked in its contours for driving pressure 25 Mpa (scale remains the same for all driving pressure at SR = 1.33). The scale of the contours for SR = 0.66 is marked in its contours for driving pressure 25 Mpa (scale remains the same for all driving pressure at SR = 0.66).

Figure 7.6 shows absorbed energy density and total absorbed energy for both attached and detached cavities plotted against driving pressure. It can be clearly observed that a higher driving pressure leads to a higher absorbed energy density and therefore a higher total absorbed energy. The absorbed energy density is higher for attached cavity for all driving pressures compared to detached cavity. However, the higher volume of plastic zone in case of detached cavity leads to a higher total absorbed energy compared to an attached cavity. The difference in total absorbed energy and hence erosion rate for detached and attached cavity seems to be more prominent as the driving pressure increases.

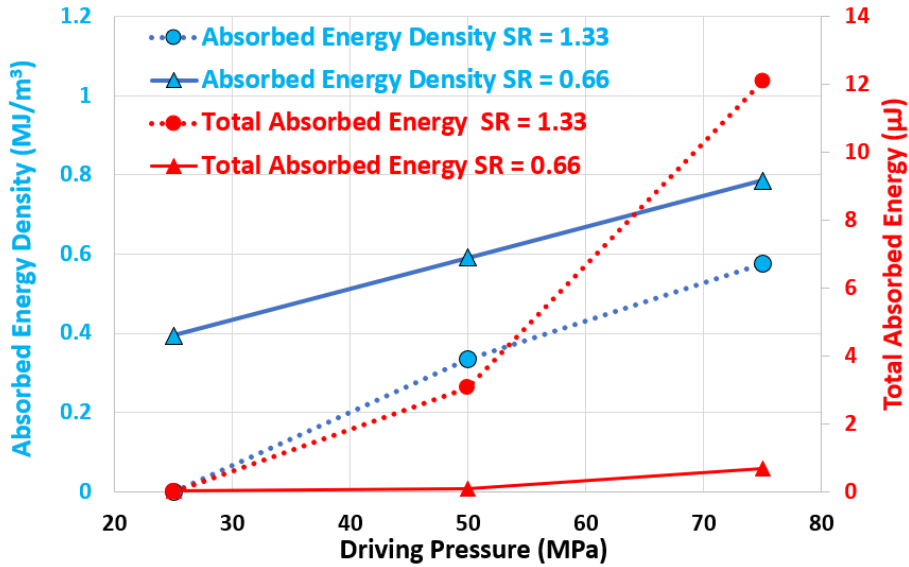


Figure 7.6. Plot of absorbed energy density and total absorbed energy wrt driving pressure for 2 different stand-off ratio ( $SR = 0.66$  &  $1.33$ ) for FSI single bubble collapse simulations.

### 7.3.3. Effect of bubble size

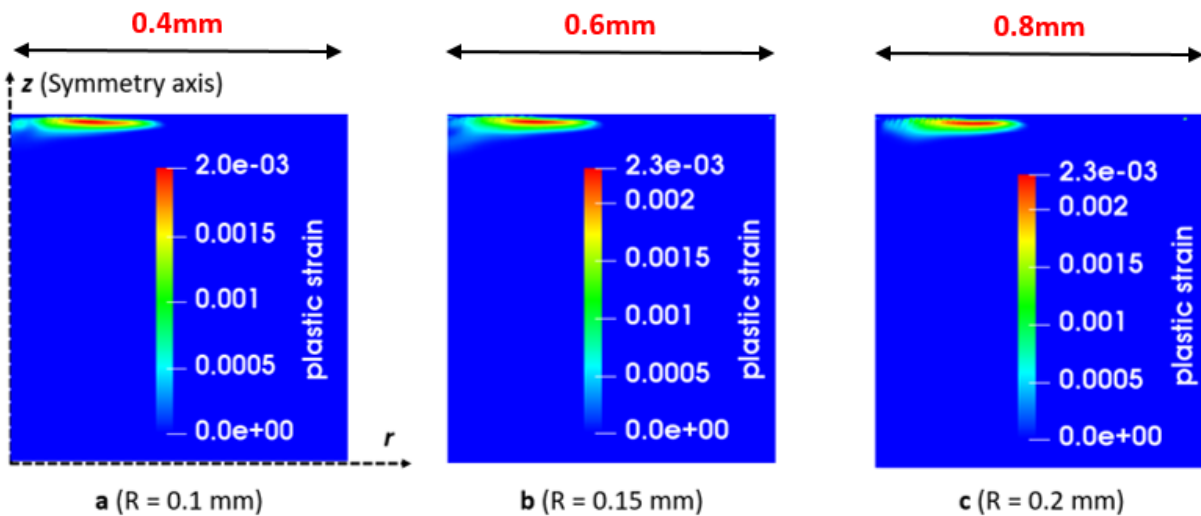


Figure 7.7. Contours of plastic strain for 3 different bubble radius ( $R = 0.1$  mm,  $0.15$  mm &  $0.2$  mm) for detached cavity ( $SR = 1.33$ ) while keeping driving pressure constant at  $50$  MPa. The scales have been marked on each contour, the scale of the domain linearly increases with the bubble size.

To understand the effect of bubble size, we use three different bubble radii ( $R = 0.1$  mm,  $0.15$  mm &  $0.2$  mm) for the detached cavity ( $SR = 1.33$ ) while keeping the driving pressure constant at  $50$  MPa. The contours of plastic strain suggest that the maximum plastic strain remains almost the same for different bubble radii. This is because the micro jet velocity is independent

of bubble size and hence the shock wave pressure at the interface remains almost the same for all bubble radii.

It could also be observed that the plastic strain close to the symmetry axis decreases as the bubble radius increases. This behaviour could be attributed to the speed of the shock wave front along the interface. When the point of collapse of the bubble has a smaller axial distance from the interface, the wave velocity along the interface near the symmetry axis is smaller (section 6.4.4.2). For a given stand-off ratio, the lower bubble size would have a lower axial distance of collapse from the interface and hence a lower shock wave velocity along the interface near the symmetry axis. Thus, the material has more time to react to the load which translates into plastic deformation.

As mentioned in section 7.2.1, the domain size scales with the bubble radius. Hence, the dimensions of the contours shown in figure 7.7 also scale with the bubble radius and therefore the volume of plastic strain zone increases with increasing bubble radius. Thus, even though the absorbed energy density exhibits almost similar values for all bubble radii, the total absorbed energy increases significantly with increasing bubble radius as shown in figure 7.8. This would suggest that the incubation time for all bubble radii would be almost the same whereas the erosion rate would increase significantly with increasing radius.

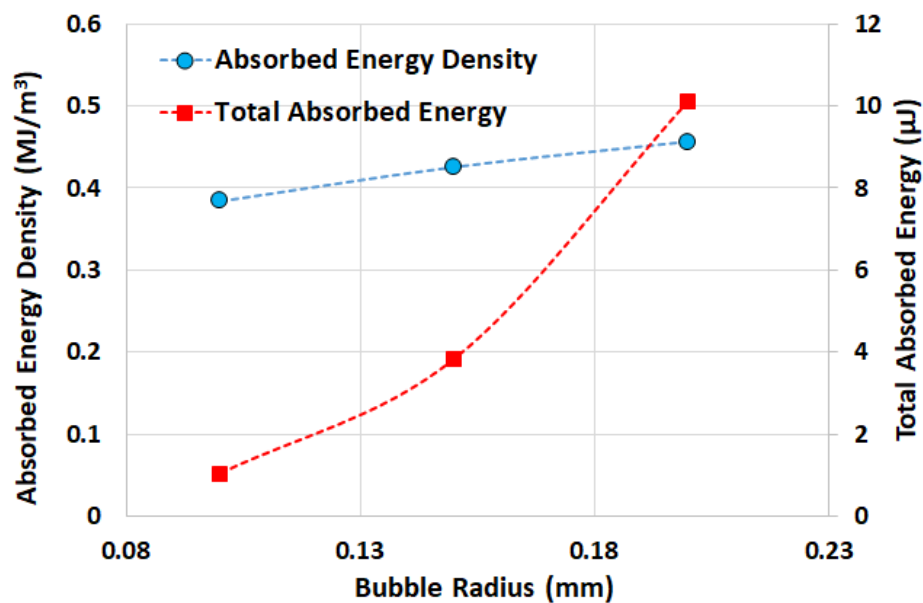


Figure 7.8. Plot of absorbed energy density and total absorbed energy wrt bubble radius (for  $SR = 1.33$  and driving pressure of 50 MPa) for FSI cavitation collapse simulations.

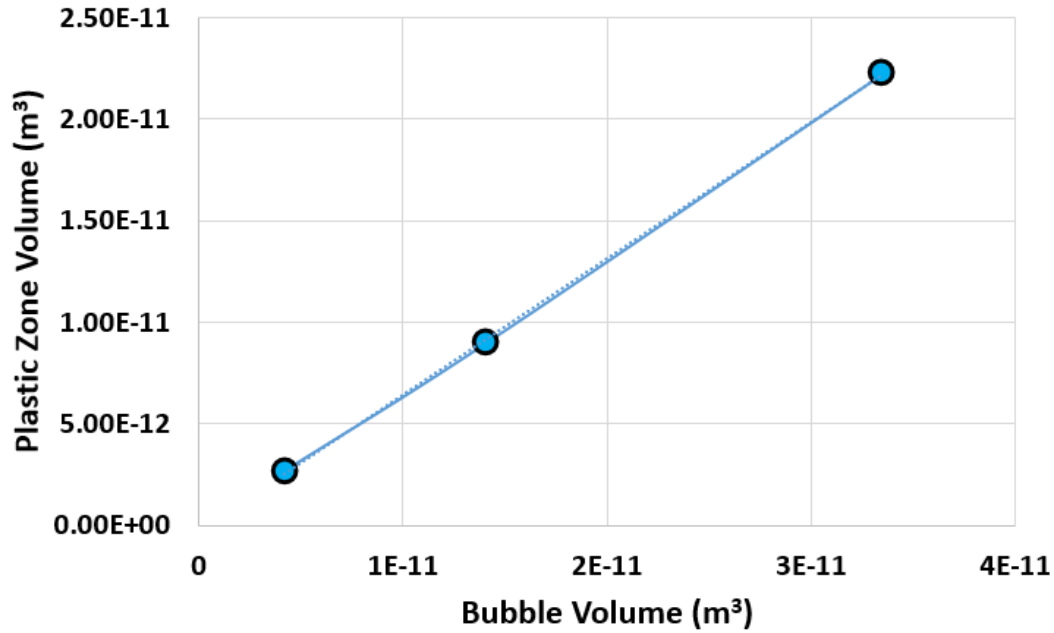


Figure 7.9. Plot of plastic zone volume vs bubble volume for three bubble radius (0.1, 0.15 & 0.2 mm),  $SR = 1.33$  and driving pressure of 50 MPa for FSI single bubble collapse simulations.

To understand the relationship between the bubble volume and the plastic zone volume, we plot in figure 7.9 the plastic zone volume on the left axis and the volume of the bubble for three bubble radii (0.1, 0.15 & 0.2 mm) while keeping the standoff ratio at 1.33 and driving pressure at 50 MPa. It can be observed from figure 7.9 that as the bubble volume increases the plastic zone volume increases linearly.

#### 7.3.4. Effect of strain rate

The effect of strain rate can be demonstrated by switching off the strain rate terms in equation 7.2 by substituting  $C_0$  as 0 instead of 0.031. We present results for  $C_0 = 0$  and  $C_0 = 0.031$  for three stand-off ratios ( $SR = 0.33, 1.0$  &  $1.33$ ), keeping the bubble radius and driving pressure constant at  $R = 0.15$  mm and  $P = 50$  MPa respectively. The two contours in column **a** of figure 7.10 are for a detached cavity ( $SR = 1.33$ ). It is observed that the strain rate insensitive case produces 60% higher maximum plastic strain and 40% higher volume of plastically deformed zone. Also, for attached cavity case shown in column **b** ( $SR = 1.0$ ) and **c** ( $SR = 0.33$ ), the plastic strain is almost 180% and 220% more in the strain rate insensitive case compared to the strain rate sensitive case for column **b** and **c** respectively. Hence strain rate sensitivity has an even more prominent effect on plastic strain for attached cavities. The case presented in column **c** ( $SR = 0.33$ ) shows an interesting effect. The primary and secondary plasticity zones (section

3.1 gives a description of these zones) show similar magnitude of plastic strain for the strain rate insensitive case. However, the strain rate sensitive case shows a higher magnitude of plastic strain in the primary plasticity zone compared to the secondary plasticity zone.

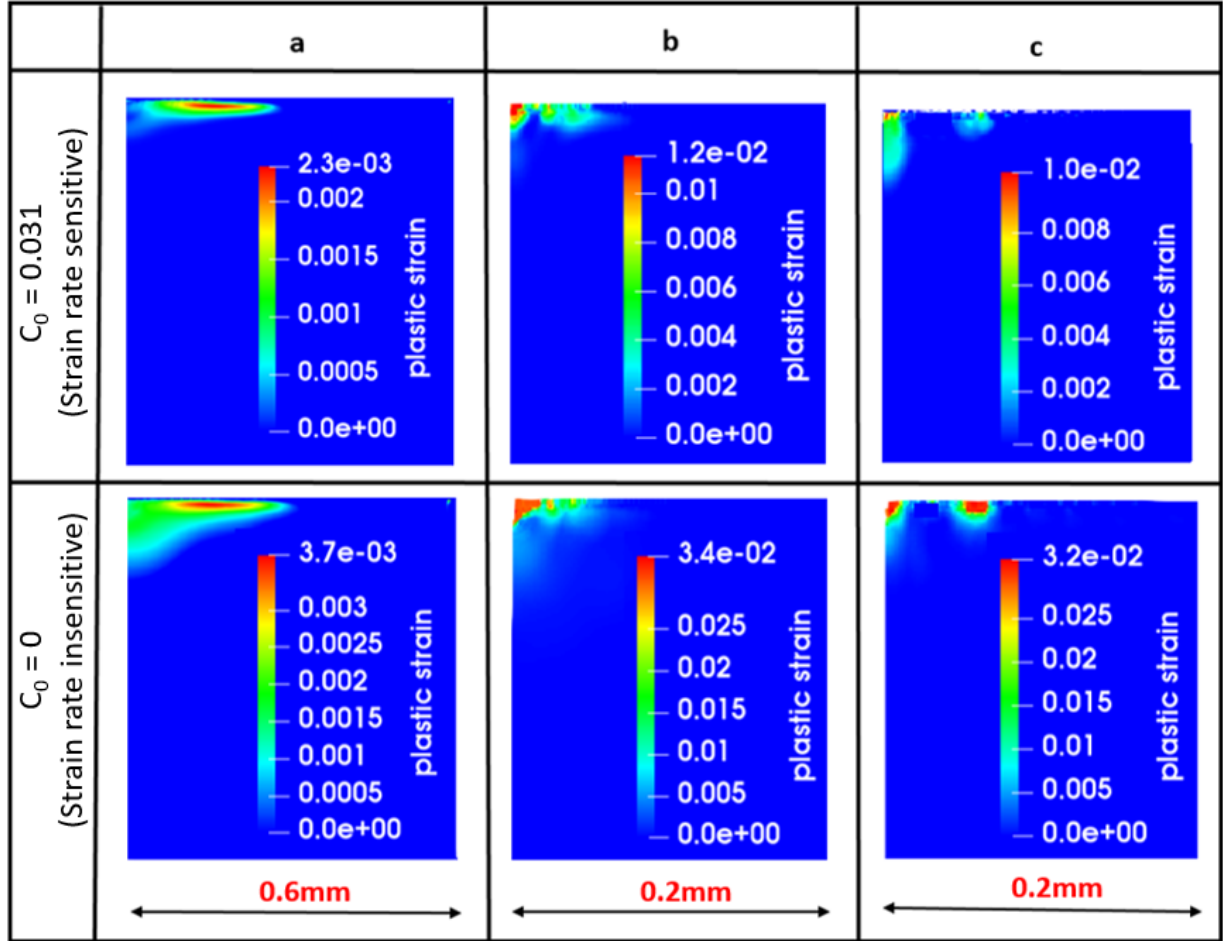


Figure 7.10. Contours of plastic strain for 3 different stand-off ratio ( $SR = 1.33, 1.0$  &  $0.33$ ) showing both strain rate sensitive ( $C_0 = 0.031$ ) and insensitive ( $C_0 = 0$ ) response while keeping the bubble radius and driving pressure constant at  $0.15$  mm and  $50$  MPa respectively. Column **a** shows results for  $SR = 1.33$ , column **b** shows results for  $SR = 1.0$  and column **c** shows results for  $SR = 0.33$ ; All attached cavity contours (column **b** and **c**) are magnified contours over the white dashed rectangle in figure 7.3g. The size of the domain is marked at the bottom of each column (the size marked at the bottom hold for both  $C_0 = 0$  and  $C_0 = 0.031$  in that column).

### 7.3.5. Plastic deformation potential

This section compares the plastic energy dissipated by the material to the potential energy of the bubble, which gives a relative potential of the cavity to produce plastic deformation in the material. We consider the ratio of the two quantities: plastic energy absorbed ( $W_{Plastic}$ ) and bubble potential energy ( $E_{Potential}$ ) which is given by the driving pressure multiplied by the

initial volume of the cavity). The ratio is hereafter in the article referred to as *Plastic Deformation Potential* (PDP) given by the following,

$$\%PDP = \frac{W_{Plastic}}{E_{Potential}} \times 100 \quad (7.3)$$

The %PDP is plotted in figure 7.11 against the stand-off ratio for 7 cases (SR = 0.33, 0.66, 1.0, 1.2, 1.33, 1.5 & 1.66) for the same driving pressure (50 MPa) and same bubble radius (0.15mm) and consequently for the same bubble potential energy. It can be observed that the amount of plastic energy absorbed by the material as a percentage of the initial bubble potential energy (%PDP) for attached cavities lie within a range of 0.09-0.019% (SR = 0.33, 0.66 & 1). However, the %PDP is around 0.53-0.83% for detached cavities close to the solid (SR = 1.2 & 1.33), which is more than a magnitude higher than the attached cavities. Furthermore, as the stand-off ratio increases for detached cavities (SR = 1.5 & 1.66), the bubble potential energy that translates to plastic energy goes down by a few orders of magnitude. Hence the *plastic deformation potential* of a cavity detached from the solid but placed close enough to the solid seems to be the highest compared to either an attached cavity or a detached cavity with higher stand-off (SR > 1.33).

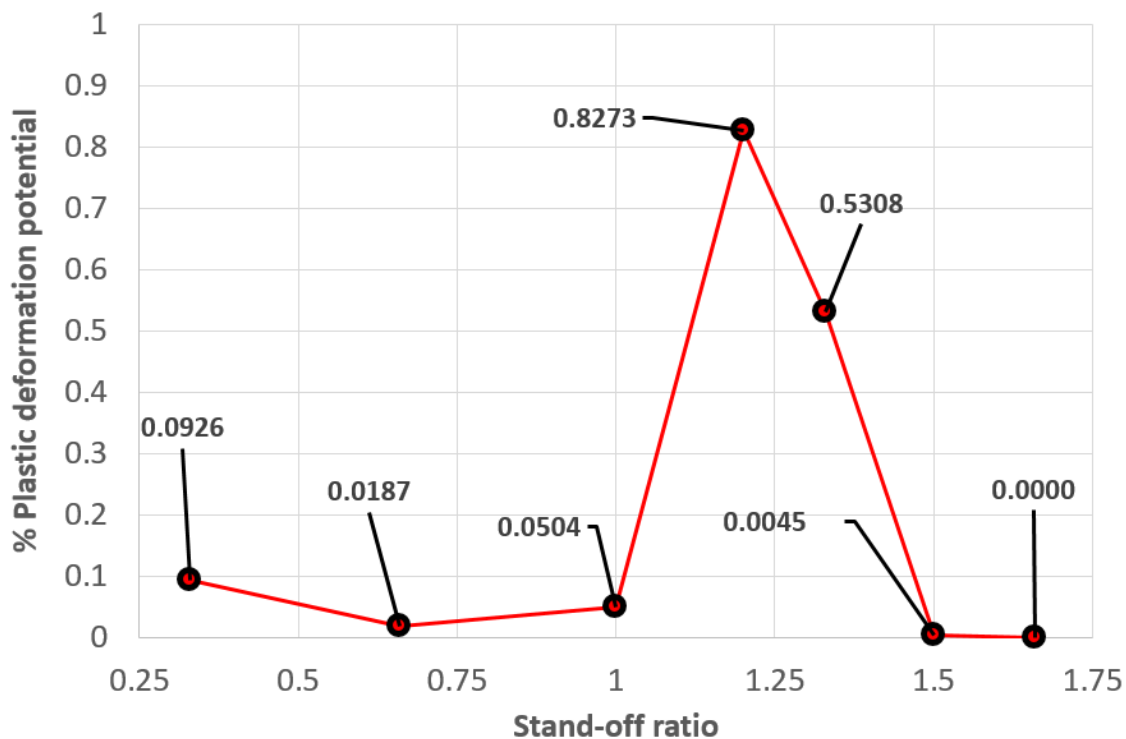


Figure 7.11. Plot of %PDP vs stand-off ratio (for bubble radius of 0.15 mm and driving pressure of 50 MPa) for FSI single bubble collapse simulations.

#### 7.4. Conclusions and future work

Fluid structure interaction simulations of single bubble collapse for different stand-off ratio, driving pressure and bubble radius has been presented in the article. Results reveal that for varying stand-off ratio while keeping the bubble radius and driving pressure constant, the attached cavities ( $SR \leq 1$ ) show a higher plastic strain magnitude and a higher absorbed energy density which would suggest a smaller incubation time in the case of repeated impacts. However, the volume of the plastic deformation zone and the total absorbed energy are much larger for detached cavities so that the erosion rate would be much higher in the case of repeated impacts.

The results show that, as expected, both the absorbed energy density (hence incubation time) and the total absorbed energy (hence erosion rate) increase with increasing driving pressure. The change in bubble radius while keeping other parameters constant does not affect the magnitude of plastic strain and absorbed energy density much, which would suggest that irrespective of the size of the cavitation bubble, the incubation time should remain similar for all bubble sizes. However, since the volume of plastically deformed zone goes linearly with the bubble volume, the total absorbed energy increases significantly with increasing bubble size, which would suggest that the erosion rate also increases significantly for repeated collapses.

Fluid structure interaction studies in the past have not considered strain rate sensitivity while defining the plasticity model. The strain rate effects presented in the paper suggest that the magnitude of the plastic strain is over predicted while using plasticity models that do not include strain rate sensitivity. In the case of 1-2205 duplex stainless steel, the over prediction of the magnitude of plastic strain is around 60% for detached cavities and around 200% for attached cavities. This would lead to an under prediction of incubation time and an over prediction of erosion rate while using strain rate insensitive plasticity models.

A quantity called *plastic deformation potential* (PDP) is introduced in the article which refers to the plastic energy absorbed by the material divided by the initial potential energy of the cavity. Thus PDP indicates the relative efficiency of a cavity to translate its potential energy into plastic energy. It is observed that detached cavities close to the solid wall can produce the highest PDP of the order of 0.83% (only 0.83% of bubble potential energy translates to plastic energy), the next most efficient are the attached cavities that can produce PDP of the order of 0.05% and the detached cavity far from the solid ( $SR > 1.5$ ) produce extremely low PDP values.

## Chapter Highlights

- A parametric study is carried out for FSI simulations of single bubble collapse over a stainless steel specimen (A-2205).
- Absorbed energy density is used to indicate incubation time and total absorbed energy indicates erosion rate. The two quantities are used to compare the erosion abilities of various cases.
- It is found that detached cavities placed close to the interface (stand-off ratio  $<1.5$ ) can show a much higher erosion rate compared to attached cavities.
- By varying bubble radii while keeping driving pressure and stand-off ratio constant, it is found that the maximum plastic strain seems to be similar for all bubble radius. However, the volume of plastic deformation zone linearly increases with increasing bubble volume.
- Use of strain rate sensitive plasticity model is important as the study shows that using strain rate insensitive models can lead to over prediction of the magnitude of plastic strain by around 60% for detached cavities and 200% for attached cavities.
- Plastic deformation potential which is the plastic energy absorbed by the material divided by the initial potential energy of the bubble is presented in the chapter. It shows that around 0.8% of bubble potential energy is absorbed as plastic energy for detached cavities close to the interface, for attached cavities it is around 0.05%.

# 8 CONCLUSIONS AND PERSPECTIVES

## 8.1 Conclusions

This thesis is focussed on the fundamental aspect of cavitation erosion and the underlying phenomena. Specifically, it focusses on studying cavitation erosion at a micro scale to see how bubble collapses lead to material damage using numerical methods. The objective of the thesis was to develop a Smoothed Particle Hydrodynamics (SPH) fluid structure interaction cavitation solver. To start with, an existing 2D open source fluid SPH code SPHYSICS is used as a basis to develop the solver further. The aim is to modify the fluid code to solve for bubble collapse and to develop a solid solver to be coupled to the fluid solver for simulating a collapsing bubble over a solid medium in 2D. The same solver is then extended to 2D axisymmetric to obtain more realistic results of material damage due to a collapsing bubble. Finally, the solver is used to simulate FSI cavitation bubble collapse which potentially could lead to better understanding of the cavitation erosion phenomenon.

An axisymmetric SPH solid solver is therefore developed that can treat the particles close to the symmetry axis in a mathematically consistent way. A novel scheme is proposed where density correction near the symmetry axis is used which leads to corrections in momentum equations that are for the first time derived in this thesis for solid response. The solver is capable of solving elasto-visco-plastic simulations with material damage and strain rate effects. An indentation test case is selected as a validation test case for reasons that firstly it can test the capability of the scheme in dealing with phenomenon near the symmetry axis and secondly that indentation loading is similar to cavitation loading. The results are compared against FEM results for the same case and an excellent agreement is observed. It is also demonstrated that the new formulation derived in the thesis provides a much more accurate result near the symmetry axis compared to the existing method. Mass loss curves were computed to demonstrate the capability of the model to solve for material damage. In this first study, the damage behaviour was simplistic. A more precise and sophisticated damage model should depend on various aspects such as [28]: cumulated plastic strain, stored energy, surface energy, stress triaxiality and strain rate. Various predictive models have been proposed so far to determine fracture criteria considering all the above parameters. Future work will consist of

including a more realistic damage model in the SPH code using experimental measurements. The mass loss curves obtained for different extents of the applied load have shown that the smallest extent of the indenter velocity profile  $R$  is the fastest to initiate damage but produces the lowest rate of erosion. The type of loading simulated here (indentation generated by the indent velocity) is quite different from the impact load due to bubble collapse.

To understand the actual behaviour of a bubble collapse near a solid, this solver is coupled to a fluid SPH solver to solve for cavitation bubble collapse near a solid. Hence, an axisymmetric SPH FSI solver has been developed, which is capable of computing the collapse of a single bubble over an elastic-plastic solid following a Johnson-Cook yield model. The fluid solver was validated against the analytical solution of the Rayleigh-Plesset equation and the solid solver against an FEM solver for an indentation case.

Simulations of the collapse of a detached and an attached cavity suggest that the micro jet generated during the collapse of an attached cavity has an ability to cause a larger maximum plastic strain in the material as compared to the shock wave generated during the collapse of a detached cavity. It is observed that for the same magnitude of pressure wave initiating the collapse and the same size of the bubble, the micro jet can produce twice the maximum plastic deformation compared to a shock wave. Hence, in case of repeated collapse, a micro jet dominated impact would exhibit a smaller incubation time compared to the detached cavity. On the other hand, the volume of material that is plastically deformed in case of a micro jet is miniscule compared to a shock wave impact (almost 800 times smaller). This would imply that, even though the incubation time for material erosion might be lower for a micro jet collapse, the shock wave can plastically deform a much larger volume of material and hence the erosion rate should be higher for a shock wave impact. Hence it could be inferred that the material erosion ability of a shock wave dominated collapse is much higher than that of a micro jet dominated collapse.

An important and novel finding in the present thesis is the response of the material for a detached cavity. It is shown that maximum plastic deformation does not occur at the center of collapse but at an offset from the center. Even though the pressure experienced by the material is the highest at the center, it does not produce the maximum plastic deformation there. This phenomenon is due to inertial effects, since the material tends not to respond to the load as the rate of loading and unloading is extremely high. The effect is linked to the high loading and unloading rate near the center of the collapse due to the flat geometry of the solid medium. The study clearly demonstrates that maximum pressure does not always correspond to the location of maximum plastic deformation.

A new parameter called effective pressure is defined in the thesis which matches well with the plastic strain in the material. However, the definition of effective pressure is based on the shock wave impacting the solid and hence is only valid for larger stand-off ratios ( $SR > 1.3$ ). For lower stand-off ratios the effective pressure under predicts the plastic strain near the symmetry axis which is due to the impact of the micro jet and not of the shock wave. An alternative approach to quantifying material response while considering inertial effects is by using characteristic time analysis. The material characteristic time and the loading characteristic time are compared for two cases ( $SR = 1.2$  &  $1.33$ ), where the lower material characteristic time relative to loading characteristic time signifies more dominant inertial effects and hence relatively lower plastic strain. The characteristic time analysis predicts the zones of plastic deformation quite well. However, the definition of material characteristic time is such that it cannot be known without solving for the solid since it relies on the plastic zone size.

Single bubble collapse fluid structure interaction simulations for different stand-off ratios, driving pressure and bubble radius have also been presented in the thesis. Results reveal that for varying stand-off ratio while keeping the bubble radius and driving pressure constant, the attached cavities ( $SR \leq 1$ ) show a higher plastic strain magnitude and a higher absorbed energy density which would suggest a quicker incubation time. However, the volume of plastic deformation zone is much lower in attached cavities, thus the total absorbed energy and the erosion rate would be higher for a detached cavity compared to an attached one.

The increase in driving pressure shows expected results where both the absorbed energy density (hence incubation time) and the total absorbed energy (hence erosion rate) increase with increasing driving pressure. The change in bubble radius while keeping other parameters constant does not affect the magnitude of plastic strain and absorbed energy density much, which would suggest that irrespective of the size of the cavitation bubble, the incubation time should remain similar for all bubble sizes. However, since the volume of the plastically deformed zone goes linearly with the bubble volume, the total absorbed energy or the erosion rate increases significantly with increasing bubble size.

Fluid structure interaction studies in the past have not considered strain rate sensitivity while defining the plasticity model [5-6]. The strain rate effects presented in the thesis suggest that the magnitude of plastic strain is over predicted while using plasticity models that do not use strain rate sensitivity. The over prediction of the magnitude of plastic strain of around 60% for detached cavities presented in the thesis and around 200% for attached cavities presented in the thesis is observed for A-2205 duplex stainless steel. This would lead to an under prediction

of incubation time and over prediction of erosion rate while using strain rate insensitive plasticity models.

A quantity called plastic deformation potential (PDP) is introduced in the thesis which refers to the plastic energy dissipated in the material divided by the initial potential energy of the cavity. PDP indicates the relative efficiency of a cavity to translate its potential energy into plastic energy. It is observed that detached cavities close to the solid wall can produce the highest PDP of the order of 0.83% (only 0.83% of bubble potential energy translates to plastic energy), the next most efficient are the attached cavities that can produce PDP of the order of 0.05% and the detached cavity far from the solid ( $SR > 1.5$ ) produce extremely low PDP values.

## 8.2 Perspectives

Although some perspectives have already been proposed in the previous section, this section focuses on more general perspectives regarding future work that can lead to a much better understanding of the cavitation erosion phenomenon:

### ➤ **Consecutive bubble collapse and mass loss curves**

The present thesis analyses in details the material response from a single bubble collapse, the results from these collapses are then used to extrapolate the erosion abilities of the material. For example, we use absorbed energy density and total absorbed energy as indicators to incubation time and erosion rate. However, these are based on single bubble collapses and by running a simulation with consecutive bubble collapse, we can actually obtain the mass loss curves and hence the incubation time and erosion rate directly. Such a solver can also be used to run simulations with different size and stand-off ratio of bubbles one after the other to understand how plasticity and therefore material erosion develops in the solid. However, since the time required for running such simulation could be very high, the solver should be optimised for multiple CPU or GPU processing to speed up the simulations.

### ➤ **Damage models**

The damage model implemented in this thesis is a simplistic one based on fracture strain. However, more sophisticated damage models for a ductile material are available in the literature which are based on the following quantities: cumulated plastic strain, stored energy, surface energy, stress triaxiality and strain rate. These models are based on the theory of void growth and coalescence in the material. They assume that material possesses voids and these would grow or shear under loads to merge with each other and produce a

crack. These models should be revisited in the case of high loading rate for example using a careful experimental investigation (by SEM, AFM or X-Rays) of the early stage of crack propagation in an eroded specimen. Then the model should be implemented in the solver to produce more accurate erosion curves. Moreover, most damage models for ductile fracture are developed from the data from tensile tests and not compressive tests. The difference between a compressive and a tensile load is that the tensile load encourages void growth and hence crack formation, whether the compressive load leads to closure of these voids and hence inhibiting crack formation. Only under the effect of shear do these voids have a chance to experience a shape change and hence a possible coalescence under a compressive load. Hence there is also a need to characterise material and obtain new damage criterion for compressive tests since the kind of load under cavitation is generally a compressive load on the material.

➤ **3D FSI solver for cloud collapses**

It could be argued that the single bubble collapse or even consecutive single bubble collapses is a rather simplistic calculation when considering a large cavity over equipments, let's say a hydrofoil. Investigating the loading on the material and the resulting material response due to multiple bubble collapses (cloud collapse) can provide a much better understanding of the cavitation erosion phenomenon. The solver presented in this thesis focusses on 2D axisymmetric calculation. An axisymmetric formulation cannot be used to simulate cloud collapses because of the geometrical limitations to represent only symmetric geometries. In order to simulate 3D clouds using SPH fluid structure interaction solver, the development process has to be re-initiated with an open source 3D fluid solver which can be used for cavity collapses and then adding a 3D solid solver to it. Most SPH 3D code need to be parallel and a good option would be to use Dual\_SPHYSICS which is a 3D GPU and CPU parallel solver with features that can be helpful in developing a solver capable of solving cloud collapses.

➤ **Cavitation resistant coating development and simulation**

The issue of cavitation erosion could be addressed in two ways: one would be to design equipments in such a way that it does not lead to cavitation erosion even if there is cavitation and the second would be to strengthen or protect the material via coating such that erosion is delayed or avoided even if there is cavitation. It has been shown that compliant materials like ultra-high molecular weight polyethylene (UHMWPE) has excellent cavitation erosion resistance over metallic alloys, which comes from high damping ability of the polymeric material to impact loadings [90]. Thus these materials can

be used as a coating for cavitation erosion protection of metallic structure but this coating is currently not being used in marine application for its weak adhesion to metallic alloys. Thus it would be interesting to numerically study the cavitation erosion behaviour of such compliant materials. The numerical simulation of cavitation erosion of coating on metallic substrate would be interesting as it could lead to important information that would help in designing the coating better in terms of thickness and properties. Apart from these so called soft coatings (polymer coatings), hard coatings can also be developed to protect the material from cavitation erosion. Simulating these coatings before an actual experiment can help determining the properties that suit cavitation resistance better.

➤ **Vapour or gas inside the bubble**

A major drawback of the present solver is the lack of vapour or gas inside the bubble. The solver simulates the cavity as a vacuum cavity that does not offer any resistance to the collapsing bubble. Moreover, the rebound and re-collapse of the bubble is completely missed since there is no gas inside the bubble. The loading due to the rebound bubble collapsing near the solid can lead to significant changes in the material response and hence it would be interesting to add vapour and/or gas inside the bubble. A better option would be to add gas inside the bubble. However, with such a system where the volume of the cavity goes from the initial bubble volume to almost zero, the SPH gas particle inside the bubble will have to occupy a very small volume at the end of the collapse. This would lead to overcrowding of particle and hence to inaccurate results at the liquid-gas interface and also to large computation time. A particle coalescence model should be considered to make sure we can avoid errors as the gas particles are squeezed into a small volume towards the end of collapse.





## Appendix A

### *Kernel Function*

The accuracy and stability of an SPH code is highly dependent on the choice of the kernel functions. They should satisfy several conditions such as positivity, compact support, and normalization. Also,  $w_{ab}$  of a particle  $a$  should monotonically decrease with increasing distance from the particle and behave like a delta function as the smoothing length  $h$  tends to zero [17-19]. The value of the Kernel function depends on the smoothing length  $h$ , and the non-dimensional distance between particles given by  $q = r/h$ ,  $r$  being the distance between particles  $a$  and  $b$ . The parameter  $h$ , often called smoothing length, controls the size of the area/volume around particle  $a$  where contribution from the rest of the particles is considered, outside the radius  $h$  the contribution of the particles is either zero or negligible.

A cubic spline kernel has been used in the present work:

$$W(r,h) = \alpha_D \begin{cases} 1 - \frac{3}{2}q^2 + \frac{3}{4}q^3 & 0 \leq q \leq 1 \\ \frac{1}{4}(2-q)^3 & 1 \leq q \leq 2 \\ 0 & q > 2 \end{cases} \quad (\text{A.1})$$

where  $\alpha_D = 2/(\pi h^2)$  in 2D and  $\alpha_D = 5/(4\pi h^3)$  in 3D.

## Appendix B

### *Return mapping algorithm*

To calculate plastic strain, a return mapping algorithm is required to return from a trial stress state to the yield curve at any time step, an incremental plastic strain is then calculated corresponding to the return from trial stress to the yield curve. Firstly, we define the von Mises stress as:

$$\sigma_{VM} = \sqrt{(\sigma^{rr} - \sigma^{zz})^2 + (\sigma^{rr} - \sigma^{\theta\theta})^2 + (\sigma^{\theta\theta} - \sigma^{zz})^2 + 6(\sigma^{rz})^2} \quad (\text{B.1})$$

and the equivalent plastic strain is defined as

$$\varepsilon_P = \frac{\sqrt{2}}{3} \sqrt{(\varepsilon_{pl}^{rr} - \varepsilon_{pl}^{zz})^2 + (\varepsilon_{pl}^{rr} - \varepsilon_{pl}^{\theta\theta})^2 + (\varepsilon_{pl}^{zz} - \varepsilon_{pl}^{\theta\theta})^2 + \frac{3}{2}(\varepsilon_{pl}^{rz})^2} \quad (\text{B.2})$$

At any time step, as the material deforms, the stress state is updated. If the von Mises stress goes beyond the Yield stress, the stress state is assumed as a trial state ( $\sigma_{VM}^t$ ). The stress state then has to return back to the yield curve as shown in fig B.1. The following equation then gives the solution to the incremental plastic strain ( $\Delta\varepsilon_P$ ):

$$\sigma_{VM}^t - 3G\Delta\varepsilon_P - \sigma_Y(\varepsilon_P^{N-1} + \Delta\varepsilon_P) = 0 \quad (\text{B.3})$$

Where  $\sigma_{VM}^t$  is the trial von Mises stress in the material,  $\Delta\varepsilon_P$  is the incremental plastic strain,  $\varepsilon_P^{N-1}$  is the plastic strain at time step N-1 and  $\sigma_Y$  is the yield stress in the material. The above equation can be solved using numerical methods such as Newton-Raphson. The yield stress can be calculated using equation 2.27, however, the yield stress not just depends on the plastic strain but also on plastic strain rate. To calculate equivalent plastic strain, rate the following equation is used:

$$\dot{\varepsilon}_P^N = \frac{\varepsilon_P^N - \varepsilon_P^{N-1}}{\Delta t} \quad (\text{B.4})$$

where a backward differencing method is used to calculate the derivative of plastic strain and

$$\varepsilon_P^N = \varepsilon_P^{N-1} + \Delta\varepsilon_P$$

The above calculation can be substituted in equation 2.27 to give yield stress and finally the yield stress is substituted in equation B.3 which then becomes a non-linear equation in  $\Delta\varepsilon_P$ . Iterative methods such as newton Raphson can then be used to solve for  $\Delta\varepsilon_P$  at each time step.

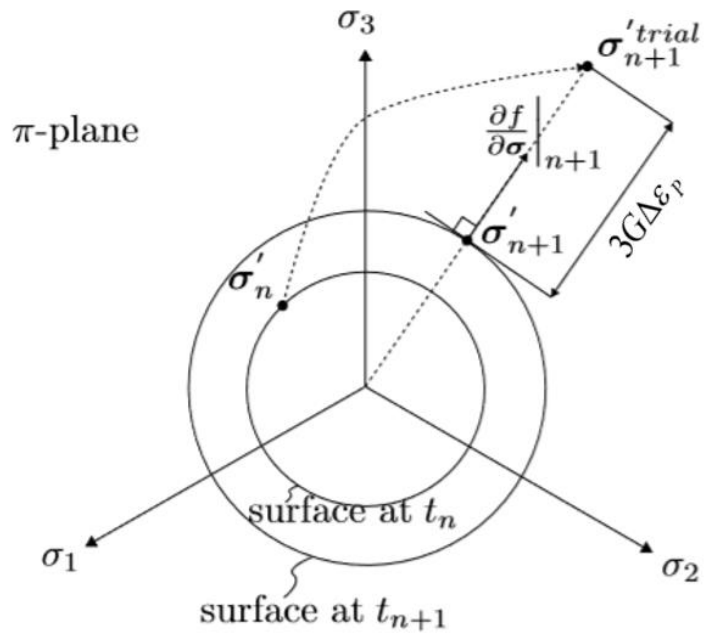


Figure B.1. Schematic shows the yield curve and the stress return algorithm in the  $\pi$ -plane, shows how stress from the trial state returns back to the yield curve.

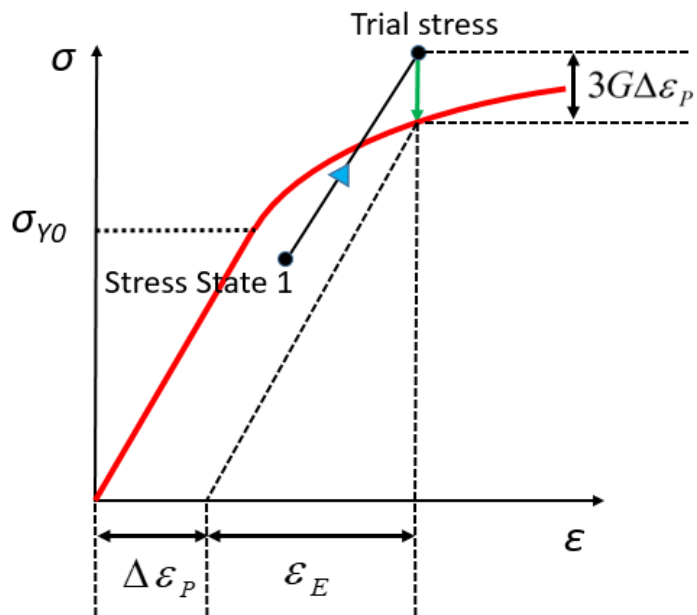


Figure B.2. Schematic shows the decomposition of elastic and plastic strain and return to the yield curve from a trial stress on a stress-strain curve.



## NOMENCLATURE

$W$	SPH Kernel function ( $m^{-3}$ )
$h_a$	kernel smoothing length (m)
$P_a$	pressure of particle $a$ ( $N/m^2$ )
$m_a$	mass of particle $a$ (Kg)
$\rho_a$	density of particle $a$ ( $Kg/m^3$ )
$\rho_{a0}$	Initial density of particle $a$ (at the start of the simulation) ( $Kg/m^3$ )
$\sigma$	stress tensor ( $N/m^2$ )
$\varepsilon$	strain tensor
$\dot{\varepsilon}$	strain rate tensor
$v_a^i$	velocity component of particle $a$ in direction $i$ (m/s)
$\Pi_{ab}$	artificial viscosity term for interaction of particle $a$ & $b$ ( $Nm^4/Kg^2$ )
$A_0, B_0, C_0, n$	coefficients in Johnson-Cook model ( $A_0$ & $B_0$ : $N/m^2$ , $C_0$ & $n$ : unitless)
$\vec{F}_{ab}$	Force vector on particle $a$ due to particle $b$ (N)
$F_r, F_z$	Force component in radial and axial direction respectively (N)
$n_r, n_z$	Interface normal unit vector components in radial and axial directions respectively
$\vec{F}_{ab}^{Interface}$	Force vector on particle $a$ due to particle $b$ (when $a$ & $b$ interact from across the interface) (N)
$\alpha, \beta$	coefficients in artificial viscosity term
$\bar{c}_{ab}$	average sound speed of particle $a$ and $b$ (m/s)
$\bar{\rho}_{ab}$	average density of particle $a$ and $b$ ( $Kg/m^3$ )
$\eta_a$	2D density of particle $a$ ( $Kg/m^2$ )
$\hat{\eta}_a$	corrected 2D density of particle $a$ ( $Kg/m^2$ )
$r_a$	radial distance of particle $a$ from the symmetry axis (m)
$f_1^a$	correction function for density equation of particle $a$
$\zeta_a$	non-dimensional radial distance of particle $a$ from the symmetry axis
$\sigma_Y$	yield stress for the material ( $N/m^2$ )
$\sigma_{Y0}$	initial yield stress for the material ( $N/m^2$ )
$d_H$	diametric extent of the load (m)

$\sigma_H$	maximum amplitude of the hydrodynamic impact pressure (N/m <sup>2</sup> )
$t_H$	characteristic impact rise duration (s)
$\alpha_z$	Axial distance of bubble collapse point from the interface (m)
$\mu, \lambda$	Lamé parameters (N/m <sup>2</sup> )
$\dot{\epsilon}_{p0}$	Reference plastic strain rate
$\dot{\epsilon}_p^*$	Non-dimensional effective plastic strain rate
$B_1, \gamma$	Parameters in Tait equation of state ( $B_1$ : N/m <sup>2</sup> & $\gamma$ : unitless)
$\vec{b}$	Body force vector (N/m <sup>2</sup> )
$\mathcal{E}_{coef}$	Coefficient for XSPH equation
$q$	Non dimensional distance between two particles given by $r/h$
$MDER_{max}$	maximum mean depth of erosion rate (s)
$\sigma_{vm}$	von Mises stress (N/m <sup>2</sup> )
$\epsilon_u$	permissible equivalent plastic strain for failure
$D_{DMG}$	damage parameter
SR	Standoff ratio = $D/R$
D	Distance of bubble center from the interface (m)
R	Radius of bubble (m)
$v_{SW}$	Shock front velocity along the interface (m/s)
$\alpha_z$	axial distance of shock generation point from the interface (m)
$PDP$	Plastic deformation potential
$W_{Plastic}$	Plastic energy dissipated in the material (J)
$E_{Potential}$	Initial bubble potential energy (J)

## REFERENCES

- [1] A. Philipp, W. Lauterborn, Cavitation erosion by single laser-produced bubbles, *J. Fluid Mech.* 361, 1998, pp 75–116. doi:10.1017/S0022112098008738.J
- [2] A. Vogel, W. Lauterborn, R. Timm, Optical and acoustic investigations of the dynamics of laser-produced cavitation bubbles near a solid boundary, *J. Fluid Mech.* 206 (1989) 299–338.
- [3] S.M. Ahmed, K. Hokkirigawa, R. Oba, Fatigue failure of SUS 304 caused by vibratory cavitation erosion, *Wear.* 177 (1994) 129–137. doi:10.1016/0043-1648(94)90238-0.
- [4] I.R. Jones, D.H. Edwards, An experimental study of the forces generated by the collapse of transient cavities in water, *J. Fluid Mech.* 7 (1960) 596–690. doi:10.1017/S0022112060000311.
- [5] T. Momma, A. Lichtarowicz, A study of pressures and erosion produced by collapsing cavitation, *Wear.* 186-187 (1995) 425–436. doi:10.1016/0043-1648(95)07144-X.
- [6] <http://cafe-project.eu/>
- [7] <https://ec.europa.eu/programmes/horizon2020/en/>
- [8] Phoevos K. Koukouvinis, George Bergeles, Manolis Gavaises, “A cavitation aggressiveness index within the Reynolds averaged Navier Stokes methodology for cavitating flows,” 2015, *Journal of Hydrodynamics, Elsevier*, 27(4):579-586, DOI: 10.1016/S1001-6058(15)60519-4
- [9] Z. R. Li, "Assessment of cavitation erosion with a multiphase Reynolds-Averaged Navier-Stokes method," PhD Thesis, TU Delft, 2012
- [10] Y. C. Wang and C. E. Brennen, "Numerical Computation of Shock Waves in a Spherical Cloud of Cavitation Bubbles," *Journal of Fluids Engineering*, vol. 121, pp. 872-880, 1999
- [11] Chao-Tsung Hsiao A. Jayaprakash, A. Kapahi, J.-K. Choi and Georges L. Chahine, "Modelling of material pitting from cavitation bubble collapse," *Journal of Fluids Mechanics*, 2014, vol. 755, pp. 142-175.
- [12] F. Pöhl, S. Mottyll, R. Skoda, S. Huth, "Evaluation of cavitation-induced pressure loads applied to material surfaces by finite-element-assisted pit analysis and numerical investigation of the elasto-plastic deformation of metallic materials", *Wear*, 2015, vol. 330-331, pp. 618-628. DOI: 10.1098/rspa.2017.0315
- [13] C. K. Turangan, G. J. Ball, A. R. Jamaluddin, T. G. Leighton, “Numerical studies of cavitation erosion on an elastic–plastic material caused by shock-induced bubble collapse,” *Proceedings of the Royal Society A*, 2017, vol. 473

- [14] Par Francois Axisa, Jose Antunes, “Modelling of Mechanical Systems: Fluid-Structure Interaction,” 2007, Elsevier, ISBN 10: 0-7506-6847-4.
- [15] Yves Paquette, "Interaction Fluide-Structure en Érosion de Cavitation " PhD Thesis, Université Grenoble Alpes, 2017
- [16] Gómez-Gesteira, M., Rogers, B.D., Dalrymple, R.A., Crespo, A.J.C. and Narayanaswamy, M., 2010, User Guide for the SPHysics Code v2.0. <http://wiki.manchester.ac.uk/sphysics>
- [17] Lucy, L., “A numerical approach to the testing of the fission hypothesis”, 1977, *Astronomical Journal*, vol. 82:1013–1024.
- [18] Monaghan, J. J. 1992. Smoothed particle hydrodynamics. *Annual Rev. Astron. Appl.*, 30: 543- 574
- [19] G.R. Johnson, W.H. Cook, Fracture characteristics of three metals subjected to various strains, strain rates, temperature and pressure, *Engineering Fracture Mechanics*, Vol. 21, No. 1, pp. 31-48, 1985.
- [20] Monaghan, J. and Pongracic, H, “Artificial viscosity for particle methods”, 1985, *Applied Numerical Mathematics*, 1.3:187–194.
- [21] Monaghan, J. J., “On the problem of penetration in particle methods”.1989, *Journal Computational Physics*, 82: 1-15.
- [22] Monaghan, J. J., “Smoothed particle hydrodynamics”, 1992, *Annual Rev. Astron. Appl.*, 30: 543- 574
- [23] Benz W., “Smoothed Particle Hydrodynamics: A review in *The Numerical Modelling of Nonlinear Stellar Pulsations: Problems and Prospects*”, 1990, J.R. Butchler ed., Kluwer Acad. Publ. 269-288
- [24] Liu, G.R., “Mesh Free methods: Moving beyond the finite element method”,2003, CRC Press, pp. 692.
- [25] Monaghan, J.J., and Lattanzio, J.C., 1985. A refined method for astrophysical problems. *Astron. Astrophys.* 149: 135–143.
- [26] Crespo, A.J.C., Gómez- Gesteira, M and Dalrymple, R.A. 2007. Boundary conditions generated by dynamic particles in SPH methods. *Computers, materials & continua*, 5(3): 173-184.

- [27] Dalrymple, R.A. and Knio, O. 2000. SPH modelling of water waves,” Proc. Coastal Dynamics, Lund.
- [28] Monaghan, J. J. and Kos, A. 1999. Solitary waves on a Cretan beach. *J. Wtrwy. Port, Coastal and Ocean Engrg.*, 125: 145-154.
- [29] Rogers, B.D. and R.A. Dalrymple, SPH Modeling of tsunami waves, *Advances in Coastal and Ocean Engineering*, Vol. 10 Advanced Numerical Models for tsunami waves and runup, World Scientific, 2008.
- [30] R.E.A. Arndt, Cavitation in fluid machinery and hydraulic structures, *Annu. Rev. Fluid Mech.* 13 (1981) 273–328.
- [32] G.J. Ball, B.P. Howell, T.G. Leighton, M.J. Schofield, Shock-induced collapse of a cylindrical air cavity in water: a Free-Lagrange simulation, (2000) 265–276. doi:10.1007/s001930000060.
- [32] T.B. Benjamin, A.T. Ellis, The collapse of cavitation bubbles and the pressure thereby produced against solid boundaries, *Philos. Trans. R. Soc. London A.* 260 (1966) 221–240.
- [33] J.P. Best, The formation of toroidal bubbles upon the collapse of transient cavities, *J. Fluid Mech.* 251 (1993) 79–107.
- [34] Lord Rayleigh, On the pressure developed in a liquid during the collapse of a spherical cavity, *Philos. Mag. Ser. 6.* 34 (1917) 94–98. doi:10.1080/14786440808635681.
- [35] M. Harrison, An Experimental Study of Single Bubble Cavitation Noise, *J. Acoust. Soc. Am.* 24 (1952) 776. doi:10.1121/1.1906978.
- [36] C.F. Naudé, A.T. Ellis, On the Mechanism of Cavitation Damage by Non-hemispherical Cavities Collapsing in Contact With a Solid Boundary, *J. Basic Eng.* 83 (1961) 648. doi:10.1115/1.3662286.
- [37] L.A. Crum, Surface Oscillations and Jet Development in Pulsating Bubbles, *Le J. Phys. Colloq.* 40 (1979) C8–285–C8–288. doi:10.1051/jphyscol:1979849.
- [38] Y. Tomita, A. Shima, Mechanisms of impulsive pressure generation and damage pit formation by bubble collapse, *J. Fluid Mech.* 169 (1986) 535–564. doi:10.1017/S0022112086000745.

- [39] O. Lindau, W. Lauterborn, Cinematographic observation of the collapse and rebound of a laserproduced cavitation bubble near a wall, *J. Fluid Mech.* 479 (2003) 327–348. doi:10.1017/S0022112002003695.
- [40] M.S. Plesset, R.B. Chapman, Collapse of an initially spherical Vapor Cavity in the Neighborhood of a solid Boundary, *J. Fluid Mech.* 47 (1971) 283–290. doi:10.1017/S0022112071001058.
- [41] E. Johnsen, T. Colonius, Numerical simulations of non-spherical bubble collapse, *J. Fluid Mech.* 629 (2009) 231. doi:10.1017/S0022112009006351.
- [42] A. Jayaprakash, C.-T. Hsiao, G. Chahine, Numerical and Experimental Study of the Interaction of a Spark-Generated Bubble and a Vertical Wall, *J. Fluids Eng.* 134 (2012) 031301. doi:10.1115/1.4005688.
- [43] N.D. Shutler, R.B. Mesler, A Photographic Study of the Dynamics and Damage Capabilities of Bubbles Collapsing Near Solid Boundaries, *J. Basic Eng.* 87 (1965) 511. doi:10.1115/1.3650589.
- [44] Franc, J.-P. and Michel, J.-M. (2006). *Fundamentals of cavitation*. Kluwer Academic Publisher.
- [45] Plesset, M. (1949). The dynamics of cavitation bubbles. *Journal of Applied Mechanics*, 48:277–282.
- [46] C. E. Brennen, “Bubble dynamics, damage and noise,” NREC, 1994.
- [47] J. S. Carlton, “Cavitation,” in *Marine Propellers and Propulsion*, Elsevier
- [48] J.-P. Franc, M. Riondet, A. Karimi, G.L. Chahine, Impact Load Measurements in an Erosive Cavitating Flow, *J. Fluids Eng.* 133 (2011) 121301. doi:10.1115/1.4005342.
- [49] R.I. Stephens, A. Fatemi, R.R. Stephens, H.O. Fuchs, *Metal Fatigue in Engineering*, John Wiley & Sons, 2000.
- [50] G.E. Dieter, *Mechanical Metallurgy*, McGraw-Hill, 1988.
- [51] K.-H. Kim, G. Chahine, J. Franc, A. Karimi, eds., *Advanced Experimental and Numerical Techniques for Cavitation Erosion Prediction*, Springer, 2014.
- [52] G.L. Chahine, P. Courbière, Noise and Erosion of Self-Resonating Cavitating Jets, *J. Fluids Eng.* 109 (1987) 429–435.

- [53] X. Escaler, F. Avellan, E. Egusquiza, Cavitation erosion prediction from inferred forces using material resistance data, in: 4th Int. Symp. Cavitation, 2001: pp. 1–9.
- [54] F.G. Hammitt, Damage to solids caused by cavitation, *Philos. Trans. A.* 260 (1966) 245–255.
- [55] M.K. Lee, W.W. Kim, C.K. Rhee, W.J. Lee, Liquid impact erosion mechanism and theoretical impact stress analysis in TiN-coated steam turbine blade materials, *Metall. Mater. Trans. A.* 30 (1999) 961–968. doi:10.1007/s11661-999-0149-y.
- [56] ASTM G32-06, Standard Test Method for Cavitation Erosion Using Vibratory Apparatus, ASTM International, West Conshohocken, PA, 2006, www.astm.org, n.d.
- [57] ASTM G32-10, Standard Test Method for Cavitation Erosion Using Vibratory Apparatus, ASTM International, West Conshohocken, PA, 2010, www.astm.org, n.d.
- [58] ASTM G134-95(2001)e1, Standard Test Method for Erosion of Solid Materials by a Cavitating Liquid Jet, ASTM International, West Conshohocken, PA, 2001, www.astm.org, n.d.
- [59] S. Hattori, T. Hirose, K. Sugiyama, Prediction method for cavitation erosion based on measurement of bubble collapse impact loads, *Wear.* 269 (2010) 507–514. doi:10.1016/j.wear.2010.05.015.
- [60] M. Futakawa, H. Kogawa, C. Tsai, S. Ishikura, Y. Ikeda, Off-line tests on pitting damage in Mercury target, Japan, 2003.
- [61] H. Soyama, M. Futakawa, Estimation of incubation time of cavitation erosion for various cavitating conditions, *Tribol. Lett.* 17 (2004) 27–30. doi:10.1023/B:TRIL.0000017415.79517.8c.
- [62] S. Hattori, Recent Investigations on Cavitation Erosion at the University of Fukui, in: K.-H. Kim, G.L. Chahine, J.-P. Franc, A. Karimi (Eds.), *Adv. Exp. Numer. Tech. Cavitation Eros. Predict.*, Springer, 2014: pp. 257–28
- [63] T. Okada, Y. Iwai, S. Hattori, N. Tanimura, Relation between impact load and the damage produced by cavitation bubble collapse, *Wear.* 184 (1995) 231–239. doi:10.1016/S0301-9322(97)88613-2.
- [64] A. Karimi, W.R. Leo, Phenomenological model for cavitation erosion rate computation, *Mater. Sci. Eng.* 95 (1987) 1–14. doi:10.1016/0025-5416(87)90493-9.

- [65] H. Kato, A. Konno, M. Maeda, H. Yamaguchi, Possibility of Quantitative Prediction of Cavitation Erosion Without Model Test, *Trans. ASME*. 118 (1996) 582–588.
- [66] N. Berchiche, J.P. Franc, J.M. Michel, A Cavitation Erosion Model for Ductile Materials, *J. Fluids Eng.* 124 (2002) 601. doi:10.1115/1.1486474.
- [67] G.L. Chahine, Modeling of Cavitation Dynamics and Interaction with Material, in: K.-H. Kim, G.L. Chahine, J.-P. Franc, A. Karimi (Eds.), *Adv. Exp. Numer. Tech. Cavitation Eros. Predict. Fluid Mech. Its Appl.* Vol. 106, Springer, 2014: pp. 123–161.
- [68] S.C. Roy, J.-P. Franc, C. Pellone, M. Fivel, Determination of cavitation load spectra – Part 1: Static finite element approach, *Wear*. In Press (2015). doi:10.1016/j.wear.2015.09.006.
- [69] S.C. Roy, J.-P. Franc, N. Ranc, M. Fivel, Determination of cavitation load spectra—Part 2: Dynamic finite element approach, *Wear*. In Press (2015). doi:10.1016/j.wear.2015.09.005.
- [70] F. Pöhl, S. Mottyll, R. Skoda, S. Huth, Evaluation of cavitation-induced pressure loads applied to material surfaces by finite-element-assisted pit analysis and numerical investigation of the elastoplastic deformation of metallic materials, *Wear*. 330-331 (2015) 618–628. doi:10.1016/j.wear.2014.12.048.
- [71] Chahine, G. L. & Perdue, T. O. 1990 Simulation of the three-dimensional behavior of an unsteady large bubble near a structure. In 3rd International Colloquium on Drops and Bubbles, Monterey, CA, AIP Conf. Proc., vol. 197, p. 188
- [72] Chahine, G. L., Duraiswami, R. & Kalumuck, K. M. 1996 Boundary element method for calculating 2-D and 3-D underwater explosion bubble loading on nearby structures. Report NSWCDD/TR-93/46. Naval Surface Warfare Center, Weapons Research and Technology Department, September (limited distribution).
- [73] Chahine, G. L. & Kalumuck, K. M. 1998a BEM software for free surface flow simulation including fluid structure interaction effects. *Intl J. Comput. Appl. Technol.* 11 (3/4/5), 177–199.
- [74] Wardlaw, A. B., Luton, J. A., Renzi, J. R., Kiddy, K. C. & McKeown, R. M. 2003 The Gemini Euler solver for the coupled simulation of underwater explosions. Tech. Rep. 2500, November. Naval Surface Warfare Center – Indian Head Division
- [75] S.C. Roy, “Modeling and analysis of material behaviour during cavitation erosion,” Phd dissertation Univ. Grenoble Alpes, 2015. <https://tel.archives-ouvertes.fr/tel-01267573/document>.

- [76] Christopher Earls Brennen, “Cavitation and bubble dynamics”, Oxford university Press 1995.
- [77] D. García-Senz, A. Relaño, R. M. Cabezón, E. Bravo, Axisymmetric smoothed particle hydrodynamics with self-gravity, Monthly Notices of the Royal Astronomical Society, Volume 392, Issue 1, 1 January 2009, Pages 346–360, 2008, <https://doi.org/10.1111/j.1365-2966.2008.14058.x>
- [78] André Pineau, Amine A Benzerga, T Pardoen, Failure of metals I: Brittle and ductile fracture, Acta Materialia, Vol. 107, pp. 424-483, 2016.
- [79] <http://www-cast3m.cea.fr>
- [80] Brookshaw L., “Smooth particle hydrodynamics in cylindrical coordinates”,2003, ANZIAM J, 44, C114
- [81] Monaghan J. J., “Smoothed Particle Hydrodynamics”, 2005, Rep. Prog. Phys., 68, 1703-1759
- [82] Jian Wang, Dave Chan, Jiahe Zhang, “Stable axisymmetric SPH formulation with no axis singularity”, 2016, International Journal for Numerical and Analytical Methods in Geomechanics, vol. 40, Issue 7, pages 987–1006.
- [83] Omang M., Borve S., Trulsen J., “SPH in spherical and cylindrical coordinates” 2006, Journal of Computational Physics, vol. 213, pages 391-412
- [84] Omang M., Borve S., Trulsen J., “Shock collisions in 3D using an axisymmetric regularized smoothed particle hydrodynamics code”,2007, Shock Waves, vol. 16, pages 467-475
- [85] M. Fivel, J. -P. Franc, S. C. Roy, “Towards numerical prediction of cavitation erosion,” Interface Focus, 5, 20150013. <http://dx.doi.org/10.1098/rsfs.2015.0013>
- [86] Monaghan, J. J. 1994. Simulating free surface flows with SPH. Journal Computational Physics, 110: 399- 406.
- [87] Peskin, C. S. 1977. Numerical analysis of blood flow in the heart. Journal Computational Physics 25: 220- 252.
- [88] Saira Freda PINEDA RONDON, "Numerical prediction of cavitation erosion" PhD Thesis, Ecole centrale de Lyon, 2018

[89] Yu-Kang Zhou, F.G. Hammitt, Cavitation erosion incubation period, *Wear*, Volume 86, Issue 2, 15 April 1983, Pages 299-313

[90] T. Deplancke, O. Lame, J.-Y. Cavaille, M. Fivel, J.-P. Franc, M. Rondet, Outstanding cavitation erosion resistance of Ultra High Molecular Weight Polyethylene (UHMWPE) coatings, *Wear*, 328-329, pp.301-308, (2015).



## ABSTRACT

The thesis is focused on development of a Smoothed Particle Hydrodynamics (SPH) Fluid-Structure Interaction (FSI) cavitation solver to investigate the phenomenon of material deformation under cavitation load. The fluid solver and the solid solver are validated against Rayleigh-Plesset spherical bubble collapse case and FEM solver respectively. The fluid solver is developed using an open source SPH code SPHYSICS\_2D and the code is changed from 2D to 2D axisymmetric. The solid SPH solver is developed in-house in 2D axisymmetric with a novel scheme to solve typical issues near symmetry axis. The solid solver has the capability to solve for non-linear isotropic hardening with strain rate effects (commonly known as Johnson-Cook plasticity model).

Various cases for detached and attached cavities are simulated using the FSI solver. The results show that, for the same magnitude of pressure wave initiating the collapse and the same size of the bubble, the micro jet can produce twice the maximum plastic deformation compared to the shock wave. Hence a micro jet dominated impact would exhibit a smaller incubation time compared to the detached cavity in the case of repeated cavitation impacts. It is also observed that the volume of material that is plastically deformed in case of a micro jet is miniscule compared to a shock wave impact (almost 800 times smaller). This would imply that even though the incubation time for material erosion might be lower for a micro jet collapse, the shock wave can plastify a much larger volume of material and so the erosion rate should be higher for a shock wave impact. Hence it could be inferred that the material erosion ability of a shock wave is much higher than that of a micro jet.

An important and novel finding in the present study is the response of the material for a detached cavity where plastic deformation does not occur at the center of collapse but at an offset from the center. The results show that even though the pressure experienced by the material is the highest at the center, it does not produce the maximum plastic deformation. This is for the first time that such a phenomenon is reported in cavitation studies. We find that the phenomenon is linked to inertial effects where the material does not respond to the load as the rate of loading and unloading is extremely high. The effect is linked to the high loading and unloading rate near the center of the collapse due to the flat geometry of the solid medium. The study clearly demonstrates that maximum pressure does not always correspond to the location of maximum plastic deformation or material erosion.

Fluid structure interaction simulations for different stand-off ratios, driving pressure and bubble radius have been computed. Results show that for varying stand-off ratio while keeping the bubble radius and driving pressure constant, the attached cavities ( $SR \leq 1$ ) show a higher plastic strain magnitude and a higher absorbed energy density which would suggest a quicker incubation time. However, the volume of plastic deformation zone is much lower in attached cavities thus the total absorbed energy and the erosion rate would be higher for a detached cavity compared to an attached one.

The change in driving pressure shows, as expected, that both the absorbed energy density (hence incubation time) and the total absorbed energy (hence erosion rate) increase with increasing driving pressure. The change in bubble radius while keeping other parameters constant do not affect the magnitude of plastic strain and absorbed energy density much, which would suggest that irrespective of the size of the cavitation bubble, the incubation time should remain similar. However, since the volume of plastically deformed zone goes almost linearly with the bubble size, the total absorbed energy or the erosion rate increases significantly with increasing bubble size.

Fluid structure interaction studies in the past have not considered strain rate sensitivity while defining the plasticity model. The strain rate effects suggest that the magnitude of plastic strain is over predicted while using plasticity models that do not use strain rate sensitivity. The over prediction of the magnitude of plastic strain of around 60% for detached cavities presented in the paper and around 200% for attached cavities presented in the paper is observed. This would lead to an under prediction of incubation time and over prediction of erosion rate while using strain rate insensitive plasticity models.

**Shrey Joshi, PhD Thesis, SIMaP-GPM2, University Grenoble Alpes, France**

